공학박사 학위논문

Damage detection and prediction of composite materials and their applications to fatigue and creep

손상 감지 및 예측을 통한 복합재료의 피로 및 크립 특성 예측 방법

2023 년 8 월

서울대학교 대학원

재료공학부

양 제 욱

Damage detection and prediction of composite materials and their applications to fatigue and creep

Advisor: Woong-Ryeol Yu

by

Jewook Yang

2023

Department of Materials Science and Engineering Graduated School Seoul National University

Damage detection and prediction of composite materials and their applications to fatigue and creep

손상 감지 및 예측을 통한 복합재료의 피로 및 크립 특성 예측 방법

지도 교수 유 웅 열

이 논문을 공학박사 학위논문으로 제출함

2023 년 8 월

서울대학교 대학원

재료공학부

양 제 욱

양제욱의 공학박사 학위논문을 인준함

2023 년 8 월

위 원 장 안 철 희 (인)

부 위 원 장 유 웅 열 (인)

위 원 이 명 규 (인)

위 원 안 현 철 (인)

위 원 나 원 진 (인)

Abstract

Composite materials including steel-polymer sandwich composites and short fiber-reinforced plastics (SFRPs) exhibit high mechanical properties and low density, so they are widely used in various industrial fields such as automobile, aviation, aerospace and defense industries. However, composites used in automotive and structural parts are typically subjected to environmentally dynamic conditions. Damage resulting from external loading, such as forming, creep and fatigue, significantly contributes to the degradation of mechanical properties in composite materials. Therefore, it is crucial to incorporate a safe design that considers these factors. In this study, experimental and theoretical investigations were conducted to detect and analyze such damage, aiming to apply the findings in forming or predicting the creep-fatigue lifespan of composites.

Firstly, the delamination damage was detected using acoustic emission (AE) technique. Multiple tests were conducted to identify the distinctive AE features associated with the failure modes of the sandwich composites. Subsequently, a punch test was performed while monitoring AE signals. By utilizing the AE signals related to delamination, a new FLD for steel-polymer sandwich composites was constructed. Additionally, formability tests were simulated using the cohesive zone model, taking into account interfacial properties, to investigate the impact of interfacial adhesion on the formability of the sandwich composites.

Secondly, a progressive pseudograin damage accumulation (PPDA) model is proposed to predict the fatigue life of short fiber-reinforced plastics (SFRPs), combining viscoelastic-viscoplastic (VEVP) two-step homogenization theory with Chaboche fatigue damage model. Each representative volume element (RVE) of SFRPs is decomposed into pseudograins using a two-step homogenization framework. Then, the fatigue life of each pseudograin is predicted using a master S-N curve, which is prepared based on the “normalized fatigue factor” taking into account both the stress ratio and multiaxial stress state. Thereafter, the overall failure of RVE is predicted by a PPDA model, in which each pseudograin fails progressively considering the stress concentration of the living pseudograins, resulting in non-linear fatigue damage evolution. The PPDA model is implemented into ABAQUS user material subroutine (UMAT), predicting the fatigue lifetime in good agreement with experimental data.

Lastly, the PPDA model is expended to predict the creep and creep-fatigue interaction effect of SFRPs. Creep damage model and creep-fatigue interaction damage model is combined with Tsai-Wu effective stress and normalized fatigue factor. The expended model was implemented into ABAQUS user material subroutine and predicted creep life appropriately showing that PPDA approach is in a good agreement with experimental results in literature compared to first pseudograin failure model or last pseudograin failure model. Furthermore, PPDA model reflects nonlinearity of creep-fatigue interaction effect in SFRPs.

Keywords: Composite materials, steel-polymer composites, short fiber-reinforced plastics, acoustic emission, mean-field homogenization, progressive damage

accumulation model

Student number: 2017-22541

Contents

List of tables

List of figures

Chapter 1. Introduction

1.1. Composite materials

International Energy Agency, IEA reported the data in 2022 that about 22% of the total CO_2 worldwide is produced in the transport section as shown in **Figure 1-1** [1]. Vehicles are responsible for a huge depletion of natural resources for materials and fuels production. In the recent years, the car manufacturers have been implementing several technical solutions to meet EU legislation requirements. Electric vehicle is one of the promising solution for CO_2 reduction. According to the IEA report, CO_2 emissions would have been 13 Mt higher, if all new electric cars had been diesel or gasoline cars [1]. Nonetheless, the range that an electric vehicle can travel without recharge is not satisfactory due mainly to the limitation of energy storage. Due to the such increasing demands for energy saving vehicles, the need to develop new lightweight materials becomes essential. Composite materials been increasingly used in automotive industry for their advantages of lightweight, high strength [2].

Composite materials can be categorized according to their structure as listed in **Figure 1-2** [3]. Particle composites are normally based on the metallic matrix with hard particles to offer high strength and wear resistance. Structural sandwich laminates with adhesive layer and short fiber-reinforced composites (SFRPs) are the main focus of this study.

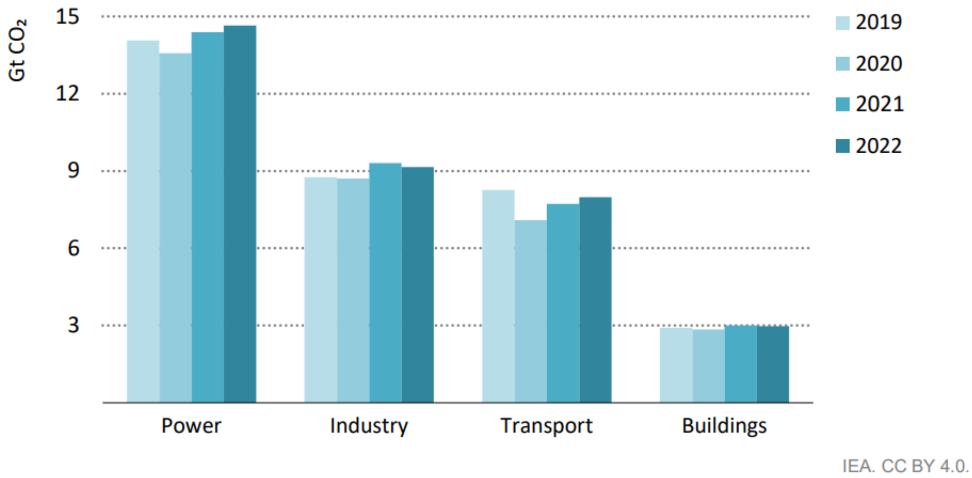

Figure 1-1 Global CO_2 emissions by sector, 2019-2022 [1].

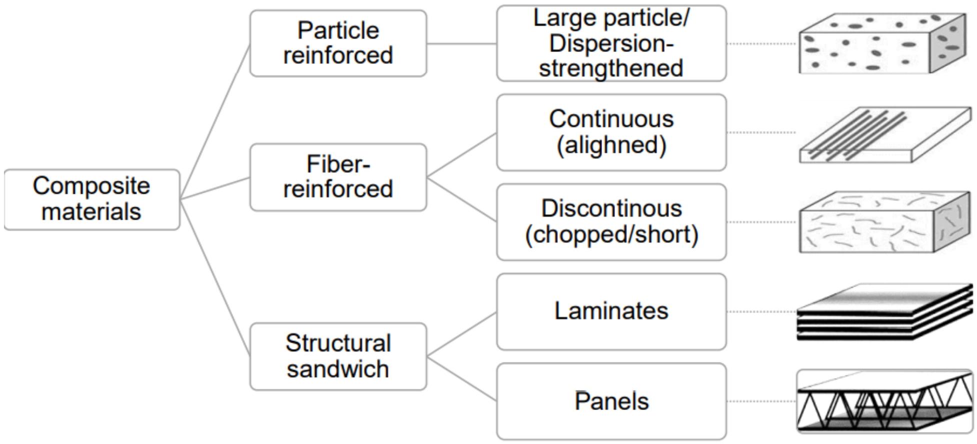

Figure 1-2 Types of composite materials [4].

1.1.1. Steel-polymer sandwich composites

Steel–polymer sandwich composites are composed of two skin steel layer and a core polymer layer. Steel–polymer sandwich composites have advantages such as improved specific weight and enhanced energy absorption characteristics while having comparable bending stiffness with the monolithic steel sheet [5] . In addition, due to the core polymer, steel–polymer sandwich composites exhibit multifunctional properties, such as acoustic damping and heat insulation [6-12]. Due to their favorable properties, laminated steel–polymer sandwich sheets have been widely used to replace monolithic steel sheets in automotive, aerospace and construction industries [13].

1.1.2. Short fiber-reinforced composites

Short fiber-reinforced plastics (SFRPs) comprised of polymer matrix and reinforcing short fiber, are one type of fiber-reinforced composites (FRPs) which have replaced metals in various industrial products to achieve weight reduction [14-18] due to their great specific properties (**Figure 1-3** [19]). Their fibers are randomly oriented, so that SFRPs show isotropic properties in nature. Injection-molded short fiber-reinforced plastics have the advantages of molding flexibility, mold cycle time and formability. While, injection molding, short fibers are typically subjected to matrix flow so that final structure part shows aligned orientation as shown in **Figure**

1-4. Therefore, environmentally dynamic conditions including multiaxial fatigue loading.

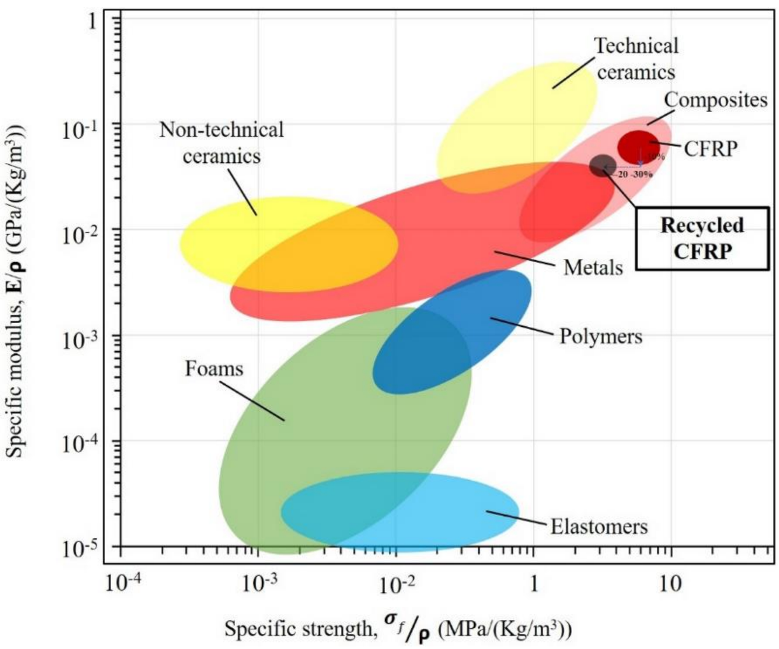

Figure 1-3 Specific strength and stiffness values of conventional materials and FRPs [19].

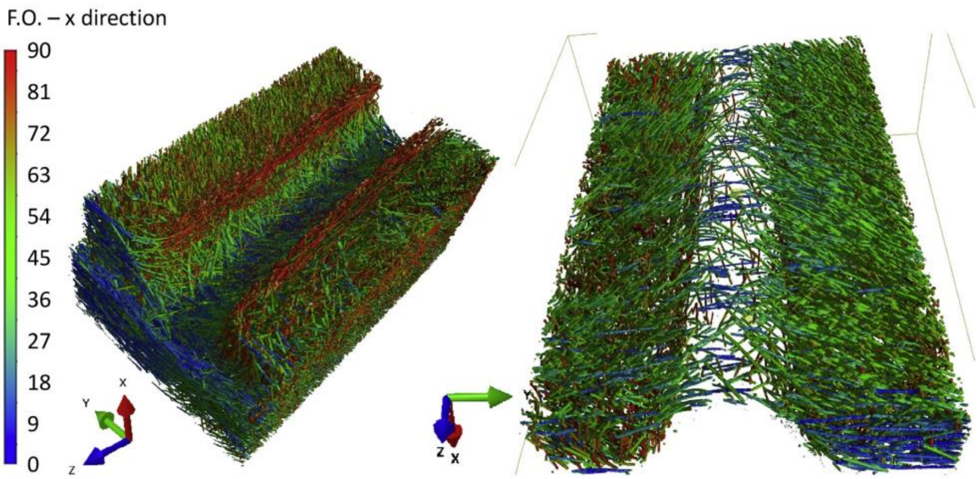

Figure 1-4 Fiber orientation distribution in the material volume analyzed by means of X-Ray CT.

1.2. Damage of composite materials

Micromechanical damage development in composites can result in the degradation of whole composite parts and the mechanical properties. Micromechanical damage can occur in the process of forming and their usage. However, it does not lead to the immediate rupture of the composite laminate. Instead, it leads to a nonlinear response due to the constraining effects of undamaged part of composites. To describe microdamage initiation and propagation, many studies have been studied. Tanaka, K. et al [20] studied the influence of fiber orientation on crack propagation with single edge-notched SFRP specimens. They observed fatigue crack propagation with SEM image. Crack path was changed depending on the fiber orientation showing damage development can differ according to the fiber orientation. Also, Li, Z. et al [21] conducted full simulation of SFRPs to understand the relationship between microstructures and complex mechanical behaviors of the materials. They reported that the damage initiation results from fiber-matrix debonding at fiber ends, which is perfectly consistent with shear-lag theory and experimental characterization [22, 23]. In the next step, stress is continuously redistributed and the fiber breakage happens. It leads to the crack of neighboring matrix. Then, loads are transferred to nearby fibers and matrix along the crack direction. Finally, the damage is accumulated until the ultimate failure happens.

Various methods reported to quantitatively measure damage in composites. As a direct method, the internal damage was directly observed through an observation instrument such as high speed camera [24] and X-ray computed tomography [25-27].

As an indirect method, it was reported that the damage inside the composites could be measured by using methods such as ultrasonic wave [28], acoustic emission [29, 30], vibration damping [31], and electrical resistance [32].

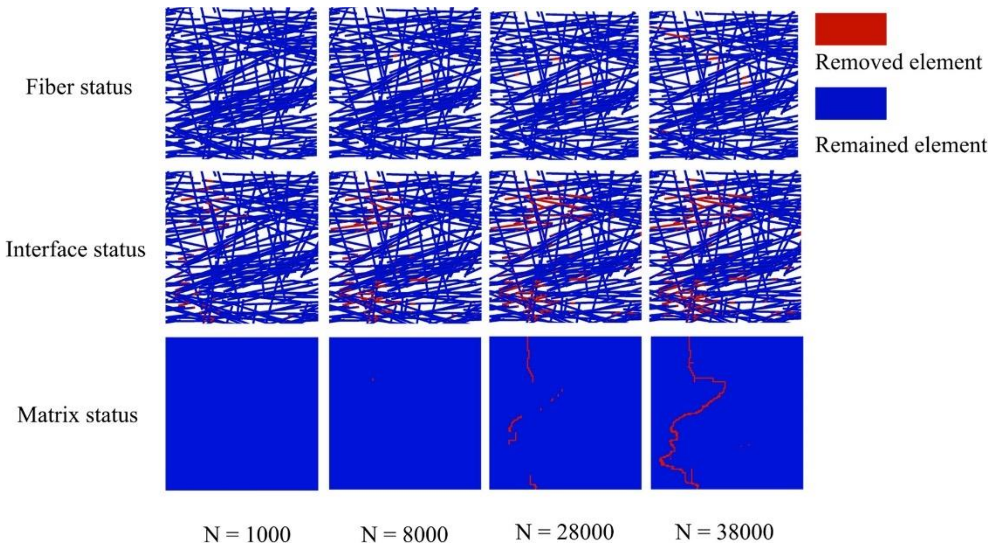

Figure 1-2 Progressive element status during cyclic loading: fiber status (top), interface status (middle), and matrix status (bottom) [33].

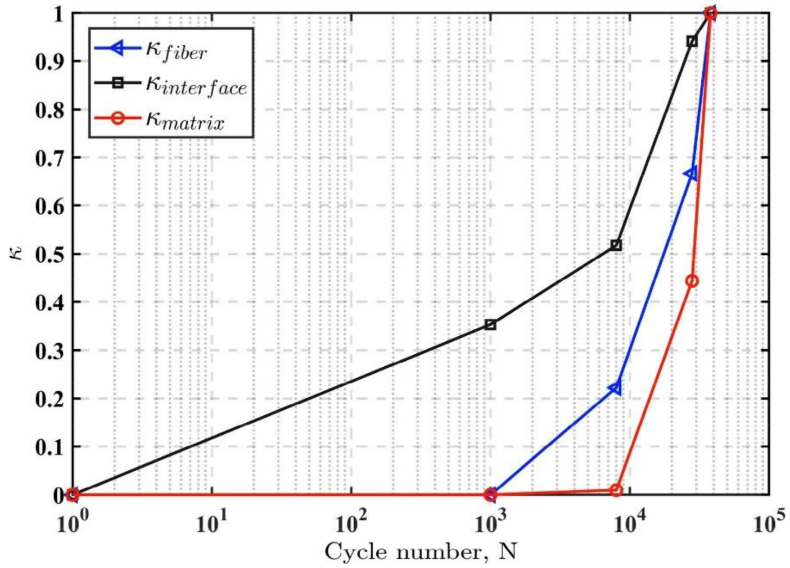

Figure 1-3 The fatigue damage extent variables of different fatigue failure modes in SFRPs [33].

1.3. Formability of composite materials

For the composite to be applied to industrial fields, it should be made into various shapes after forming process. Generally, materials have a forming limit, and the forming limit diagram (FLD) is mainly used as an indicator of the formability of the material. The FLD shows the criterion for major and minor strains that can be formed without failure. With the FLD, the stable forming process can be designed. Therefore, many researches have been conducted on constructing FLD of metal-polymer sandwich composites experimentally [34-45]. Among them, some researchers consider damage in composites and made model for numerical simulation because making the FLD for sandwich composites through experiments required considerable labor [35]. There were various model for predicting the FLD, such as mathematical models (Hill-Swift model, Barlat model, Marciniak-Kuczynski model and Sing-Rao model) and empirical model proposed by the North American Deep Drawing Research Group (NADDRG), but they were suitable only in a specific situation and in most cases did not match the experiment [46]. When the FLD of the sandwich composite was created through simulation and compared with the experimental results, the results showed more similar to the experimental results than the above-mentioned models [36]. However, most of the simulations were performed through structural simplification or without consideration of interfacial properties. As mentioned above, even for relatively simple properties such as mechanical properties and vibration damping performance of sandwich composite, consideration of the interfacial properties is necessary for accurate prediction. When performing the formability test of the sandwich composite in our research group, the delamination at the interface occurred. Therefore, in order to explain the formability of the sandwich composites, the delamination must be considered.

1.4. Two-step homogenization model

Various mechanical models of SFRPs considering mechanical responses of SFRPs have been reported. One of the most widely used type of model is full representative volume element (RVE) simulation model, which contains mechanical properties and geometries of all constituents of SFRPs [47-49]. However, this model has high computational cost for bigger industrial parts such as car body or airplane wings [49].

Instead, A two-step homogenization model was first proposed by Pierard et al. [50] as an approach to consider micromechanical aspects such as mechanical properties of constituents and fiber orientation distribution while reducing the computational time. In this model, RVE is decomposed into several domains. Each domain is a group of elements with similar fiber orientation, and these domains are called pseudograins. In the first step, the fibers and matrix are homogenized to predict the behavior of each pseudograin using various theory such as Eshelby's single inclusion theory [51], Mori–Tanaka model [52], self-consistent model [53], double-inclusion model [54], and differential-scheme model [55]. Then, in the second step, the pseudograins are treated as individual materials, and they are homogenized to predict the behavior of the RVE using various model such as uniform strain assumption (Voigt model [56]), uniform stress assumption (Reuss model [57]), or a combination of both (Voigt–Reuss model [58]).

This two-step homogenization model has been studied by many researchers [58-65]. Pseudograins are assumed to be elastic and unidirectionally aligned in a representative orientation, which is determined by processing orientation distribution function (ODF) with equivalent orientation approach [66] or iso-size facets algorithm [67]. Many mechanical models for pseudograin are used such as the elasticity, viscoelasticity and viscoelastic-viscoplasticity [63, 68-71], and fracture mechanics [61, 63]. When predicting damage of SFRPs using the two-step homogenization, a progressive failure was modeled as a successive failure of pseudograins, employing continuum damage mechanics to calculate the damage accumulation of each pseudograin. Then, the “first pseudograin damage (FPGD)” model by analogy with first-ply-failure concept for laminates was used to predict static failure of SFRPs under tensile loading [61, 63]. This model is suitable for predicting the failure of multiaxial loading with various fiber orientations, however, damage accumulation by interaction between pseudograins have not been considered.

1.5. Research objectives

In this thesis, the objectives are detecting and predicting damage of composite materials, and applying feature and model to predict mechanical behavior of them. For those purpose experimental and theoretical approaches were conducted to understand damage evolution involved in forming behavior of steel-polymer sandwich composites and creep-fatigue behavior of SFRPs.

In Chapter 2. the formability of steel–polymer sandwich composites was investigated using a new forming limit diagram (FLD) while considering delamination and fracture. The acoustic emission (AE) technique was used to observe delamination during the forming process. Several tests, including tensile and lap shear tests, were performed to identify the AE features of delamination. In addition, finite element simulations were carried out using the cohesive zone model to predict the delamination of steel–polymer sandwich composites. An FLD of the sandwich composite was also constructed using the finite element model. Finally, the effect of interfacial adhesion on the formability of sandwich composites was investigated, from which the optimal condition for interfacial adhesion (in terms of ensuring the formability of the sandwich composite) was obtained.

In Chapter 3, a progressive pseudograin damage accumulation (PPDA) model is proposed to predict the fatigue life of short fiber-reinforced plastics (SFRPs), combining viscoelastic-viscoplastic (VEVP) two-step homogenization theory with Chaboche fatigue damage model. Each representative volume element (RVE) of

SFRPs is decomposed into pseudograins using a two-step homogenization framework. Then, the fatigue life of each pseudograin is predicted using a master S-N curve, which is prepared based on the “normalized fatigue factor” taking into account both the stress ratio and multiaxial stress state. Thereafter, the overall failure of RVE is predicted by a PPDA model, in which each pseudograin fails progressively considering the stress concentration of the living pseudograins, resulting in non-linear fatigue damage evolution. Finally, the PPDA model is successfully implemented into ABAQUS user material subroutine (UMAT), predicting the fatigue lifetime in good agreement with experimental data.

In Chapter 4, the progressive pseudograin damage accumulation (PPDA) model is expended to predict the creep and creep-fatigue interaction effect of SFRPs. Nonlinearity in creep and fatigue interaction are investigated. Each representative volume element (RVE) of SFRPs is decomposed into pseudograins using a two-step homogenization framework. Then, the creep and fatigue life of each pseudograin is predicted using a master curve, which is prepared based on the Tsai-Wu effective stress and “normalized fatigue factor”. Thereafter, the overall failure of RVE is predicted by a PPDA model. The PPDA model is successfully implemented into ABAQUS user material subroutine (UMAT), predicting the creep lifetime and creep-fatigue interaction effect of SFRPs in good agreement with experimental data.

Chapter 2. Damage detection and a forming limit diagram

2.1. Delamination-based forming limit diagram

Various forming methods have been used to produce metal–polymer sandwich composites such as deep drawing [72], injection forming [73] and roll bonding [74]. Furthermore, incremental forming was recently developed to extend forming potential of the sandwich laminates [75]. Despite these manufacturing techniques, various failure mechanisms such as delamination, skin sheet cracking, and core polymer failure are major obstacles that make it difficult to accurately form sandwich composite parts. Delamination, in particular, occurs during forming process due to the different lengths of the metal skin layers, resulting in high shear forces in the interfaces [76]. Therefore, it is essential to characterize the formability of sandwich composites considering delamination to evaluate forming methods effectively.

Extensive researches have been conducted on characterizing forming limit of metal–polymer sandwich composites. One of the most widely used to characterize formability of sheet material is forming limit diagram (FLD) [77]. The FLD shows the criterion for major and minor strains that can be formed without failure. Many researches have been conducted on investigating the effect of change in constituent of sandwich composites [34-45]. Typically, the FLD is built by analyzing the failure of bottom metal sheet [43, 78]. Furthermore, studies have shown that increasing the core thickness improves the formability [35, 38], and that the mechanical properties of the core polymer can also improve the formability of metal–polymer sandwich composites [34, 79].

Kazemi et al. performed Nakazima test of steel–polyethylene sandwich composites and observed noticeable delamination based on the SEM investigation [80]. However, since the SEM image was observed after all fractures had occurred, the forming limit at the moment of delamination could not be observed. As a result, delamination was not considered in their FLD. [81] constructed an FLD for a multilayer sheet material (steel–polyvinyl chloride–polyethylene terephthalate) based on delamination. They used a CCD camera during the forming process to optically observe the moment of delamination between the steel and polymer–coated layers, but only the delamination to the surface was observed. To construct a FLD of sandwich composites based on delamination, a technique to detect both surface and subsurface delamination during the forming process is required.

This study proposes a new process for constructing the FLD of a steel–polymer sandwich composites based on delamination. The acoustic emission (AE) technique was used to detect delamination during formability testing. First, several tests were carried out to identify the characteristic AE features associated with the failure modes of the sandwich composites. Then, a punch test was performed with AE monitoring. Using the AE signals of delamination, a new FLD of the steel–polymer sandwich composites was constructed. Additionally, the formability tests were simulated using the cohesive zone model to consider interfacial properties, and the effect of interfacial adhesion on the formability of the sandwich composite was investigated.

2.2. Methods

2.2.1. Sandwich composites preparation

An electrogalvanized (EG) steel sheet with a thickness of 0.6 mm was used as the skin material for the sandwich composite. A polyamide-6 (PA) sheet with a thickness of 1 mm was used as the core material. The total thickness of the EG steel–PA–EG steel (EG–PA–EG) sandwich composite was 2.2 mm. A cyanoacrylate adhesive, Loctite 401, was used to bond the skin and core sheets together. After adhesive applied, sandwich sheet was heated at 120℃ with 0.0015 MPa pressure for 3 hours.

2.2.2. Punch test procedure

Hemispherical punch test was selected as the forming process of steel–polymer composites in this study. **Figure 2-1(a)** shows the punch test set-up based on a 100-kN Instron™ universal testing machine. The diameter of the hemispherical punch was 50 mm and that of the die cavity was 56.5 mm.

A specimen was placed on the die and then clamped by the blank holder using nuts and bolts. The beads on the blank holder ensured that the specimen did not slip. The punch descended at a crosshead speed of 10 mm/min. Sandwich composite specimens prepared for the Nakajima forming test are shown in **Figure 2-1(b)** [82].

Circular specimens 100 mm in diameter, and hourglass-shaped specimens with neck widths of 10, 20, 30, 40, and 50 mm, were used. Due to their geometrical shape, each specimen was designed to have different strain paths from uniaxial to biaxial tension.

Circular (3-mm-diameter) grids were printed on specimens using a stamp (**Figure 2-1(c)** left). The grid on deformed ("failed") specimens was transferred to a flat surface using tape. The major and minor strains were identified by measuring the deformed grids on the tape. Safe and neck/fracture regions were determined [83]. The nearest unnecked grids were considered as safe regions, while necked and fractured grids were classified as neck/fracture regions (see **Figure 2-1(c)** right). Then, the forming limit curve was plotted above the strains of the safe region and below the strains of the neck/fracture region.

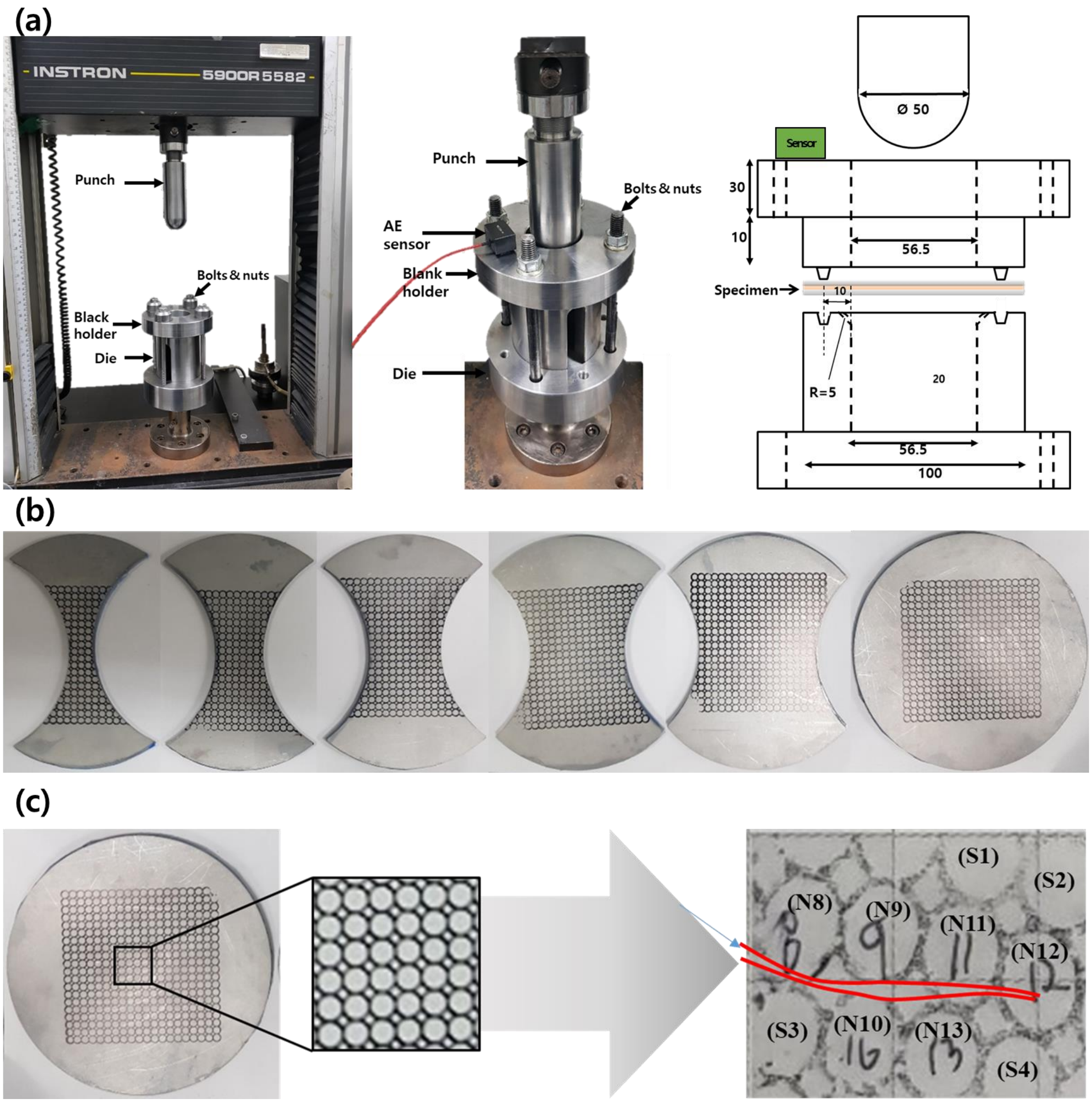

Figure 2-1 (a) Punch test set-up, (b) specimen geometry for the Nakazima punch test, and (c) circfular grids printed on the specimen with a stamp (left) and grids of the deformed specimen (right).

2.2.3. Observing delamination using acoustic emission

2.2.3.1. Equipment

An AE system was used to establish the moment of delamination during the punch test (**Figure 2-2(a)**). First, a broadband-type transducer (M204A; Fuji Ceramics Corporation, Japan) collected wave signals. The transducer had a diameter of 5.5 mm and operated at 10–600 kHz. Then, a Fuji Ceramics Corporation amplifier amplified the AE signal. A single-channel Mistras 1283 USB AE Node data acquisition board (Physical Acoustic Corporation, USA) was used to record the AE data. Acoustic emission software (WIN; Mistras, USA) was used to analyze the wave signals. To ensure good acoustic coupling, silicone grease was applied to the surface of the transducer, which was fixed to a magnetic support. The intensity of wave acquisition was calibrated using a pencil-break test.

2.2.3.2. Test procedures

We conducted two types of tests to obtain acoustic emission (AE) signal features. The first type of test involved performing tensile tests on monolithic layers of steel (T-EG) and polymer (T-PA) according to ASTM E8 [84] and D638 [85] standards, respectively. The geometry of the steel and polymer specimens used in these tests are shown in **Figure 2-2(b)** and **(c)**, respectively. Punching tests of monolithic EG steel (P-EG) were also conducted to confirm that the AE signal features are generated in the punching test environment. The sensor was attached to the blank holder as shown in **Figure 2-2(a)**.

For the second type of test, delamination of sandwich composites was induced using the lap shear test (T-LS) according to the ASTM D3164 [86] standard, and the geometry of the lap shear specimen is shown in **Figure 2-2(d)**. Tensile testing of the steel–polymer sandwich composites with (T-SC-W) and without (T-SC-WO) adhesion was also conducted with the specimen geometry shown in **Figure 2-2(b)**. Next, the punch shear test specimen (P-LS) was designed such that delamination was the primary failure mode (**Figure 2-2(e)**). When the hemispherical punch pushed the middle region of the specimen, shear force was generated between the steel and polymer layers, and delamination finally occurred. The sensor was attached to the blank holder as shown in **Figure 2-2(a)**.

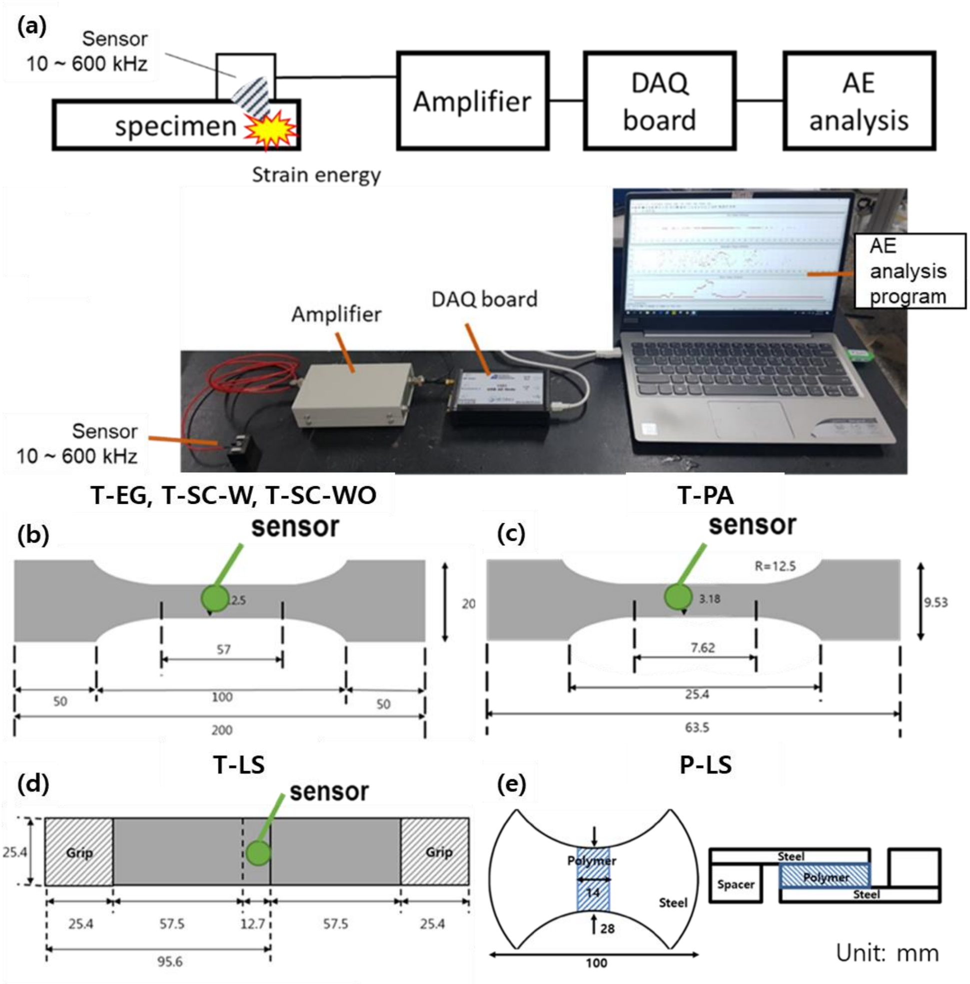

Figure 2-2 (a) Acoustic emission (AE) test set-up. (b) Steel and composite tensile specimens (T-EG, T-SC-W, T-SC-WO), (c) polymer tensile test specimen (T-PA), (d) lap shear test specimen (T-LS), and (e) punch shear test specimen (P-LS) used to observe AE features.

2.2.4. Numerical simulation of punch test

Numerical FLD of steel–polymer composite was constructed to compare with experimental results and confirm the theoretical validity of experimental FLD. Additionally, we used the numerical FLD to investigate the influence of interfacial properties on the formability of the sandwich composites. In Section 2.2.4.1, built-in models used to simulate the punch test are introduced, followed by the material parameter identification for these models in Section 2.2.4.2.

2.2.4.1. Numerical model

To simulate the punch test, finite element analysis software (ABAQUS, Simulia Inc) was used. Following the actual experiments, three-dimensional solid models were generated; the geometries of the model and specimen are provided in **Figure 2-3(a)**. An example of punch test simulation result and strain measurement region is shown in **Figure 2-3(b)**. Delamination between the steel skin and core polymer was considered in the cohesive element layer. The thickness of this layer was set to be 0.001 mm.

Isotropic elastic, J2 plastic, ductile failure criterion, and damage evolution built-in models were used to simulate steel and polymer behaviors. J2 plasticity model is adequate for simulating the properties of the core polymer in the punch test since the effect of temperature and strain rate are negligible. The ductile failure criterion, a phenomenological model, was used to predict the onset of material damage as suggested by [87]. Equivalent plastic strain was determined as a function of stress triaxiality (η) using **Equation (1).** When **Equation (2)** was satisfied, softening of the yield stress and degradation of elasticity occurred [88]

$$\bar{\varepsilon}_D^{pl}(\eta) = \frac{\varepsilon_T^{+}\sinh\left[k_0\left(\eta^{-}-\eta\right)\right]+\varepsilon_T^{-}\sinh\left[k_0\left(\eta-\eta^{+}\right)\right]}{\sinh\left[k_0\left(\eta^{-}-\eta^{+}\right)\right]} \tag{1}$$

$$\int \frac{d\bar{\varepsilon}_D^{pl}}{\bar{\varepsilon}_D^{pl}\left(\eta\right)} = 1 \tag{2}$$

Previous researches have simulated the delamination in metal–polymer sandwich composites using cohesive zone model [89, 90]. This model involves the use of cohesive elements that determine delamination according to the traction–separation law [91]. Among various types of traction–separation laws, a bilinear law was selected due to its efficiency with respect to CPU time. The bilinear law consists of two stages. In the pre-delamination stage, the cohesive element follows elastic traction-separation relations given by:

$$\begin{pmatrix}\sigma_n\\ \sigma_t\\ \sigma_l\end{pmatrix} = \begin{pmatrix}\boldsymbol{K}_n & 0 & 0\\ 0 & \boldsymbol{K}_t & 0\\ 0 & 0 & \boldsymbol{K}_l\end{pmatrix}\begin{pmatrix}\delta_n\\ \delta_t\\ \delta_l\end{pmatrix} \tag{3}$$

where σ and δ represent traction and separation, respectively, and n, t, l denote the normal, tangential and longitudinal directions. $\boldsymbol{K}$ denotes the interfacial stiffness. When the traction in cohesive element reaches the maximum traction, delamination is initiated, and the post-delamination stage begins. Delamination propagates until the energy release rate reaches the critical fracture energy. The energy release rates are expressed as:

$$\boldsymbol{G}_i = \int \boldsymbol{\sigma}_i d\boldsymbol{\delta}_i \,, \quad i = n,t,l \tag{4}$$

The quadratic criterion (**Equation (5)**) suggested by (Ye, 1988) was used to evaluate the failure initiation value that induces delamination. the power law criterion (**Equation (6)**) suggested by (Long, 1991) was used to evaluate failure propagation criterion for continued delamination.

$$\sum \left(\frac{\boldsymbol{\sigma}_i}{\boldsymbol{\sigma}_{i.c}} \right)^2 = 1 \,, \quad i = n,t,l \tag{5}$$

$$\sum \left(\frac{\boldsymbol{G}_i}{\boldsymbol{G}_{i.c}} \right)^2 = 1 \,, \quad i = n,t,l \tag{6}$$

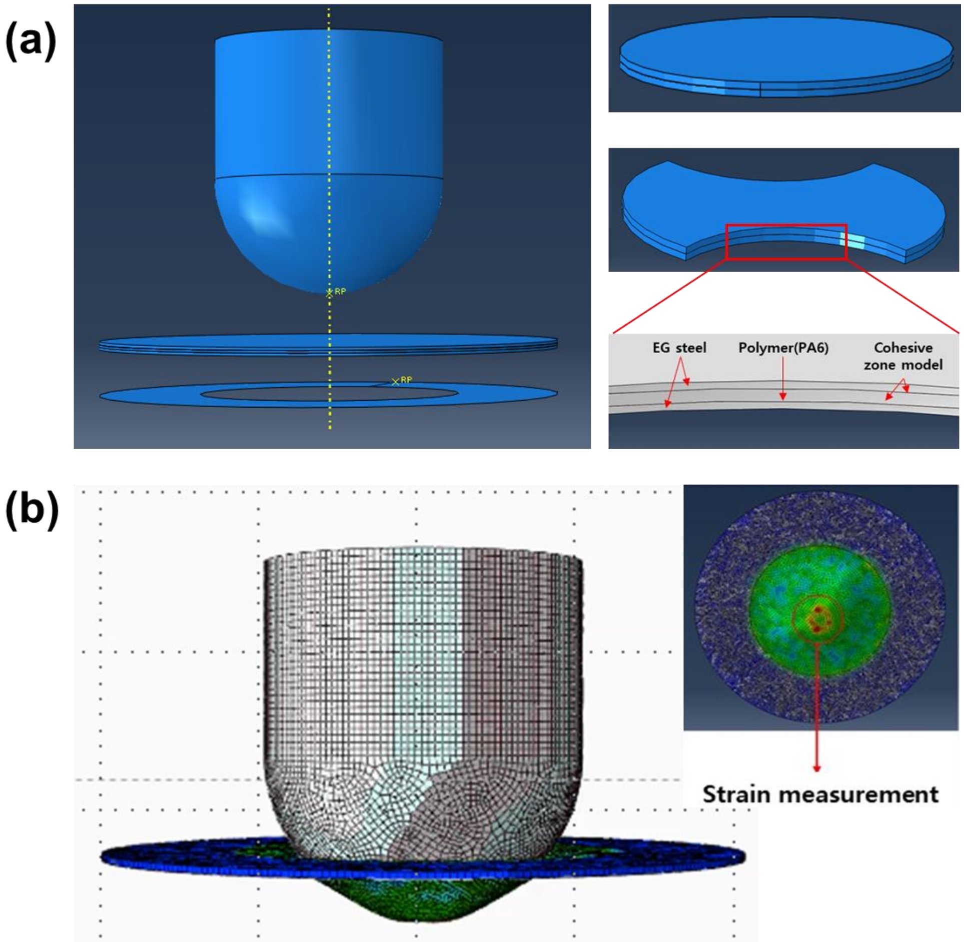

Figure 2-3 Simulation models for the (a) punch test and steel–polymer sandwich composite. (b) An example of punch test simulation result.

2.2.4.2. Material parameter identification

Tensile tests were conducted on monolithic steel and PA sheets, and the resulting material parameters are presented in **Table 2-1**. Using these material parameters and the models described earlier, tensile tests were re-simulated, and the results have a good agreement with the measurements, as shown in **Figure 2-4(a)** and **(b).**

To determine four interfacial properties ($\boldsymbol{\delta_{n,c}}$, $\boldsymbol{\delta_{t,c}} = \boldsymbol{\delta_{l,c}}$, $\boldsymbol{G_{n,c}}$, $\boldsymbol{G_{t,c}} = \boldsymbol{G_{l,c}}$) required for the bilinear law, four different experiments were carried out including butt joint, lap shear, double cantilever beam, and end-notched flexure tests [92]. The interfacial stiffness for the cohesive element was set to be 10^6 N/mm3 following the previous studies [93-95]. All material constant values for the cohesive zone model are provided in **Table 2-2**. The butt joint and lap shear tests were then re-simulated, and results were in good agreement with the measurements, as shown in **Figure 2-4(c)** and **Figure 2-4(d)**.

(a)

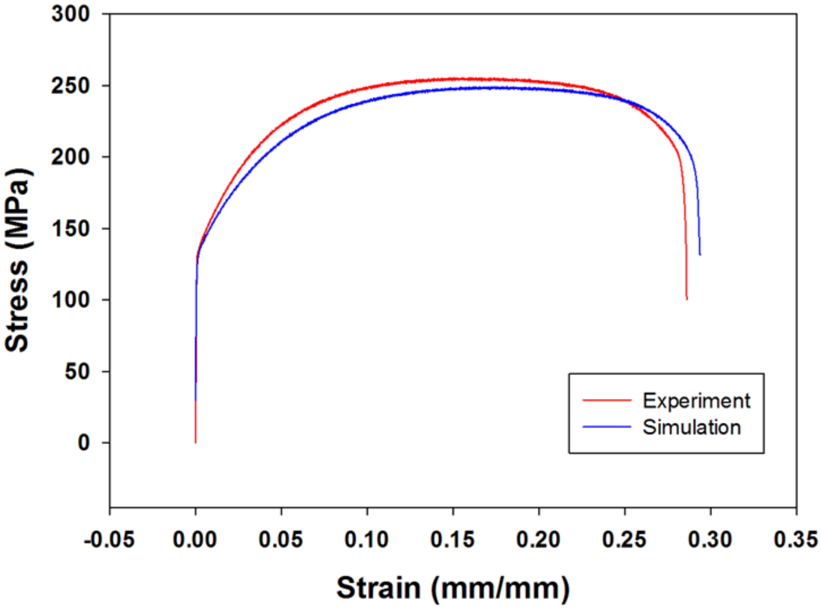

Stress (MPa)
Strain (mm/mm)
Experiment
Simulation

(b)

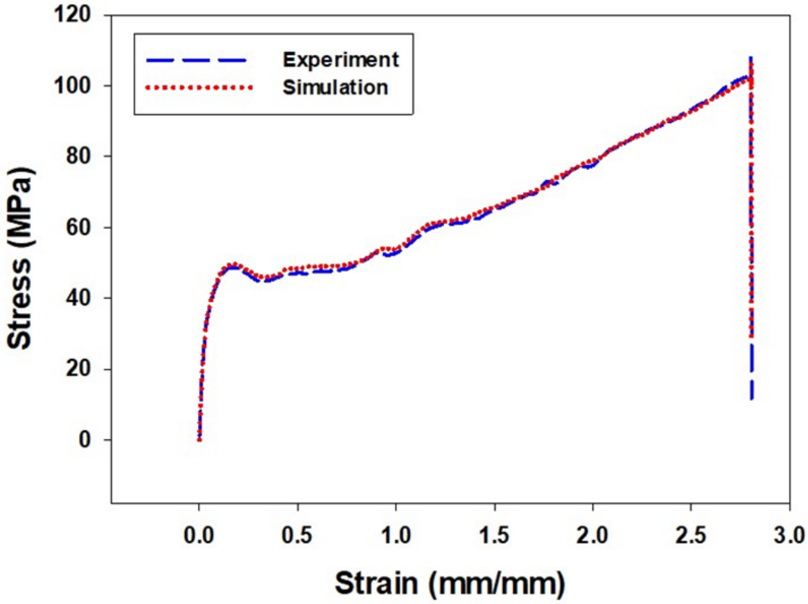

Stress (MPa)
Strain (mm/mm)
Experiment
Simulation

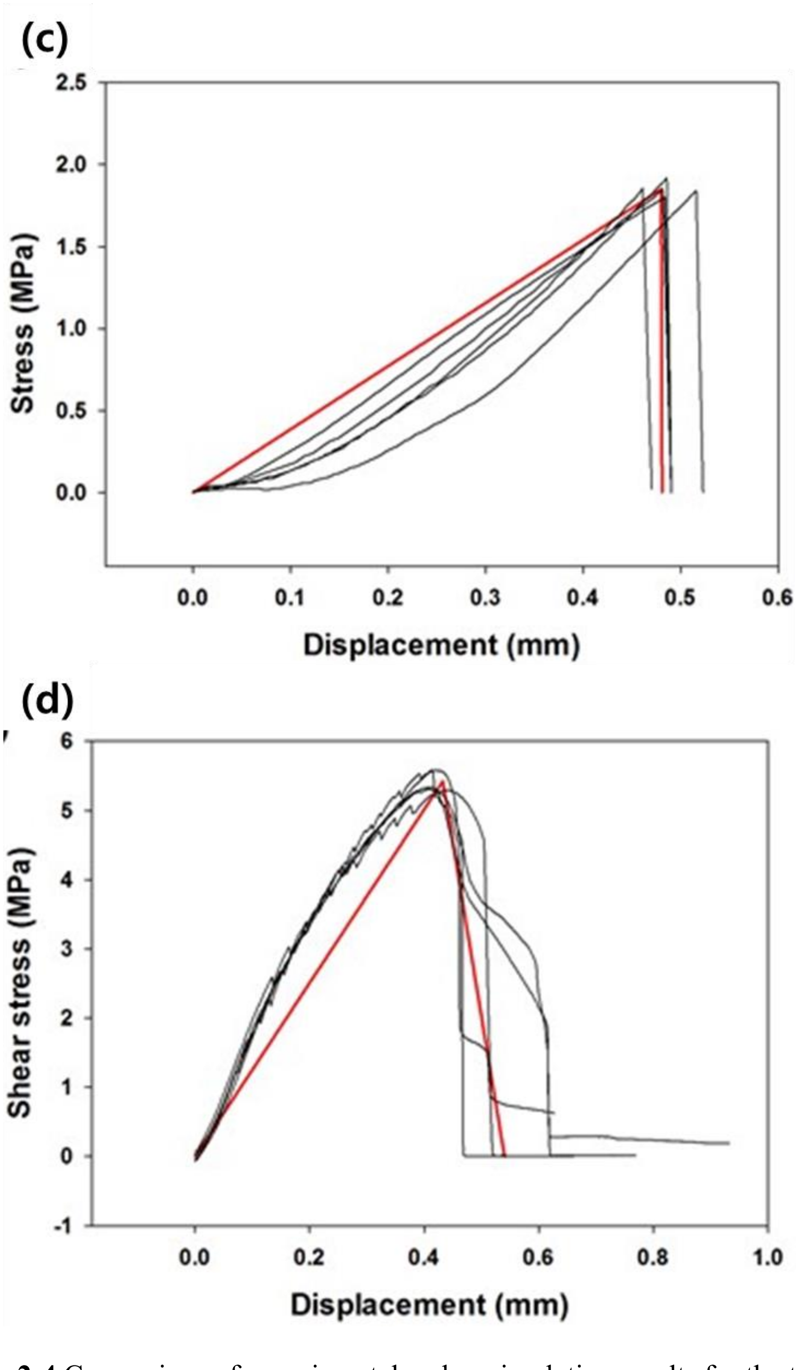

Figure 2-4 Comparison of experimental and re-simulation results for the tensile behavior of (a) steel and (b) polymer, and the results of (c) butt joint and (d) lap shear tests.

Table 2-1 Material parameters of EG steel used for the simulations.

<table>
<tr><td colspan="12">Elastic-plastic behavior</td></tr>
<tr><td colspan="3">Elastic modulus</td><td colspan="3">Poisson's ratio</td><td colspan="3">Yield strength</td><td colspan="3">Tensile strength</td></tr>
<tr><td colspan="3">190 GPa</td><td colspan="3">0.3</td><td colspan="3">130 MPa</td><td colspan="3">250 MPa</td></tr>
<tr><td colspan="12">Ductile damage</td></tr>
<tr><td colspan="4">Failure strain</td><td colspan="4">Stress triaxiality</td><td colspan="4">Strain rate</td></tr>
<tr><td colspan="4">0.29</td><td colspan="4">0.33</td><td colspan="4">0.02 s^{-1}</td></tr>
<tr><td colspan="12">Damage evolution</td></tr>
<tr><td colspan="6">Fracture toughness</td><td colspan="6">10 N/mm</td></tr>
</table>

Table 2-2 Material parameters required by the cohesive zone model.

<table>
<tr><td></td><td>Mode I</td><td>Mode II</td><td>Mode III</td></tr>
<tr><td>Failure strength (MPa)</td><td>1.85</td><td colspan="2">5.36</td></tr>
<tr><td>Fracture toughness (N/mm)</td><td>0.36</td><td colspan="2">0.8</td></tr>
<tr><td>Stiffness (N/mm^3)</td><td colspan="3">10^6</td></tr>
<tr><td>Mesh size (mm)</td><td colspan="3">0.01</td></tr>
</table>

2.3. Results and discussion

2.3.1. AE signal features

Previous studies have utilized five AE parameters (amplitude, duration, energy, rise time, and peak frequency) to classify the failure modes of composite materials. Among these parameters, peak frequency has been identified as the most significant by researchers such as [96], [97] and [98]. Therefore, in this study, we transformed AE signals to frequency domain using fast Fourier transform (FFT) to extract peak frequency information. The method for identifying delamination AE signal features using peak frequency will be described below.

An example of AE signals obtained from T-EG is shown in **Figure 2-5(a)**, and its FFT result is shown in **Figure 2-5(b)**. First, the time at which the AE signals was generated was plotted on the x-axis, and the peak frequency of the AE signals was plotted on the y-axis to create a peak frequency plot. Next, the peak frequency plot was overlaid with the load-time plot to generate a peak frequency distribution plot. **Figure 2-5(c)** shows the peak frequency distribution plot of the T-EG as an example. The peak frequency distribution plot of each test is analyzed, and the "frequency bands" are defined by clustering the peak frequency that appears repeatedly, to be used for classification of failure mechanisms. For each test, frequency bands are visually defined: frequency between 10 and 50 kHz (blue band); frequency between 70 and 200 kHz (green band); and frequency between 300 and 500 kHz (red band). For an example frequency bands of T-EG are shown in **Figure 2-5(d)**.

The peak frequency band plot for the tests conducted in Section 2.2.3.2 are presented in **Figure 2-5(d)** and **Figure 2-6**. The blue and green frequency bands are visible in all the tests. In the case of T-EG, T-PA, P-EG, T-SC-W, and T-SC-WO, these bands begin at the onset of both steel and polymer fractures, as shown in **Figure 2-5(d)**, **Figure 2-6(a)**, **(b)**, **(e)** and **(f)**. Thus, these frequency bands can be considered as characteristic features of steel and polymer fractures.

The red frequency band was observed in the T-LS and P-LS tests, and it was continuously generated throughout these tests. Therefore, the red frequency band is considered an indicator of delamination.

When comparing T-SC-W and T-SC-WO, it was found that the steel–polymer composite specimens containing adhesive between layers displayed an additional red frequency band at the same time as steel fracture, which was not observed in the specimens without adhesive. In T-SC-W, it was observed from the specimen broken that delamination had occurred, as shown in **Figure 2-7(a)**. Furthermore, numerical simulation of T-SC-W showed that delamination was observed slightly before the steel skin was broken, as shown in **Figure 2-7(b)**. The time at which delamination occurred coincided with the time at which the AE signals appeared in **Figure 2-6(e)**.

The peak frequency bands of each failure mode in the steel–polymer sandwich composites are listed in **Figure 2-8**; these were then used to detect delamination during formability testing and construction of an FLD considering delamination.

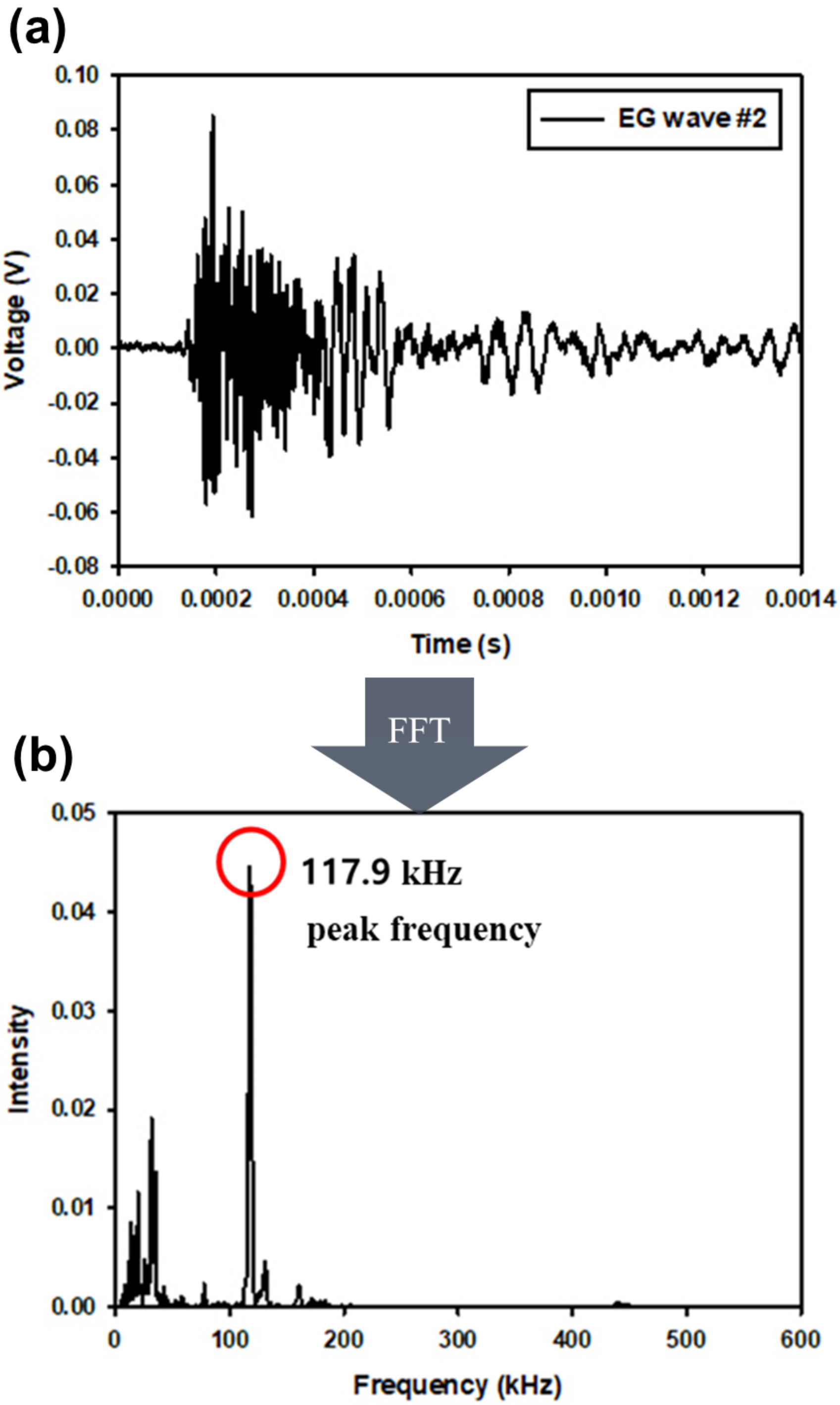
(a)
EG wave #2
Voltage (V)
Time (s)
FFT
(b)
117.9 kHz
peak frequency
Intensity
Frequency (kHz)

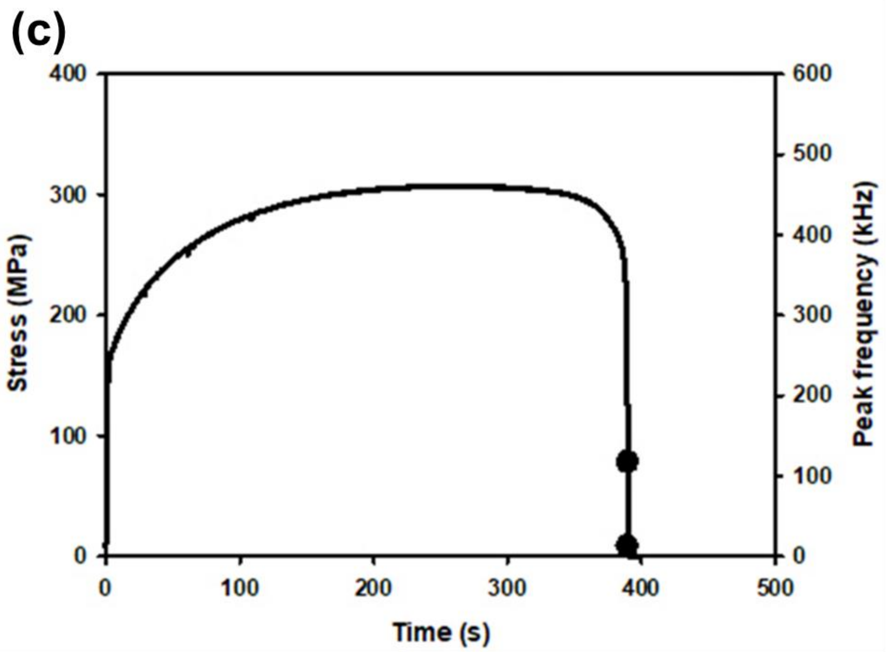

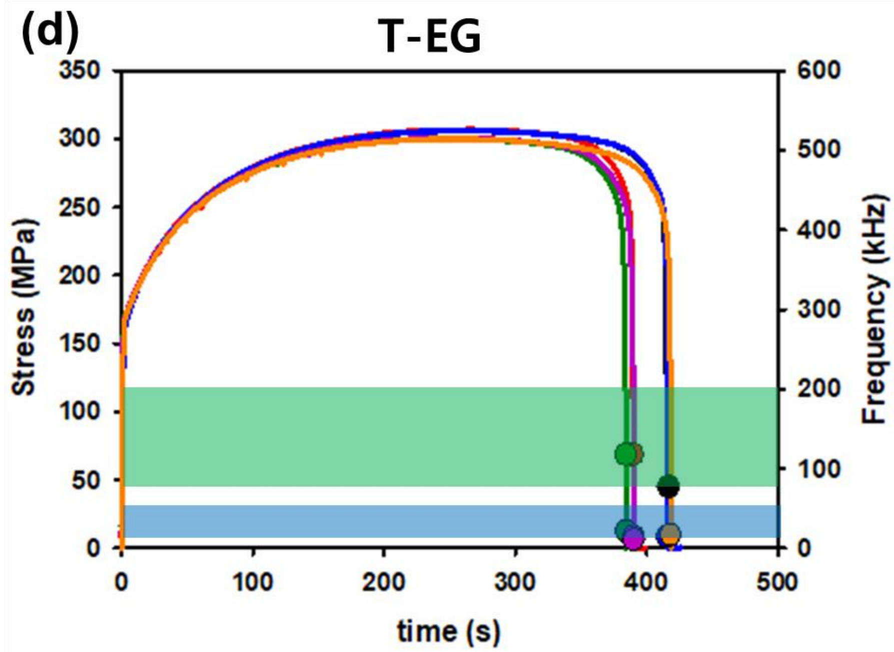

Figure 2-5 (a) AE waveform recorded, (b) fast Fourier transform result of the waveform, (c) peak frequency distribution plot, and (d) peak frequency band plot of T-EG.

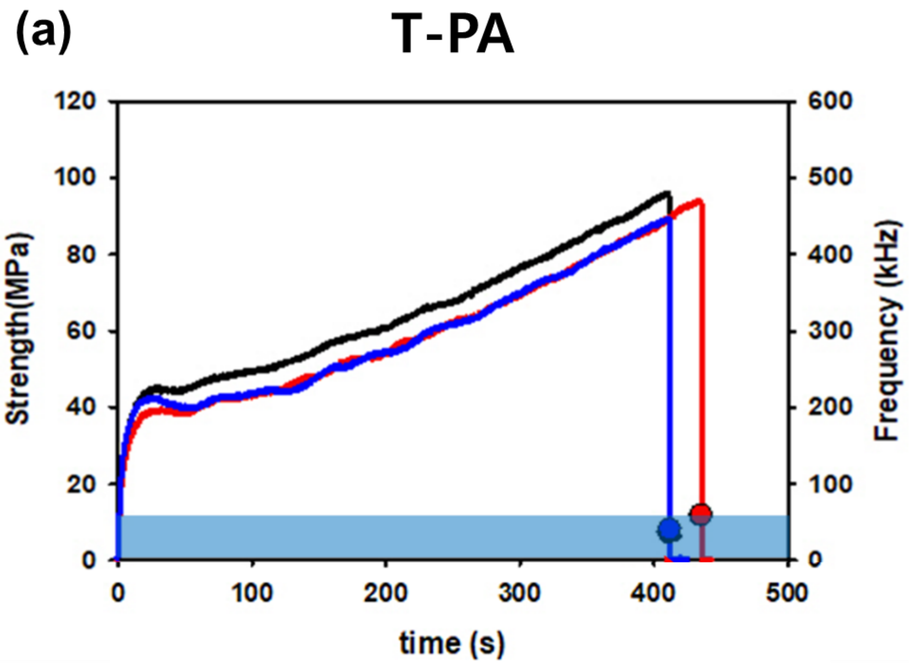
(a)
T-PA
Strength(MPa)
Frequency (kHz)
time (s)
0
20
40
60
80
100
120
0
100
200
300
400
500
600
0
100
200
300
400
500

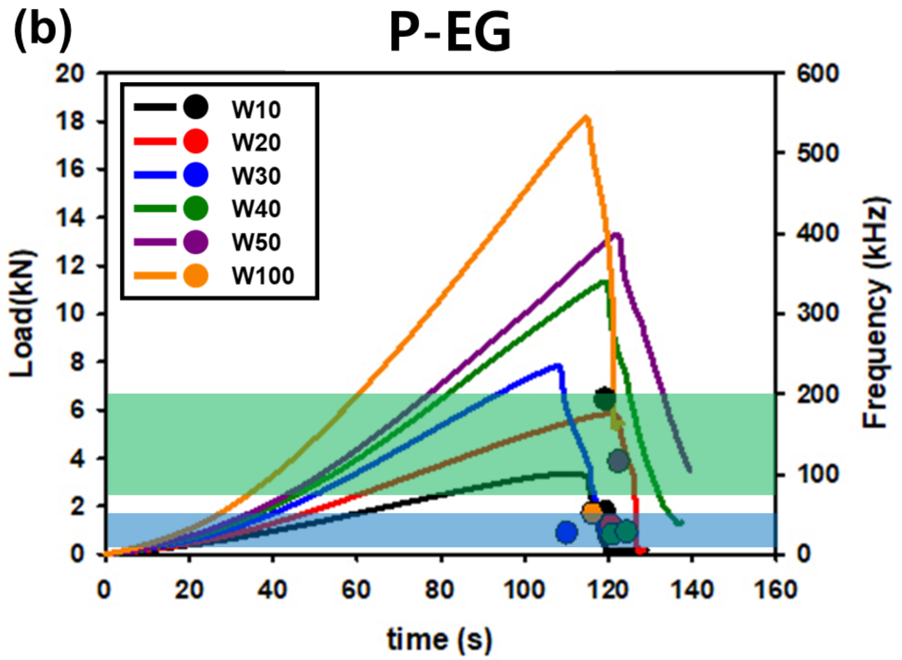
(b)
P-EG
Load(kN)
Frequency (kHz)
time (s)
W10
W20
W30
W40
W50
W100
0
2
4
6
8
10
12
14
16
18
20
0
100
200
300
400
500
600
0
20
40
60
80
100
120
140
160

(c)

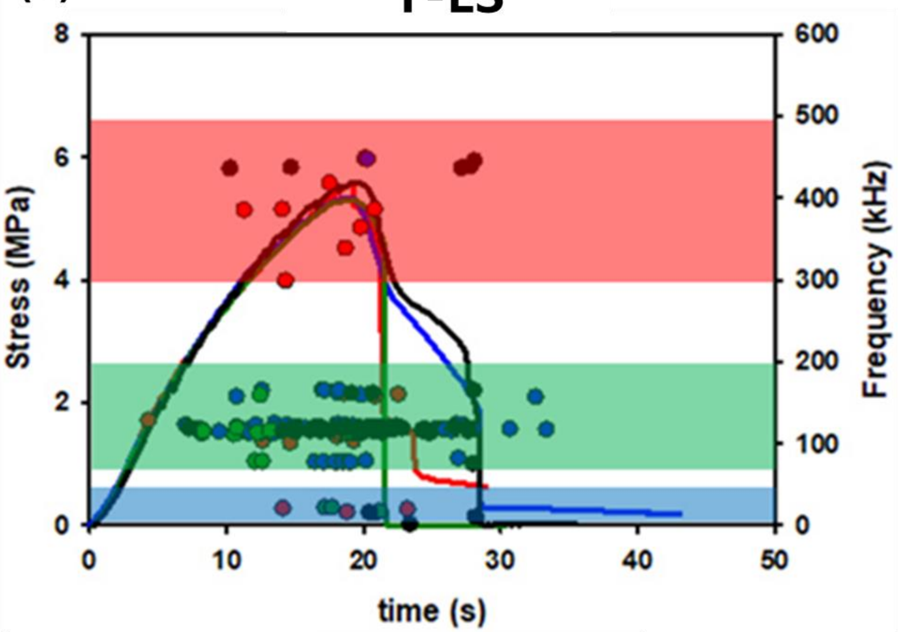
T-LS
Stress (MPa)
Frequency (kHz)
time (s)
0
2
4
6
8
0
100
200
300
400
500
600
0
10
20
30
40
50

(d)

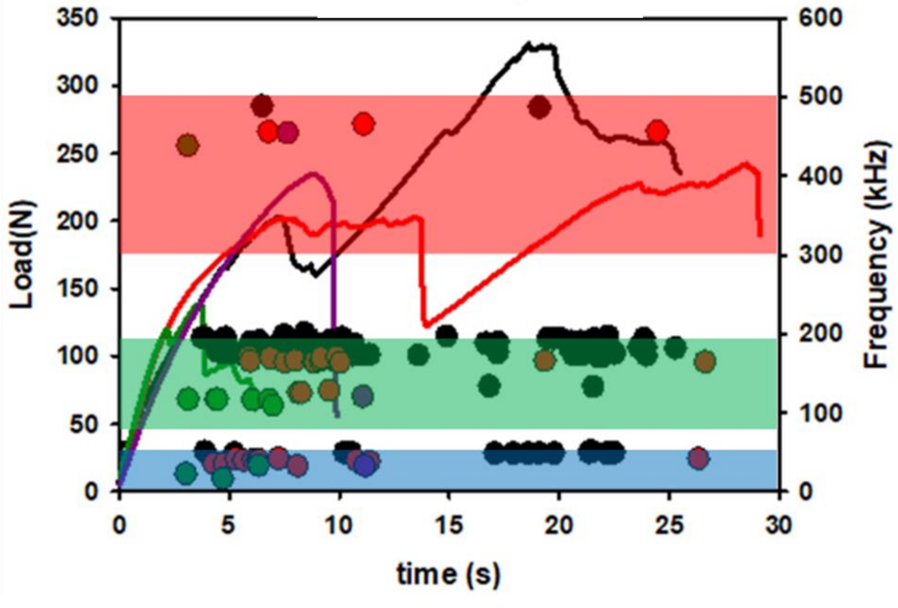
P-LS
Load(N)
Frequency (kHz)
time (s)
0
50
100
150
200
250
300
350
0
100
200
300
400
500
600
0
5
10
15
20
25
30

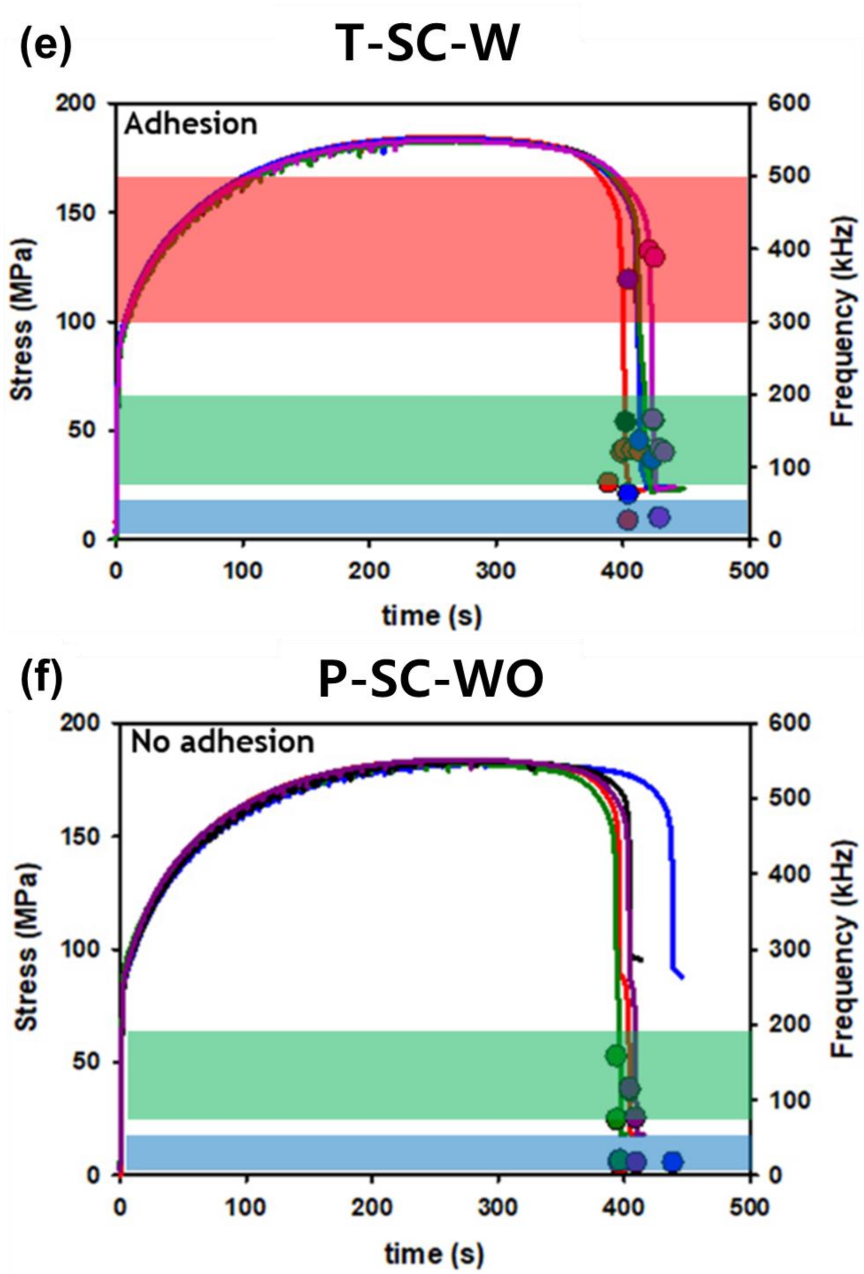

Figure 2-6 Peak frequency band plots of (a) polymer tensile test (T-PA), (b) steel punch test (P-EG), (c) lap shear (T-LS) and (d) punch shear tests (P-LS). Peak frequency band plots of a steel–polymer composite tensile test. Specimens (e) with adhesive (T-CS-W) and (f) without adhesive (T-CS-WO).

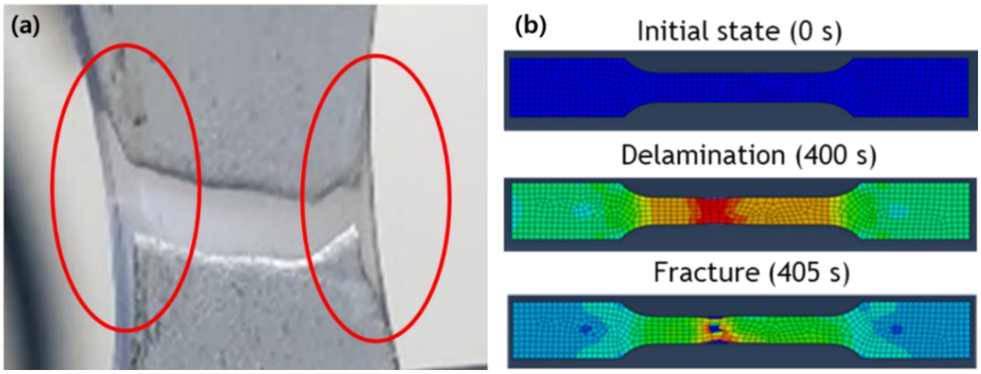

Figure 2-7 (a) Observed delamination area after tensile testing of the steel–polymer sandwich composite (T-SC-W) and (b) results of numerical simulation.

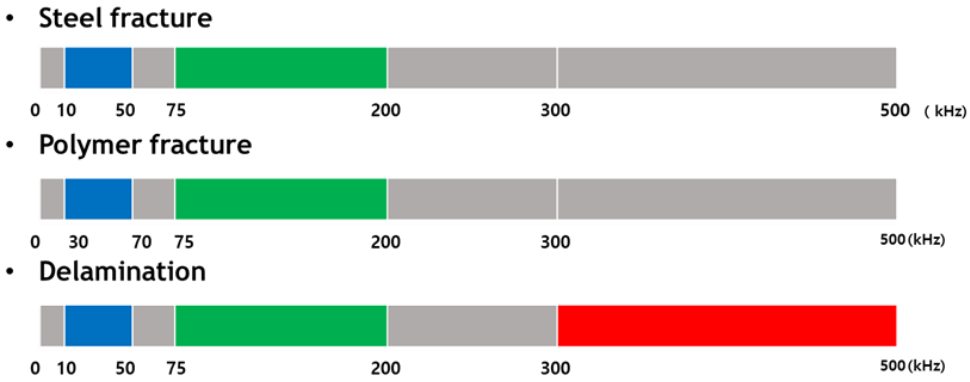

Figure 2-8 Peak frequency bands of each failure mode for the steel–polymer sandwich composite.

2.3.2. Forming limit diagram based on fracture of bottom steel

After the punching test, deformed EG–PA–EG sandwich composite specimens exhibited both steel fracture and delamination, as shown in **Figure 2-9**. In this section, the formability of steel–polymer sandwich composites considering the fracture of the bottom steel is investigated. The experimental FLDs of the EG monolayer and EG–PA–EG sandwich composite are shown in **Figure 2-10(a)** and **(b)**, respectively. It is shown that the formability of the composite was improved compared to that of the monolayer skin, as observed in other studies of metal–polymer sandwich composites [99, 100]. This can be explained by an initial defect parameter, which is one of the major parameters affecting the formability of a sheet material [101]. As thickness of sandwich composites is larger than that of monolithic steel, initial defect becomes smaller and therefore, FLC of the sandwich composite shifted upward.

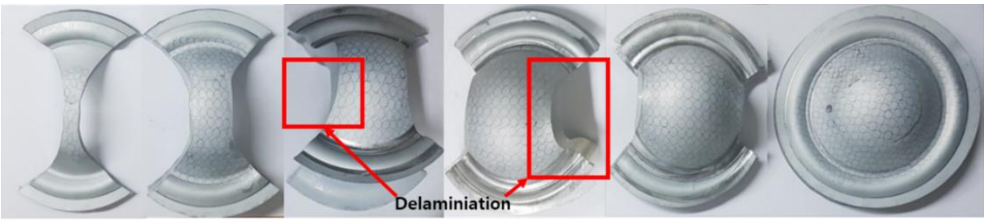

Figure 2-9 Deformed specimens after the punch test.

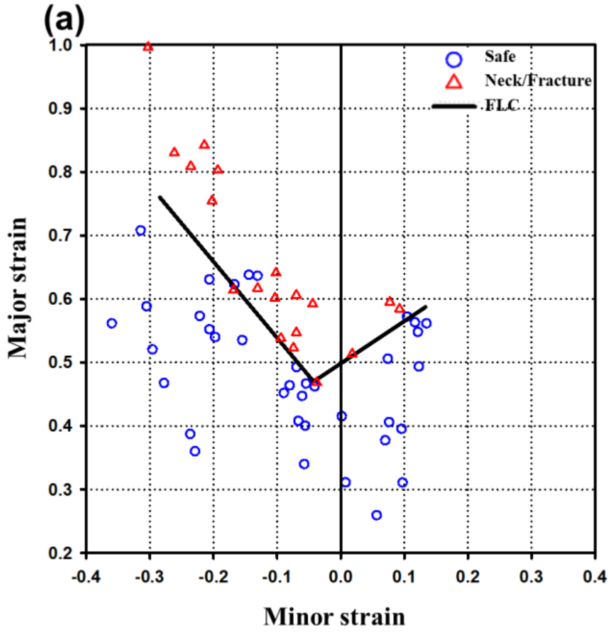

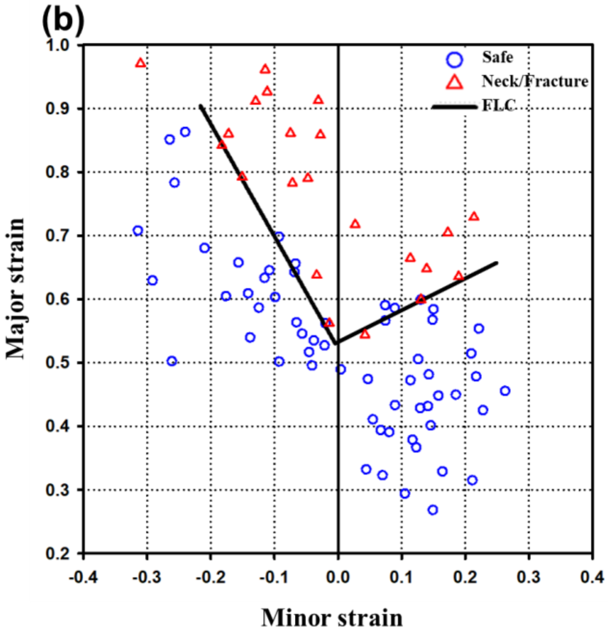

Figure 2-10 Experimental forming limit diagram (FLD). (a) Electrogalvanized (EG) monolayer steel sheet and (b) EG steel–polyamide-6–EG steel (EG–PA–EG) sandwich composite.

2.3.3. Forming limit diagram based on acoustic emission delamination signals

In this section, the formability of steel–polymer sandwich composites considering delamination is investigated. The load versus displacement plots obtained from the tests are overlaid with the peak frequency band plot of AE signals during the punching test. They are shown in **Figure 2-11(a)–(f)**. The red frequency band in the plot corresponds to the peak frequency band of delamination obtained from Section 2.3.1. The dashed line in the plot represents the average displacement of AE signals whose peak frequency falls within the range of the red band. Therefore, the dashed line indicates the moment of delamination during the punch test. In the W10 specimen, delamination occurred almost simultaneously with steel fracture, while in the W40 specimen, delamination occurred 4.5% earlier than steel fracture. No AE signals corresponding to delamination were observed in the W100 specimen. Based on these observations, it was concluded that delamination rarely occurred under biaxial and uniaxial tension conditions. However, delamination was likely to occur rapidly when the minor strain of the sandwich composite approached zero.

To construct experimental FLD considering delamination, punch displacement corresponding to the dashed line in **Figure 2-11(a)–(f)** was applied in the punch test. Then, major and minor strains of each specimen were measured. Finally, FLD based on delamination constructed as shown in **Figure 2-12**. The FLD constructed by considering delamination (black dash line) was slightly lower than that based on skin steel fracture (black solid line). Therefore, it should be noted that if the AE features of failure mechanisms are identified through pre-tests, the Nakazima test with AE sensors can be used to characterize the formability of steel–polymer sandwich composites considering both steel fracture and delamination.

A numerical FLD with interfacial properties was developed, as shown in **Figure 2-12**. The FLD constructed by considering delamination was slightly lower than that based on specimen fracture, which was consistent with the experimental results. Although there was a slight difference between the uniaxial and biaxial tension conditions, the FLDs showed good agreement over a wide range of minor strain (from -0.1168 to 0.1360).

Simulations were conducted to determine the effect of interfacial properties on the formability of the sandwich composite and predict the necessary interfacial properties for stable formability, by varying the mode I and II failure strengths while maintaining the same ratio. The results, shown in **Figure 2-12**, indicate that the forming limit of the sandwich composite increased as the interfacial properties increased. The legend “Adhesion” represents the interfacial properties in the experiment, while the other legends indicate the multiples used to change the failure strength. In most cases, delamination at the interface occurred before specimen failure in the formability simulation, and weaker interfacial properties resulted in delamination at lower strain. Additionally, deterioration of formability due to a weak interface was greater when the minor strain approached zero. The optimal interfacial properties to ensure stable formability were indirectly identified through simulation, and the failure strengths at the interface during the formability test that prevent delamination should be at least four times higher than those of the interfacial properties confirmed experimentally.

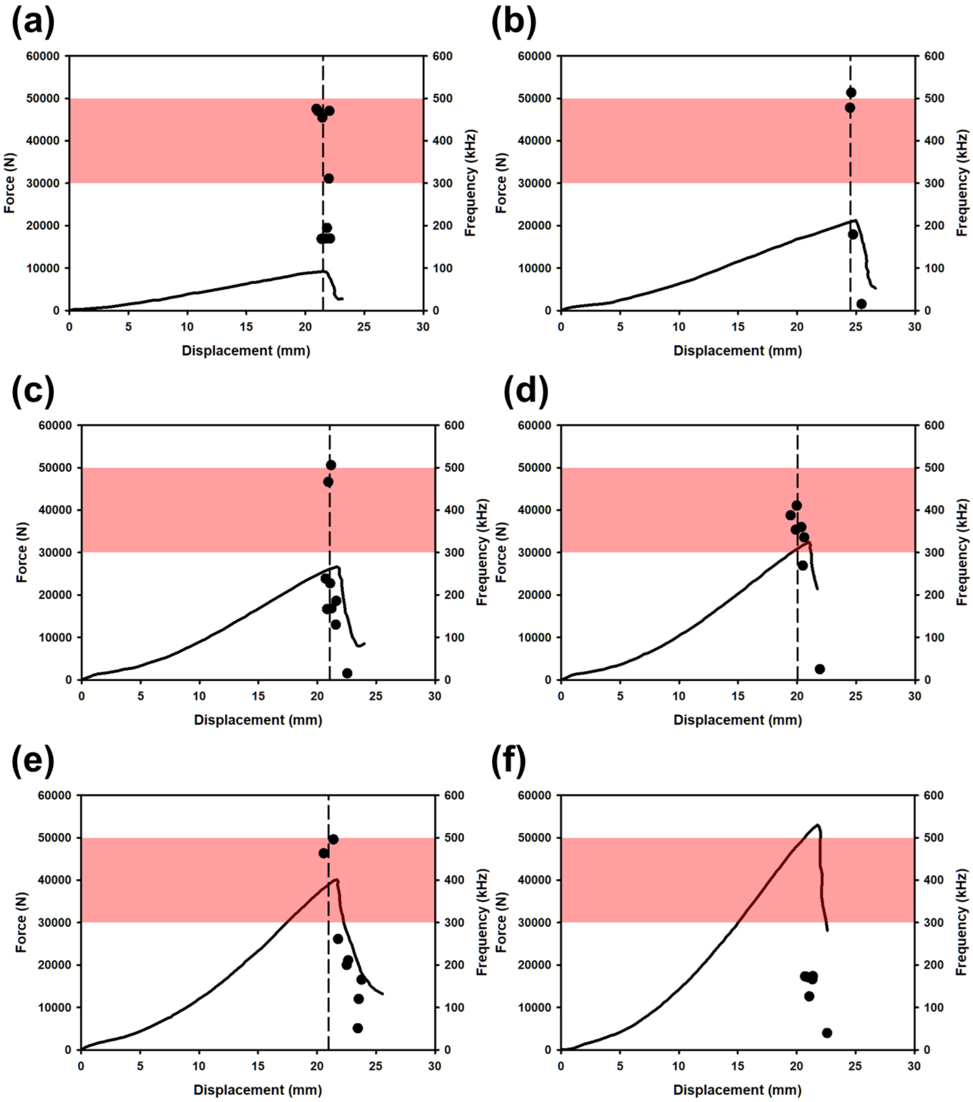

Figure 2-11 Load as a function of displacement of the steel–polymer sandwich composite showing acoustic emission signals (dots), the moment of delamination (dashed line), and the delamination peak frequency band (red band). Samples (a) W10, (b) W20, (c) W30, (d) W40, (e) W50, and (f) W100.

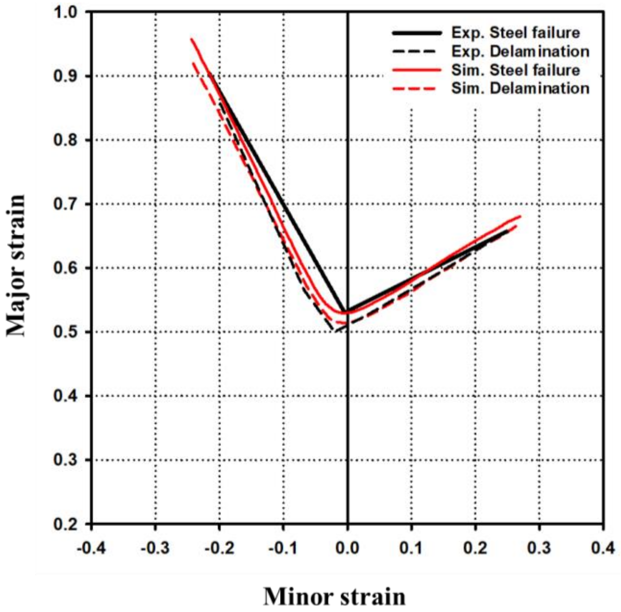

Figure 2-12 Comparison between experimental and numerical FLD using the acoustic emission signal of delamination.

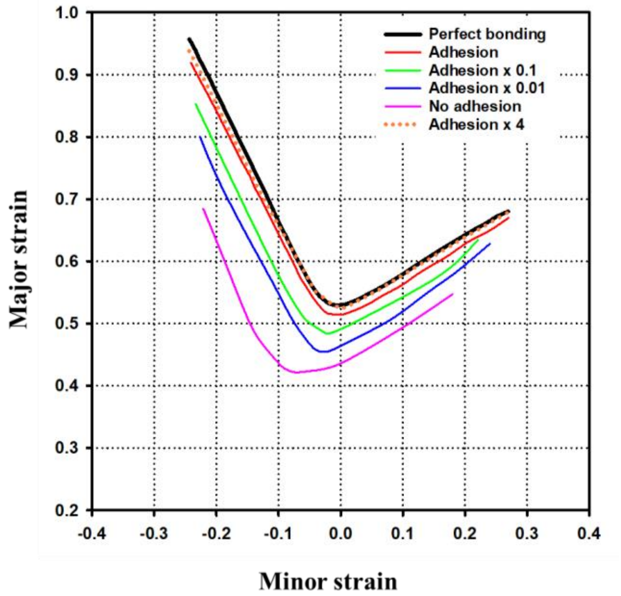

Figure 2-13 Numerical FLD as a function of adhesion. Comparison between experimental and numerical FLD using the acoustic emission signal of delamination.

2.4. Summary

In this study, we proposed a novel experimental approach for constructing forming limit diagram (FLD) to evaluate the formability of steel–polymer sandwich composites. Our approach relied on acoustic emission (AE) monitoring to detect delamination, which was identified by a peak frequency band in the range of 300-500 kHz. We also conducted numerical simulations using the cohesive zone model to investigate the effects of interfacial properties and damage on formability. Our results showed that stronger interfacial properties led to improved formability by reducing the risk of delamination. Overall, our approach provides a valuable tool for optimizing the design and processing of steel–polymer sandwich composites for various industrial applications.

Chapter 3. Fatigue life prediction of short fiber-reinforced plastics (SFRPs)

3.1. Progressive pseudograin damage accumulation (PPDA) model

Various fatigue failure models of SFRPs have been reported, which can be classified into two types: phenomenological and micromechanical models. Phenomenological models describe the fatigue behavior of SFRPs at a macroscopic level [102, 103]. Therefore, researchers have used criteria such as von Mises criteria [103], Tsai-Hill criteria [15], and Fatemi-Socie parameter [104] to describe the phenomenological fatigue failure of SFRPs. The use of these phenomenological models requires labor-intensive experiments to characterize the fatigue properties whenever the properties of constituents such as fiber volume fraction, aspect ratio or orientation tensor change. This makes such phenomenological models difficult for modeling SFRP parts that have a large difference in mechanical properties depending on the local fiber orientation [105, 106].

Micromechanical models describe the fatigue failure of SFRPs considering individual constituents (fiber, matrix, and interface). Researchers described micromechanical models considering matrix damage [107] and delamination [33, 108, 109]. In particular, Pierard et al. proposed a two-step homogenization procedure [50]. A two-step homogenization framework of viscoelastic-viscoplastic (VEVP) matrix and elastic fiber was proposed [110] and developed [111, 112] to describe non-linear behavior of SFRPs. Kammoun et al. [61, 63] suggested a pseudograin damage accumulation model with the two-step homogenization framework. Rather than defining the overall failure of whole composites, a progressive failure is modeled as successive failures of pseudograins, employing continuum damage mechanics to calculate the damage accumulation of each pseudograin. Then, the "first pseudograin damage (FPGD)" model by analogy with first-ply-failure concept for laminates was used to predict static failure of SFRPs under tensile loading. This model is suitable for predicting the failure of multiaxial loading with various fiber orientations, however, it only predicts the static failure of SFRPs, not fatigue failure.

Krairi et al. [113] proposed a fatigue failure prediction model of SFRPs using mean-field homogenization method. This model assigned a continuum damage evolution law to weak spots in the SFRPs and calculated the damage evolution using the matrix strain. The S-N curves of the SFRPs were predicted through the failure of the weak spot. However, the volume fraction and damage parameters of the weak spot needed to be estimated through reverse engineering of the S-N curve. Furthermore, the predicted S-N curves were not in a good agreement when the load angle varied with respect to the flow direction because the model did not consider anisotropic fatigue damage.

In this study, we propose a new model called 'the progressive pseudograin damage accumulation (PPDA)' model which is capable of predicting the fatigue life of short fiber-reinforced plastics. Unlike other models, our model does not compute the fatigue life by orientation averaging of the whole composites, but rather describes sequential fatigue failure of pseudograins. In our proposed model, we take into account the viscoelastic-viscoplastic behavior of SFRPs. Anisotropic fatigue damage of pseudograin is also considered using a so called "normalized fatigue factor". Then, we propose a progressive damage accumulation method that can predict the overall failure of SFRPs considering the stress concentration and fatigue damage of pseudograins. Finally, PPDA model is implemented into ABAQUS user material subroutine (UMAT). Fatigue lifetime predicted by UMAT was in a good agreement with experimental data. The graphical description of the overall procedure of our model is provided in **Figure 3-1**.

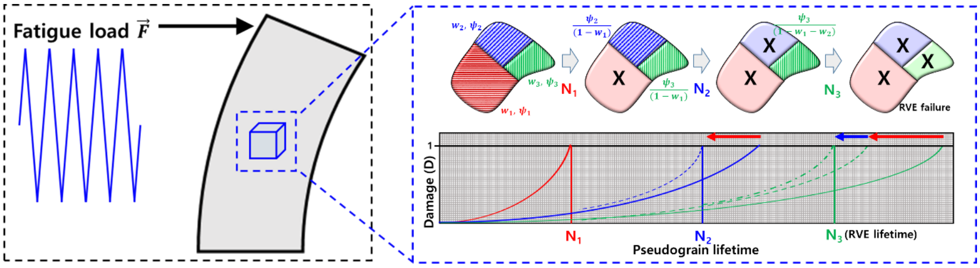

Figure 3-1. The graphical description of progressive pseudograin damage accumulation (PPDA) for fatigue.

3.2. Constitutive modeling

To predict the effective response of the real RVE is assumed to be equivalent to that of a numerical RVE, which is modeled as an aggregate consisting of discrete pseudograins. Each pseudograin is unidirectional composites, where elastic fibers with the same orientation are embedded in the VEVP matrix phase. While the pseudograins are aligned within each other, they are misaligned within the numerical RVE. This approach leads to a two-step homogenization, proposed by Doghri et al. [114]. In the first step, a mean-field homogenization is used to distribute the fatigue load inside each pseudograin. In the second homogenization step, a uniform strain is partitioned to pseudograins, resulting in the overall mechanical response.

In our PPDA model, the two-step procedure is generalized in order to treat progressive fatigue damage and failure. Section 3.2 describes the procedure of developing the PPDA model under the assumption that each pseudograin is a unidirectional continuous fiber-reinforced plastic. The matrix behavior model and two-step homogenization procedure are described in Section 3.2.1 and 3.2.2, respectively. The fatigue life prediction of each pseudograin and RVE are described in Sections 3.2.3 and 3.2.4, respectively.

3.2.1. Viscoelastic (VE)-viscoplastic (VP) matrix model

In this study, the behavior of matrix in pseudograin is described by viscoelastic-viscoplastic (VEVP) constitutive equation. Researchers have proposed VEVP constitutive models for the thermoplastic polymer [20, 21]. In this section, VEVP constitutive models used in this study are briefly introduced.

The increment of total strain is additively decomposed into two parts: a viscoelastic strain increment $d\boldsymbol{\varepsilon}^{ve}$ and a viscoplastic strain increment $d\boldsymbol{\varepsilon}^{vp}$.

$$d\boldsymbol{\varepsilon} = d\boldsymbol{\varepsilon}^{ve} + d\boldsymbol{\varepsilon}^{vp} \tag{7}$$

3.2.1.1. Linear viscoelastic model

The linear viscoelastic stress is computed in integral form by applying the Boltzmann superposition principle [22, 23].

$$\boldsymbol{\sigma}(t) = \int_{-\infty}^{t} \mathbf{C}^{ve}(t-\tau) : \frac{\partial \boldsymbol{\varepsilon}^{ve}}{\partial \tau} d\tau \tag{8}$$

For an isotropic material, relaxation tensor $\mathbf{C}^{ve}(t)$ and long term relaxation tensor $\mathbf{C}_{\infty}^{ve}$ are written as:

$$\mathbf{C}^{ve}(t) = 2G(t)\mathbf{I}^{dev} + 3K(t)\mathbf{I}^{vol} \tag{9}$$

$$\mathbf{C}_{\infty}^{ve} = 2G_{\infty}\mathbf{I}^{dev} + 3K_{\infty}\mathbf{I}^{vol} \tag{10}$$

where $\mathbf{I}^{vol}$ and $\mathbf{I}^{dev}$ are the spherical and deviatoric operators respectively. They can be expressed as: $\mathbf{I}^{vol} \equiv \frac{1}{3}\mathbf{1}\otimes\mathbf{1}$ and $\mathbf{I}^{dev} \equiv \mathbf{I} - \mathbf{I}^{vol}$, where $\mathbf{1}$ and $\mathbf{I}$ are the second and the fourth order symmetric identity tensors respectively. $G(t)$ and

$K(t)$ are the shear and bulk stiffness of the Maxwell elements and can be expressed as Prony series:

$$\begin{cases} G(t) = G_{\infty} + \sum_{j=1}^{N} G_j \exp(-\frac{t}{g_j}) \\ K(t) = K_{\infty} + \sum_{j=1}^{N} K_j \exp(-\frac{t}{k_j}) \end{cases} \tag{11}$$

G_{∞} and K_{∞} represent the long term relaxation moduli. N is the number of Maxwell elements. G_j and K_j are the relaxation weights, and g_j and k_j are the relaxation times.

3.2.1.2. Viscoplastic model

The Perzyna viscoplastic flow rule is adopted to characterize viscoplastic behavior.

$$\dot{\boldsymbol{\varepsilon}}^{vp} = \dot{\gamma}\mathbf{N} = \dot{\gamma}\frac{\partial f}{\partial \boldsymbol{\sigma}}, \quad \dot{\gamma} = \frac{\sigma_{y0}}{\mu}\left\langle \left(\frac{f}{\sigma_{y0}} \right)^{m} \right\rangle \tag{12}$$

Where $\frac{\partial f}{\partial \boldsymbol{\sigma}}$ indicates the direction of viscoplastic strain vector perpendicular to the yield surface in the flow rule. $\dot{\gamma}$ is the viscoplastic multiplier indicating the magnitude of the strain vector. μ and m are viscosity coefficient and exponent respectively. In the above equation, "$\langle \bullet \rangle$" are MacCauley brackets used to describe

$\langle \bullet \rangle = 0$ when $\bullet < 0$, and $\langle \bullet \rangle = \bullet$ when $\bullet \geq 0$. Yield function adopted in this study is defined as follows:

$$f = \bar{\sigma} - \sigma_{y0} - \kappa(\bar{\varepsilon}^{vp}) \tag{13}$$

$$\kappa(\bar{\varepsilon}^{vp}) = A(\bar{\varepsilon}^{vp})^{B} \tag{14}$$

Where σ_{y0} is initial yield strength and $\kappa(\bar{\varepsilon}^{vp})$ is isotropic hardening stress function. In this model, equivalent stress $\bar{\sigma}$ is calculated using classical J2 theory (von Mises stress). A and B are hardening coefficient and exponent, respectively.

3.2.1.3. Computational algorithm of VEVP constitutive equation

Variables $(\boldsymbol{\sigma}_n, \boldsymbol{\varepsilon}_n, \boldsymbol{\varepsilon}_n^{vp}, \gamma_n)$ at t_n are assumed to be known. Variables at t_{n+1} are calculated using a strain increment $\Delta\boldsymbol{\varepsilon}$ as described as follows.

A return mapping algorithm was used to calculate the stress with VE predictor followed by VP corrector. The unknown stress at time t_{n+1} is expressed as follows:

$$\boldsymbol{\sigma}(t_{n+1}) = \boldsymbol{\sigma}^{trial}(t_{n+1}) - \mathbf{C}^{ve} : \Delta\boldsymbol{\varepsilon}^{vp} \tag{15}$$

Trial stress $\boldsymbol{\sigma}^{trial}(t_{n+1})$ is calculated with VE predictor as follows:

$$\boldsymbol{\sigma}^{trial}(t_{n+1}) = \mathbf{C}_{\infty}^{ve} : \boldsymbol{\varepsilon}^{ve}(t_n) + \mathbf{C}^{ve} : \Delta\boldsymbol{\varepsilon} + \sum_{j=1}^{n} \exp(-\frac{\Delta t}{\tau_j})\mathbf{h}_j(t_n) \tag{16}$$

where $\mathbf{h}_j$ is internal stress variable which is updated at every time increment as:

$$\sum_{j=1}^{n} \mathbf{h}_j(t_{n+1}) = \sum_{j=1}^{n} \exp(-\frac{\Delta t}{\tau_j})\mathbf{h}_j(t_n) + \mathbf{C}^{ve}\Delta\boldsymbol{\varepsilon}^{ve} - \mathbf{C}_{\infty}^{ve}\Delta\boldsymbol{\varepsilon}^{ve} \tag{17}$$

where

$$\mathbf{C}^{ve} = 2G(\Delta t)\mathbf{I}^{dev} + 3K(\Delta t)\mathbf{I}^{vol} \tag{18}$$

$$\begin{cases} G(\Delta t) = G_{\infty} + \sum_{j=1}^{n} G_j \dfrac{1-\exp(-\Delta t / g_j)}{\Delta t / g_j} \\ K(\Delta t) = K_{\infty} + \sum_{j=1}^{n} K_j \dfrac{1-\exp(-\Delta t / k_j)}{\Delta t / k_j} \end{cases} \tag{19}$$

When the trial stress satisfies $f < 0$ using **Equation (13)**, the matrix behavior is considered viscoelastic and the total stress at t_n is:

$$\boldsymbol{\sigma}(t_n) = \mathbf{C}_{\infty}^{ve} : \boldsymbol{\varepsilon}^{ve}(t_n) + \sum_{j=1}^{n} \mathbf{h}_j(t_n) \tag{20}$$

Combining **Equation (16)** and **(20)**, the stress increment can be expressed as:

$$\Delta\boldsymbol{\sigma} = \mathbf{C}^{ve} : (\Delta\boldsymbol{\varepsilon} - \Delta\boldsymbol{\varepsilon}_{ve}^{af}) \tag{21}$$

where $\Delta\boldsymbol{\varepsilon}_{ve}^{af}$ is the following inelastic term of VE part:

$$\Delta\boldsymbol{\varepsilon}_{ve}^{af}=\left(\mathbf{C}^{ve}\right)^{-1}:\sum_{j=1}^{n}\left[1-\exp(-\frac{\Delta t}{\tau_j})\right]\mathbf{h}_j(t_n) \tag{22}$$

When the trial stress satisfies $f \geq 0$, the VP corrector operates using flow rule and yield function in **Equation (12)** and **(13)**. VP corrector find the solution using Newton-Rapson iteration that satisfy following **Equation (23)** and **(24)**:

$$\chi = f-\sigma_{y0}\left(\frac{\mu\Delta\gamma}{\Delta t\sigma_{y0}}\right)^{1/m}\leq 0 \tag{23}$$

$$\boldsymbol{\varepsilon}_{n+1}^{vp}=\boldsymbol{\varepsilon}_{n}^{vp}+\Delta\gamma\mathbf{N}_n \tag{24}$$

Equation (23) is dynamic yield function including VP flow rule [115]. When trial stress satisfies $\chi \leq 0$ during iteration, the stress increment can be expressed as:

$$\Delta\boldsymbol{\sigma}=\mathbf{C}^{ve}:(\Delta\boldsymbol{\varepsilon}-\Delta\boldsymbol{\varepsilon}^{vp}-\Delta\boldsymbol{\varepsilon}_{ve}^{af}-\Delta\boldsymbol{\varepsilon}_{vp}^{af}) \tag{25}$$

where $\Delta\boldsymbol{\varepsilon}_{vp}^{af}$ is the following inelastic term of VP part. $\Delta\boldsymbol{\varepsilon}_{vp}^{af}$ is expressed as:

$$\Delta\boldsymbol{\varepsilon}_{ve}^{af}+\Delta\boldsymbol{\varepsilon}_{vp}^{af}=\Delta\boldsymbol{\varepsilon}-\left(\mathbf{C}^{vp}\right)^{-1}:\Delta\boldsymbol{\sigma} \tag{26}$$

where $\mathbf{C}^{vp}$ is algorithmic tangent operator followed by general isotropization [116]. Using **Equation (26)**, inelastic term for mean-field homogenization of VEVP pseudograin is calculated as follows:

$$\Delta\boldsymbol{\tau} = -\left(\mathbf{C}^{vp}\right)^{-1} : (\Delta\boldsymbol{\varepsilon}_{ve}^{af} + \Delta\boldsymbol{\varepsilon}_{vp}^{af}) \tag{27}$$

3.2.2. Mean-field homogenization of a pseudograin

In order to calculate the behavior of every pseudograin, the homogenization of elastic fiber and VEVP matrix is required. Mean-field homogenization method based on the Mori-Tanaka model is used [12]. The macro-strain field is expressed as $\langle\boldsymbol{\varepsilon}\rangle_{\Omega}$, where $\langle\bullet\rangle_{\Omega}$ designates volume averaging operator quantity. The average micro-strain field in each phase can be correlated using the strain concentration tensor (between matrix and fiber) $\mathbf{A}^{\varepsilon}$ as follows.

$$\langle\boldsymbol{\varepsilon}\rangle_{\Omega_f} = \mathbf{A}^{\varepsilon} : \langle\boldsymbol{\varepsilon}\rangle_{\Omega_m} \tag{28}$$

Mori-Tanaka model assumes that all fibers in composites are aligned and identical. The strain concentration tensor $\mathbf{A}^{\varepsilon}$ provided by the Mori–Tanaka model is as follows:

$$\mathbf{A}^{\varepsilon} = \left[\mathbf{I} + \mathbf{S} : (\mathbf{C}_m^{-1} : \mathbf{C}_f - \mathbf{I})\right]^{-1} \tag{29}$$

where S is Eshelby's tensor of ellipsoidal inclusion. The details of the Eshelby's tensor component are given in Mura's study [117]. Average macro-strain field can be correlated using the strain concentration tensor (between phase and macro-strain) $\mathbf{B}^{\varepsilon}$ are as follows:

$$\mathbf{B}_m^{\varepsilon} = \left[v_m \mathbf{I} + v_f \mathbf{A}^{\varepsilon} \right]^{-1}, \ \ \mathbf{B}_f^{\varepsilon} = \mathbf{A}^{\varepsilon} \left[v_m \mathbf{I} + v_f \mathbf{A}^{\varepsilon} \right]^{-1} \tag{30}$$

where v_m and v_f are the volume fraction of matrix phase and fiber phase, respectively. Strain increment field of macroscopic composites, fiber and matrix phases are proposed by Doghri et al. [118] as follows:

$$\left\langle \Delta\boldsymbol{\varepsilon} \right\rangle_{\Omega} = v_m \left\langle \Delta\boldsymbol{\varepsilon} \right\rangle_{\Omega_m} + v_f \left\langle \Delta\boldsymbol{\varepsilon} \right\rangle_{\Omega_f} \tag{31}$$

$$\left\langle \Delta\boldsymbol{\varepsilon} \right\rangle_{\Omega_f} = \mathbf{B}_f : \left\langle \Delta\boldsymbol{\varepsilon} \right\rangle_{\Omega} + (\mathbf{I} - \mathbf{B}_f) : (\mathbf{C}_m - \mathbf{C}_f)^{-1} : \left\langle \Delta\boldsymbol{\tau} \right\rangle_{\Omega_m} \tag{32}$$

$$\left\langle \Delta\boldsymbol{\varepsilon} \right\rangle_{\Omega_m} = \mathbf{B}_m : \left\langle \Delta\boldsymbol{\varepsilon} \right\rangle_{\Omega} - \frac{v_f}{v_m} (\mathbf{I} - \mathbf{B}_f) : (\mathbf{C}_m - \mathbf{C}_f)^{-1} : \left\langle \Delta\boldsymbol{\tau} \right\rangle_{\Omega_m} \tag{33}$$

where $\Delta\boldsymbol{\tau}$ is the increment of inelastic term defined in **Equation (27)**. Substituting **Equation (32)** and **(33)** into **Equation (31)** with respect to the stress increment field, we obtain,

$$\left\langle \Delta\boldsymbol{\sigma} \right\rangle_{\Omega} = \left\langle \mathbf{C} \right\rangle_{\Omega} : \left\langle \Delta\boldsymbol{\varepsilon} \right\rangle_{\Omega} + v_f (\mathbf{C}_f - \mathbf{C}_m) : (\mathbf{I} - \mathbf{B}_f) : (\mathbf{C}_m - \mathbf{C}_f)^{-1} : \left\langle \Delta\boldsymbol{\tau} \right\rangle_{\Omega_m} \tag{34}$$

$\left\langle \mathbf{C} \right\rangle_{\Omega}$ is the effective stiffness tensor of macroscopic composites is derived as follows:

$$\left\langle \mathbf{C} \right\rangle_{\Omega} = \left[v_m \mathbf{C}_m + v_f \mathbf{C}_f : \mathbf{A}^{\varepsilon} \right] : \mathbf{B}_m^{\varepsilon} \tag{35}$$

In order to apply mean-field homogenization to VEVP material, the incrementally affine linearization method developed by Miled et al. [13] is used in the study. The

VEVP stress increment of the matrix can be linearized with tangent stiffness $\mathbf{C}_m$ and inelastic term $\Delta\boldsymbol{\tau}$ as follows:

$$\Delta\boldsymbol{\sigma} = \mathbf{C}_m : \Delta\boldsymbol{\varepsilon} + \Delta\boldsymbol{\tau} \tag{36}$$

Hereafter, the incrementally linearized stress increment of the matrix is homogenized with elastic stress increment of the fiber by mean-field homogenization scheme.

3.2.3. Fatigue damage model of a pseudograin

When the RVE of SFRPs is loaded, pseudograins in it are subjected to multiaxial stresses. Since the multiaxial stresses varies for each pseudograin, a single master S-N curve is required that can predict the fatigue failure of all pseudograins. An effective stress representing the multiaxial state is suggested for describing a single master S-N curve. Subsequently, a fatigue damage model is introduced for the pseudograin master S-N curve.

3.2.3.1. Normalized fatigue factor

One of the most general criteria to predict the strength of the composites is Tsai-Wu failure criteria [119]. Assuming that pseudograin is transversely isotropic and that σ_{23} is negligible, it can be expressed as follows:

$$TW(\boldsymbol{\sigma}_{ij}) = [F_{11}\boldsymbol{\sigma}_{11}^2 + F_{22}(\boldsymbol{\sigma}_{22}^2 + \boldsymbol{\sigma}_{33}^2) + F_{66}(\boldsymbol{\sigma}_{12}^2 + \boldsymbol{\sigma}_{13}^2)] + [F_1\boldsymbol{\sigma}_{11} + F_2(\boldsymbol{\sigma}_{22} + \boldsymbol{\sigma}_{33})] = 1$$

$$F_1 = \frac{1}{X_t} - \frac{1}{X_c}\ ,\quad F_2 = \frac{1}{Y_t} - \frac{1}{Y_c}\ ,\quad F_{11} = \frac{1}{X_t X_c}\ ,\quad F_{11} = \frac{1}{X_t X_c}\ ,\quad F_{22} = \frac{1}{Y_t Y_c}\ ,\quad F_{66} = \frac{1}{S^2} \tag{37}$$

The left-hand side of **Equation (37)** represents a distance from origin to the failure envelope [120]. In this study, non-dimensional Tsai-Wu effective stress is defined as the distance from origin to the failure envelope, representing the ratio of the magnitude of the current stress state to the static failure of the composites. With this definition, non-dimensional Tsai-Wu effective stress is expressed as follows:

$$\xi = \frac{2[F_{11}\sigma_{11}^2 + F_{22}(\sigma_{22}^2 + \sigma_{33}^2) + F_{66}(\sigma_{12}^2 + \sigma_{13}^2)]}{-[F_1\sigma_{11} + F_2(\sigma_{22} + \sigma_{33})] + \sqrt{[F_1\sigma_{11} + F_2(\sigma_{22} + \sigma_{33})]^2 + 4[F_{11}\sigma_{11}^2 + F_{22}(\sigma_{22}^2 + \sigma_{33}^2) + F_{66}(\sigma_{12}^2 + \sigma_{13}^2)]}} \tag{38}$$

where X_t and X_c are tensile and compressive strength through the longitudinal direction to aligned short fiber. Y_t and Y_c are tensile and compressive strength through the transverse direction to aligned short fiber and S is shear strength of pseudograin. The schematic illustration of non-dimensional Tsai-Wu effective stress is shown in **Figure 3-2**.

On the other hand, Kawai et al. [120] proposed "modified fatigue stress ratio" using Tsai-Hill effective stress (η) and stress ratio (R) for unidirectional continuous fiber-reinforced plastics.

$$\Phi = \frac{1/2(1-R)\eta}{1-1/2(1+R)\eta} \tag{39}$$

In our study, η in **Equation (38)** is used instead of η in **Equation (12)**. In addition, **Equation (12)** is further modified. Jang et al [121] modified this equation for SFRPs by introducing the additional term. Using fitting parameter λ_1, a new equation for master S-N curve was suggested in terms of 'normalized fatigue factor (NFF)' and validated by demonstrating that S-N curves of various FRPs can be collapsed into a single master S-N curve using NFF in the followings.

$$\psi = \frac{1/2(1-R)\xi}{1-1/2(1+R)\xi} + \lambda_1 R(1-R)\xi \quad \left(-1 \le R \le 1\right) \tag{40}$$

3.2.3.2. Chaboche fatigue damage model

After converting the multiaxial stress state of pseudograin to a universal scalar quantity (NFF), a fatigue damage model is required to predict the lifetime of pseudograins. In this study, Chaboche model was used for this purpose.

Chaboche et al. suggested a non-linear continuous fatigue damage model for stress-controlled condition [122, 123]. This model describes the progressive degradation of material for the crack initiation process.

$$\frac{dD}{dN} = [1-(1-D)^{\beta+1}]^{\alpha} \left(\frac{S_{\max} - S_m}{M(1-D)} \right)^{\beta} \tag{41}$$

where D is the fatigue damage variable, $S_{\max}$ is the maximum stress, and S_m is the mean stress, β is constant. α and M are stress dependent functions and are expressed by,

$$\alpha = 1 - a \left\langle \frac{S_{\max} - S_m - S_{10}(1 - bS_m)}{S_u - S_{\max}} \right\rangle \tag{42}$$

$$M = M_0(1 - bS_m) \tag{43}$$

where S_{10} is the fatigue limit, S_u is the ultimate tensile strength. a is non-linearity parameter, b is mean stress effect parameter, and M_0 is a constant.

To apply NFF to Chaboche fatigue damage model, **Equation (40)** were combined with **(41)**, **(42)**, and **(43)**. Since NFF is defined considering stress ratio, the mean stress effect can be neglected. Therefore, mean stress effect parameter b was set to be zero and final fatigue damage equations for pseudograins are as follows:

$$\frac{dD}{dN} = [1-(1-D)^{\beta+1}]^{\alpha} \left(\frac{\psi_{\max}}{M_0(1-D)} \right)^{\beta} \tag{44}$$

$$\alpha = 1 - a \left\langle \frac{\psi_{\max} - \psi_{10}}{\psi_u - \psi_{\max}} \right\rangle \tag{45}$$

$$M = M_0 \tag{46}$$

Integrating damage from 0 to 1 in **Equation (44)**, fatigue lifetime (N_f) can be expressed as:

$$N_f = \frac{1}{(\beta+1)(1-\alpha)}\left(\frac{\psi_{\max}}{M_0}\right)^{-\beta} \tag{47}$$

Furthermore, damage at fatigue cycle N can be obtained by integrating cycle $N = 0$ to N_f as follows.

$$D = 1 - \left(1 - \left(\frac{N}{N_f}\right)^{\frac{1}{1-\alpha}}\right)^{\frac{1}{\beta+1}} \tag{48}$$

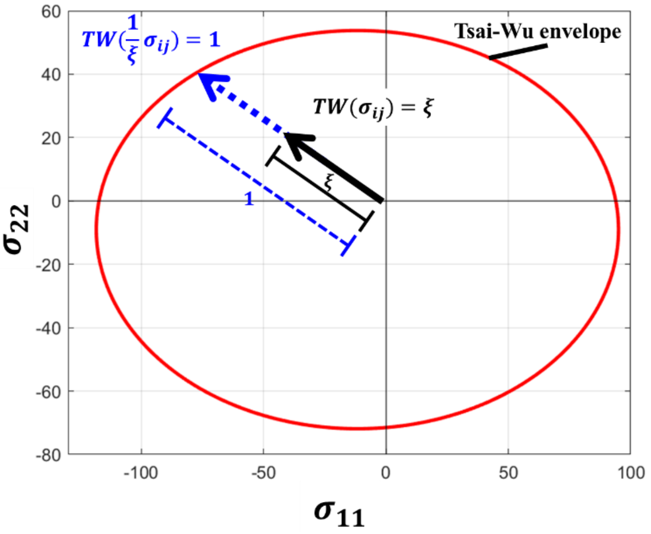

Figure 3-2 Schematic illustration of non-dimensional Tsai-Wu effective stress.

3.2.4. Developement of new damage accumulation model

After the fatigue lifetime of each pseudograin is obtained using the procedure in Section 3.2.3, the overall failure of RVE is predicted by PPDA model. We propose a new and novel PPDA model that is inspired by the progressive-ply-failure concept of laminate composites [124]. Once a pseudograin fails, the damage accumulation of the other pseudograins is accelerated due to the stress concentration.

We assume that the RVE in the fatigue loading is composed of k pseudograins: PG_i (i=1, 2, …, k). The NNF of pseudograins is calculated to ψ_i (i=1, 2, …, k) by **Equation (40)**. The fatigue life of pseudograins is expressed by $N_{f.i}$ (i=1, 2, …, k) using **Equation (47)**. Here, assume that PG_1 is a pseudograin with the shortest lifetime and PG_k is the pseudograin with the longest lifetime. Once PG_1 has failed first, all pseudgrains are cycled through $N_{f.1}$ cycles. At this cycle ($N_{f.1}$), the stress of the other pseudograins (PG_i) is concentrated due to following two reasons: (a) accumulated damage in the PG_i until the cycle $N_{f.1}$ (which can be calculated by Chaboche fatigue damage model) and (b) loss of the load-bearing ability of PG_1. First, accumulated damage of the other pseudograins is calculated using **Equation (49)** as follows:

$$D_{i.1} = 1 - \left(1 - \left(\frac{N_{f.1}}{N_{f.i}}\right)^{\frac{1}{1-\alpha}}\right)^{\frac{1}{\beta+1}} \tag{49}$$

where $D_{i.1}$ is accumulated damage in PG_i at $N_{f.1}$ cycles. In terms of mechanical parameters, damage $D_{i.1}$ can be expressed by means of a net area reduction [125]. As the damage represents the loss of effective area taking into account local stress concentrations, one can write:

$$\psi_{i.D} = \frac{\psi_i}{(1 - D_{i.1})} \tag{50}$$

where $\psi_{i.D}$ is damaged NFF. Then, the failure of PG_1 is modeled assuming that it is still capable of transferring the load to the other pseudograins and thus stress concentration effect is reflected in the NFF as follows:

$$\psi_{i.1} = K\psi_{i.D} \tag{51}$$

where $\psi_{i.1}$ is concentrated NFF at $N_{f.1}$, and K is stress concentration factor due to the failure of PG_1.

Stress concentration factor K is obtained by considering the NFF of RVE based on the assumption used in the second step of homogenization procedure. In this study, Voigt model [56], which assumes an iso-strain condition, was adopted for the second step homogenization. Accordingly, the NFF of RVE can be computed as the sum of the product of NFF and the fraction of each pseudograin, as follows:

$$\psi_{RVE} = \sum_{i=1}^{k} w_i \psi_i \tag{52}$$

where ψ_{RVE} is NFF of RVE before PG_1 fails. After PG_1 fails, NFF of RVE (ψ'_{RVE}) can be expressed as follows:

$$\psi'_{RVE} = K \sum_{i=2}^{k} w_i \psi_i \tag{53}$$

It is assumed that NFF of RVE is unchanged before and after failure ($\psi_{RVE} = \psi'_{RVE}$). Then, the stress concentration factor can be derived as follows:

$$K = \frac{\sum_{i=1}^{k} w_i \psi_i}{\sum_{i=2}^{k} w_i \psi_i} \tag{54}$$

The concentrated NFF of other pseudograins after the first pseudograin failure can be calculated using **Equations (50)**, **(51)** and **(54)** as follows:

$$\psi_{i.1} = K \psi_{i.D} = \frac{\sum_{i=1}^{k} w_i \psi_i}{\sum_{i=2}^{k} w_i \psi_i} \frac{\psi_i}{(1 - D_{i.1})} \tag{55}$$

Then, using **Equation (47)**, **(48)** and **(55)**, the remaining life of PG_2 ($n_{f.2}$) can be obtained as follows:

$$n_{f.2} = \frac{1}{(\beta + 1)(1 - \alpha)} \left(\frac{\psi_{i.1}}{M_0} \right)^{-\beta} \left[1 - (1 - (1 - D_{i.1})^{\beta + 1})^{1 - \alpha} \right] \tag{56}$$

The same procedure is then repeated after the failure of PG_2, PG_3 $\cdots$ PG_k. Finally, the life of the RVE is obtained by,

$$N_{f.RVE} = N_{f.1} + n_{f.2} + \cdots + n_{f.k} = N_{f.1} + \sum_{i=2}^{k} n_{f.i} \tag{57}$$

Flow chart for prediction of S-N curve and CLD was shown in Figure 3-3.

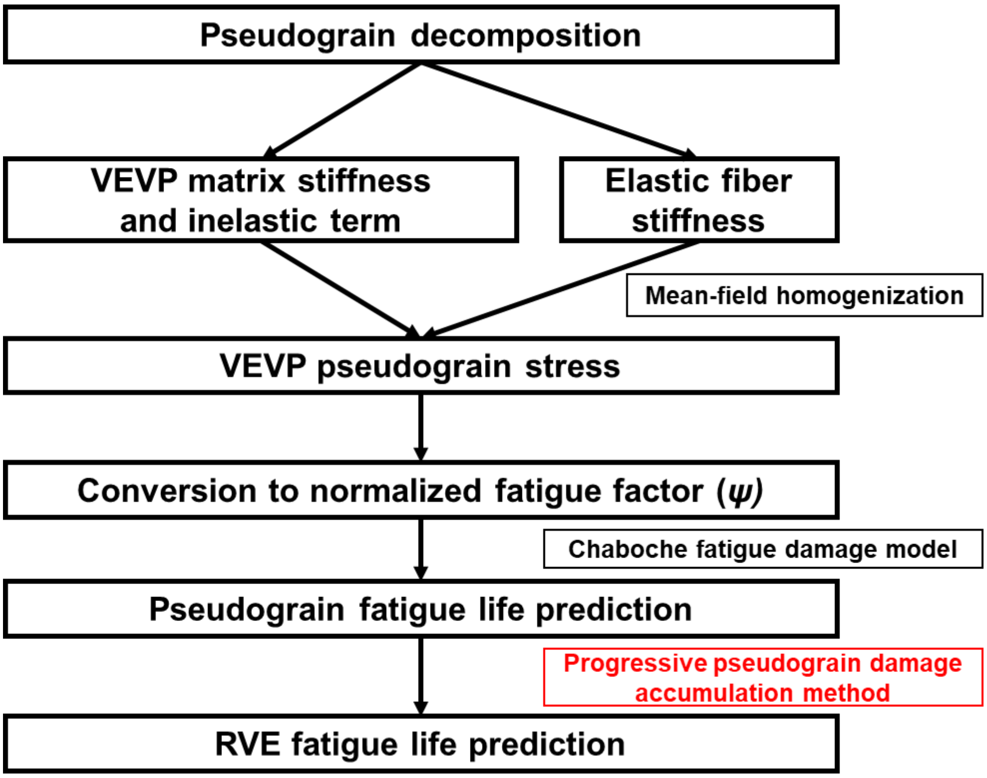

Figure 3-3 Flow chart of PPDA model.

3.3. Experimental

3.3.1. Materials

SFRP specimens were made of short glass fiber-reinforced polypropylene. The glass fibers with 30% weight fraction was embedded in polypropylene (or 13.09% volume fraction). The injection-molded sheets with a thickness of 2.7 mm were prepared and hereafter denoted by PP-GF30.

The orientation tensor of short glass fiber-reinforced plastics has been obtained by many researchers using injection molding simulation tools such as Moldex3D and Moldflow [126-132]. These researchers adopted Folgar-Tucker equation and iARD-RPR model to describe changes in the fiber orientation tensor during the injection process. The values for the parallel and transverse direction components of the fiber orientation were reported to be 0.603 to 0.785 and 0.196 to 0.377, respectively. Jiang et al [132] proposed a three-dimensional numerical model for accurately predicting the fiber orientation in injection molded parts and compared the simulated results with experiments. The material used in this study was short glass fiber-reinforced polypropylene with a plate thickness of 3 mm, and a fiber weight fraction of 20%. Due to the similarity of plate thickness and weight fraction with our study, we adopted the fiber orientation tensor a_{ij} used by Jiang et al as follows:

$$a_{ij} = \begin{bmatrix} 0.741 & 0.000 & 0.000 \\ 0.000 & 0.242 & 0.000 \\ 0.000 & 0.000 & 0.017 \end{bmatrix} \tag{58}$$

3.3.2. Mechanical testing of polypropylene

The VEVP properties of the polypropylene matrix were characterized. The viscoelastic parameters were identified by dynamic mechanical analysis (DMA) test. DMA test machine (Q800, TA instrument, USA) was used in three-point bending mode. The length and width of specimen were 60 and 10 mm, respectively. Testing temperature were ranged from −50 to 140°C with 10°C increments. The frequency were ranged from 0.01 to 10 Hz. The viscoplastic parameters were obtained by tensile tests. Tensile tests were conducted at room temperature (25°C) using a tensile testing machine (Instron 8801; Instron, Norwood, MA, USA) according to the ISO 527-2 standard [133]. Two test speeds (1.15 and 5 mm/min) were used. A digital image correlation (DIC) system (Vic-3D v7; Correlated Solutions, Inc., Irmo, SC, USA) was used to measure the tensile strain of the specimens. The dog bone-shaped specimens was used. The total length and gauge width of each specimen were 180 and 10 mm, respectively. The results of DMA test and tensile test results of PP matrix are presented in Supplementary material.

3.3.3. Fatigue testing of SFRPs

Load-controlled fatigue tests were conducted using an Instron 8801 (Instron 8801; Instron, Norwood, MA, USA). The frequency was set to 5 Hz. The fatigue test was conducted with a stress ratio of 0.1 and -1 at room temperature (25°C). Dog-boned specimens were obtained from the injection molded plate. The specimens were machined at different orientation angles by milling. Their fiber orientation angle was defined as the angle between the flow direction and the longitudinal axis of the specimen, on which the fatigue load was applied. Specimens with three orientation were used and named as PP-GF30-0D, 20D and 90D, respectively. The specifications of the test set-ups and the fatigue specimen, are shown in **Figure 3-4(a)** and **(b)**.

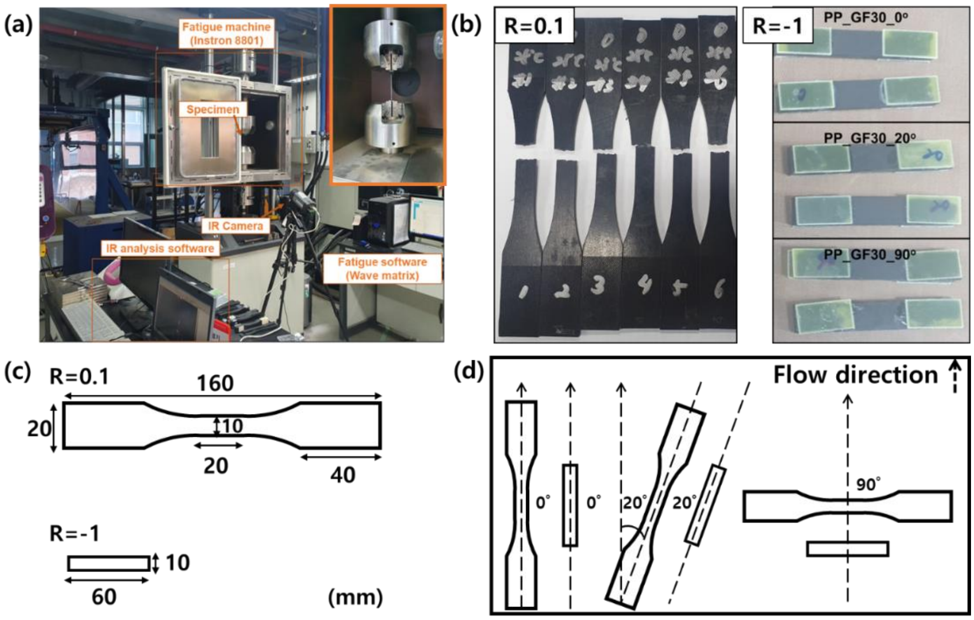

Figure 3-4 (a) Experimental set-ups and (b) test specimens for fatigue test. (c) Schematic diagram of fatigue test specimen and (d) PP-GF30-0D, 20D, 90D from PP-GF30 plate.

3.4. Results and Discussion

3.4.1. Experimental validation of VEVP homogenization model

The VEVP properties of PP matrix obtained from the DMA test and tensile tests are shown in Section 3.4.1. **Figure 3-5** and **Figure 3-6** show the DMA test and tensile test results of polypropylene, respectively. The storage modulus - reduced time curve is shown in **Figure 3-5**. Fitting the storage modulus - reduced time curve, the viscoelastic parameters were obtained for 15 Maxwell components. In the meantime, viscoplastic parameters were also obtained by curve fitting of tensile test results as shown in **Figure 3-6**. The obtained viscoelastic and viscoplastic parameters of the polypropylene were presented in **Table 3-1**.

Figure 3-7 shows the re-simulation result for validation of tensile test of PP-GF30. Elastic modulus of 72.40 GPa, Poisson's ratio of 0.22 and fiber aspect ratio of 25 were used for glass fiber in simulation. Poisson's ratio of 0.43 was used for the PP matrix in simulation. A cubic geometry of size 6×6×6 mm was created and meshed with a C3D8 element of size 1×1×1 mm as shown in **Figure 3-7(a)**. The U1=0, U2=0, and U3=0 boundary conditions were applied to the plane perpendicular to the x-, y-, and z-axis in the negative direction, respectively. A displacement boundary condition of 0.06 mm was applied to the plane perpendicular to the x-axis in the positive direction so that the applied tensile strain was 1%. The re-simulation result was compared with tensile tests of PP-GF30-0D as shown in **Figure 3-7(b)**. The simulation result was in good agreement with the experimental stress-strain curve of PP-GF30-0D. It was confirmed that the developed UMAT properly described VEVP behavior of SFRPs.

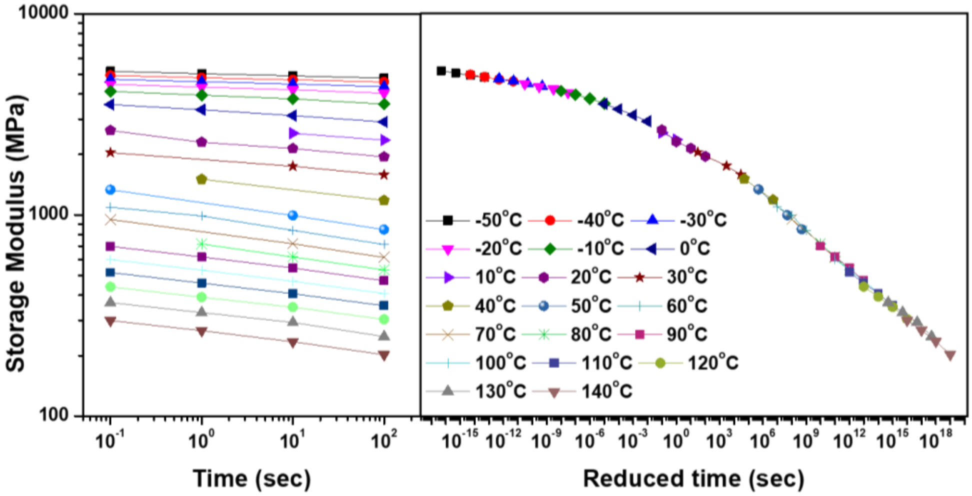

Figure 3-5 DMA test results of PP.

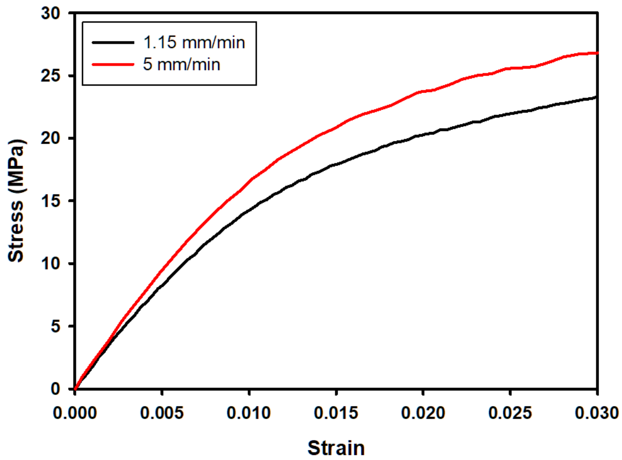

Figure 3-6 Tensile test results of PP.

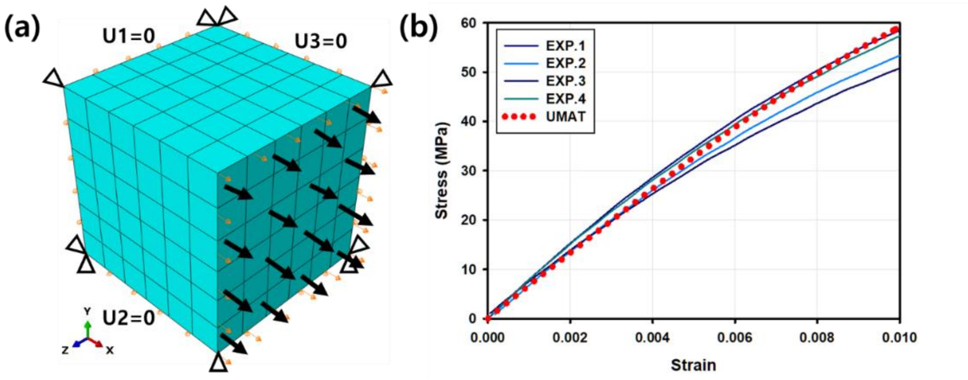

Figure 3-7 (a) Boundary condition of simulation and (b) experimental and UMAT re-simulation stress–strain curves of PP-GF30-0D.

Table 3-1 Obtained VEVP parameters of polypropylene at room temperature (25℃).

Viscoelastic parameter		
Instantaneous modulus (E_0)		4201 MPa
j	Relaxation time (τ_j)	Maxwell component moduli ratio (E_j / E_0)
1	10^6	0.0436
2	10^5	0.0475
3	10^4	0.0459
4	10^3	0.0268
5	10^2	0.0398
6	10^1	0.0525
7	10^0	0.0361
8	10^{-1}	0.0898
9	10^{-2}	0.0565
10	10^{-3}	0.0511
11	10^{-4}	0.0480
12	10^{-5}	0.0579
13	10^{-6}	0.0455
14	10^{-7}	0.0385
15	10^{-8}	0.0407
Viscoplastic parameter		
Initial yield strength (σ_{y0})		10 MPa
Viscoplasctic coefficient (μ)		5489 MPa·s
Viscoplasctic exponent (m)		1.2
Hardening coefficient (A)		88.79 MPa
Hardening exponent (B)		0.4792

3.4.2. Fatigue test results and master S-N curve construction of a pseudograin

Fatigue tests of PP-GF30-0D, 20D, and 90D samples were performed at two stress ratio (-1 and 0.1). These results were assumed to represent the fatigue behavior of pseudograin, whose the fiber direction is highly aligned. Therefore, S-N curves of PP-GF30-0D, 20D, and 90D shown in Figure 3-8 are considered to be the off-axis S-N curve of a pseudograin.

To calculate exact off-axis angle of the specimen, the orientation tensor of PP-GF30-0D obtained from Section 3.3.1 was rotated using simple rotation tensor ($\mathbf{r}_\varphi$) expressed as:

$$\mathbf{r}_\varphi = \begin{bmatrix} \cos\varphi & -\sin\varphi & 0 \\ \sin\varphi & \cos\varphi & 0 \\ 0 & 0 & 1 \end{bmatrix} \tag{59}$$

where φ is the transverse angle respect to the flow direction. Combining **Equation (58)** and **(59)**, the orientation tensors a_φ of PP-GF30-0D, 20D, and 90D are as follows:

$$a_{0^\circ} = \begin{bmatrix} 0.741 & 0.000 & 0.000 \\ & 0.242 & 0.000 \\ & & 0.017 \end{bmatrix}, a_{20^\circ} = \begin{bmatrix} 0.683 & 0.160 & 0 \\ & 0.300 & 0 \\ & & 0.017 \end{bmatrix}, a_{90^\circ} = \begin{bmatrix} 0.242 & 0.000 & 0.000 \\ & 0.741 & 0.000 \\ & & 0.017 \end{bmatrix} \tag{60}$$

Using orientation tensors in **Equation (60)** and fatigue data in **Figure 3-8**, a master S-N curve was constructed. First, the uniaxial maximum strength $S_{\max}$ from fatigue test was converted to stress tensor ($\mathbf{S}_{0^\circ}$, $\mathbf{S}_{20^\circ}$, $\mathbf{S}_{90^\circ}$) as follows:

$$\mathbf{S}_{0^\circ} = \mathbf{Q}_{0^\circ} \begin{bmatrix} S_{\max} & 0 & 0 \\ & 0 & 0 \\ & & 0 \end{bmatrix} \mathbf{Q}_{0^\circ}^{-1} = \begin{bmatrix} 0.741 & -0.427 & -0.097 \\ & 0.246 & 0.056 \\ & & 0.013 \end{bmatrix} S_{\max}$$

$$\mathbf{S}_{20^\circ} = \mathbf{Q}_{20^\circ} \begin{bmatrix} S_{\max} & 0 & 0 \\ & 0 & 0 \\ & & 0 \end{bmatrix} \mathbf{Q}_{20^\circ}^{-1} = \begin{bmatrix} 0.683 & -0.457 & -0.090 \\ & 0.306 & 0.060 \\ & & 0.012 \end{bmatrix} S_{\max} \tag{61}$$

$$\mathbf{S}_{90^\circ} = \mathbf{Q}_{90^\circ} \begin{bmatrix} S_{\max} & 0 & 0 \\ & 0 & 0 \\ & & 0 \end{bmatrix} \mathbf{Q}_{90^\circ}^{-1} = \begin{bmatrix} 0.242 & -0.427 & -0.032 \\ & 0.754 & 0.056 \\ & & 0.004 \end{bmatrix} S_{\max}$$

Note that uniaxial tensile strength $S_{\max}$ was multiplied with rotation tensor $\mathbf{Q}_\varphi$ expressed as follows:

$$\mathbf{Q}_\varphi = \begin{bmatrix} \cos\theta\cos\phi & \sin\theta\cos\phi & \sin\phi \\ -\sin\theta & \cos\theta & 0 \\ -\cos\theta\sin\phi & -\sin\theta\sin\phi & \cos\phi \end{bmatrix}, \quad \theta = \sin^{-1}\left(\sqrt{\frac{a_\varphi(2,2)}{1-a_\varphi(3,3)}}\right), \quad \phi = \sin^{-1}\left(\sqrt{a_\varphi(3,3)}\right) \tag{62}$$

where θ and ϕ are two Euler angles respect to the x-axis and xy-plane defined by Advani and Tucker [134]. Details about derivation of rotation tensor can be found in literature [135, 136]. It should be noted that fatigue specimens were treated as unidirectional composites so that a_φ represents the orientation of single fiber. Then, NFF was obtained by substituting the multiaxial stress into **Equation (38)** and **(40)**. Tsai-Wu parameters for **Equation (38)** were obtained fitting the tensile and compression test of PP-GF30-0D, 20D, and 90D as shown in **Table 3-2**. The fitting parameter ($\lambda_1 = -0.2$) was obtained that can collapse S-N curves of different stress ratio (-1 and 0.1) into a single master curve. Finally, the obtained master S–N curve is presented in **Figure 3-9**, where the symbols indicate the NFF obtained by transforming the fatigue data in **Figure 3-8**. The result shows that fatigue data were properly collapsed, confirming that the fatigue life of any pseudograin can be predicted regardless of fatigue loading condition.

To model progressive degradation of individual pseudograin, Chaboche damage fatigue model in **Equation (44)** was implemented into ABAQUS user material subroutine (UMAT). Fatigue parameters for the master curve were obtained and are listed in **Table 3-3**. Details of parameter identification methods are given in reference [137]. The value of parameter a was assumed to be 0.65, which is the value of PP-GF obtained from the same reference [137]. The master S-N curve obtained by the fatigue damage model is shown by blue solid line in **Figure 3-9**.

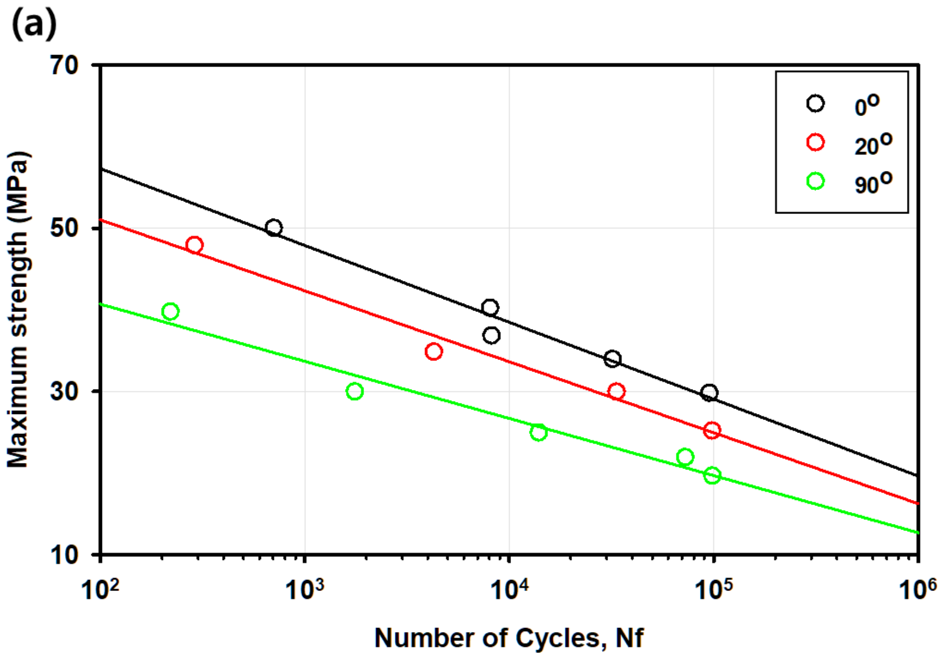

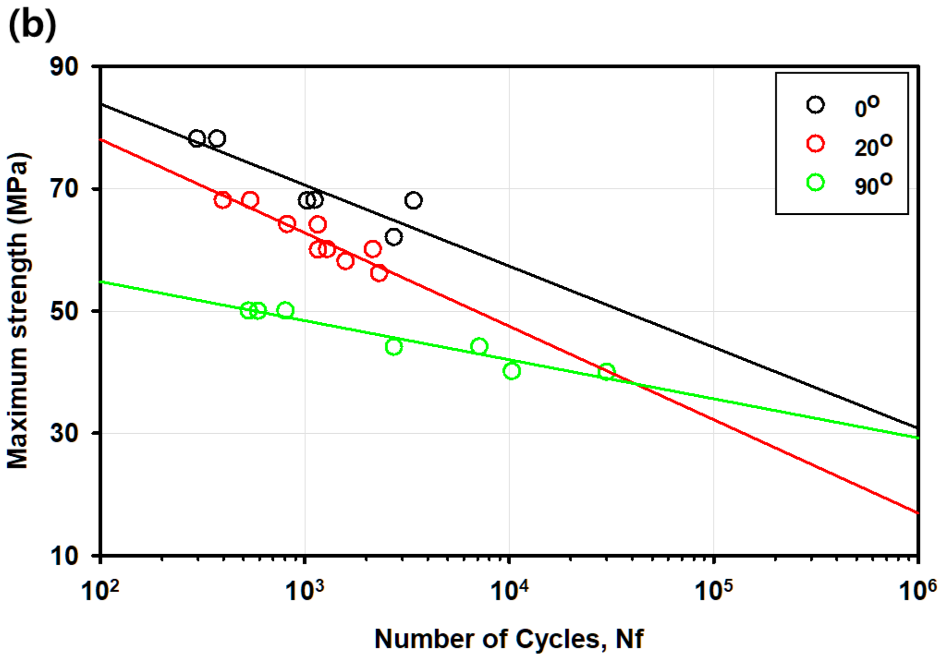

Figure 3-8 S-N curves of PP-GF30 with different fiber orientations (0D, 20D, and 90D) for stress ratio (a) -1 and (b) 0.1.

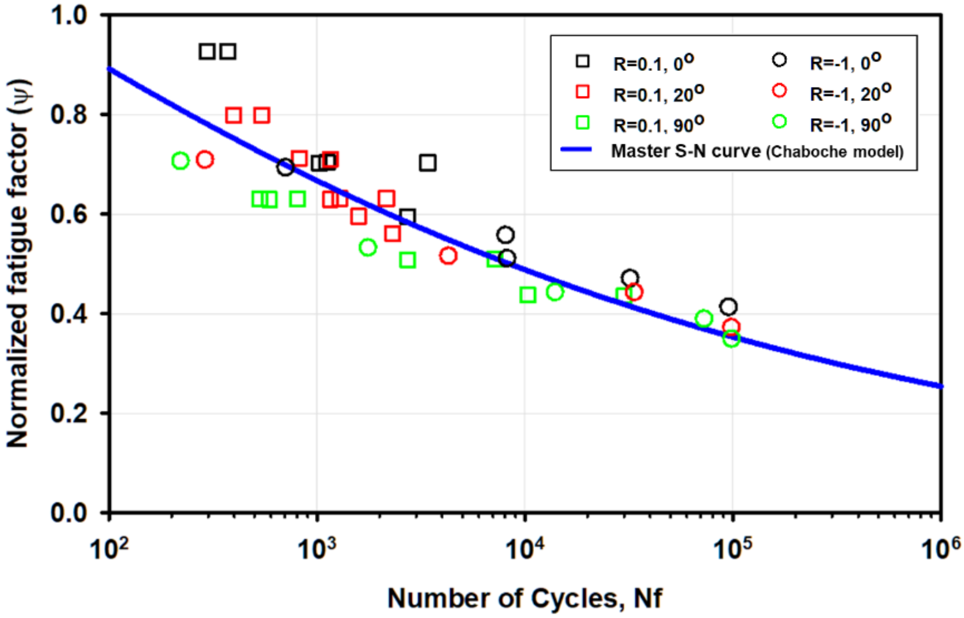

Figure 3-9 A master S-N curve of PP-GF30 using NFF.

Table 3-2 Tsai-Wu parameter for unidirectional pseudograin

Tsai-Wu parameters	
Longitudinal tensile strength (X_t)	126.72
Longitudinal compressive strength (X_c)	158.35
Transverse tensile strength (Y_t)	53.06
Transverse compressive strength (Y_c)	98.60
Shear strength (S)	43.88

Table 3-3 Chaboche fatigue damage model parameters of PP-GF30 master curve.

Chaboche fatigue damage model parameters	
Ultimate normalized fatigue factor (ψ_u)	1.4
Fatigue endurance limit (ψ_{l0})	0.01
Non-linear parameter (a)	0.65
Chaboche constant 1 (β)	5.658
Chaboche constant 2 (M_0)	2.875

3.4.3. Experimental validation of PPDA model

The reconstruction of orientation distribution function (ODF) and pseudograin decomposition procedure for 12 pseudograins were implemented in UMAT. Then, the VEVP model and mean-field homogenization method described in the previous sections were implemented. The PPDA model developed in this study were also implemented in UMAT. The re-simulation of PP-GF30 fatigue tests with three specimen (0D, 20D, 90D) and two stress ratio (-1, 0.1) were performed as follows. Elastic modulus of 72.40 GPa, Poisson's ratio of 0.22 and fiber aspect ratio of 25 were used for glass fiber in simulation. Poisson's ratio of 0.43 was used for the PP matrix in simulation. Maximum NFF $\psi_{\max}$ was obtained from the maximum value of the third cycle of the fatigue simulation.

A cubic geometry of size 6×6×6 mm was created and meshed with a C3D8 element of size 1×1×1 mm. The U1=0, U2=0, and U3=0 boundary conditions were applied to the plane perpendicular to the x-, y-, and z-axis in the negative direction, respectively. A load in a sine wave with 5 Hz frequency was applied to the plane perpendicular to the x-axis in the positive direction. Varying maximum load of sine wave and stress ratio, the fatigue tests of three different specimens (PP-GF30-0D, 20D, 90D) were simulated. Simulation conditions are detailed in **Table 3-4**.

The simulation results are presented in **Figure 3-10**, where **Figure 3-10(a)** and **Figure 3-10(b)** show the result of tension-compression ($R = -1$) and tension-tension ($R = 0.1$) conditions, respectively. Both S-N curves show a good agreement with experimental results, confirming that NFF reflects the mean stress effect of pseudograins inside SFRPs. The black, red, and green solid lines in **Figure 3-10** represent simulation results of specimens with different fiber orientation tensor (0D, 20D, 90D), showing a good agreement with the experimental results. Therefore, it can be claimed that Tsai-Wu effective stress concept and pseudograin decomposition method can properly capture the effect of fiber orientation. However, there is a slight difference between the simulation results of PP-GF30-0D and PP-GF30-20D in law fatigue cycle (~10^3) shown in **Figure 3-10(a)** and the experimental results. This is thought to be due to a master S-N curve fitting problem. As shown in **Figure 3-9**, the master S-N curve does deviate slightly from each experiment as the number of cycles decreases. This error seems to be cause of the difference between experiments and simulation. More detailed investigation into this issue will be discussed in the following Section 3.4.4 and Section 3.4.5.

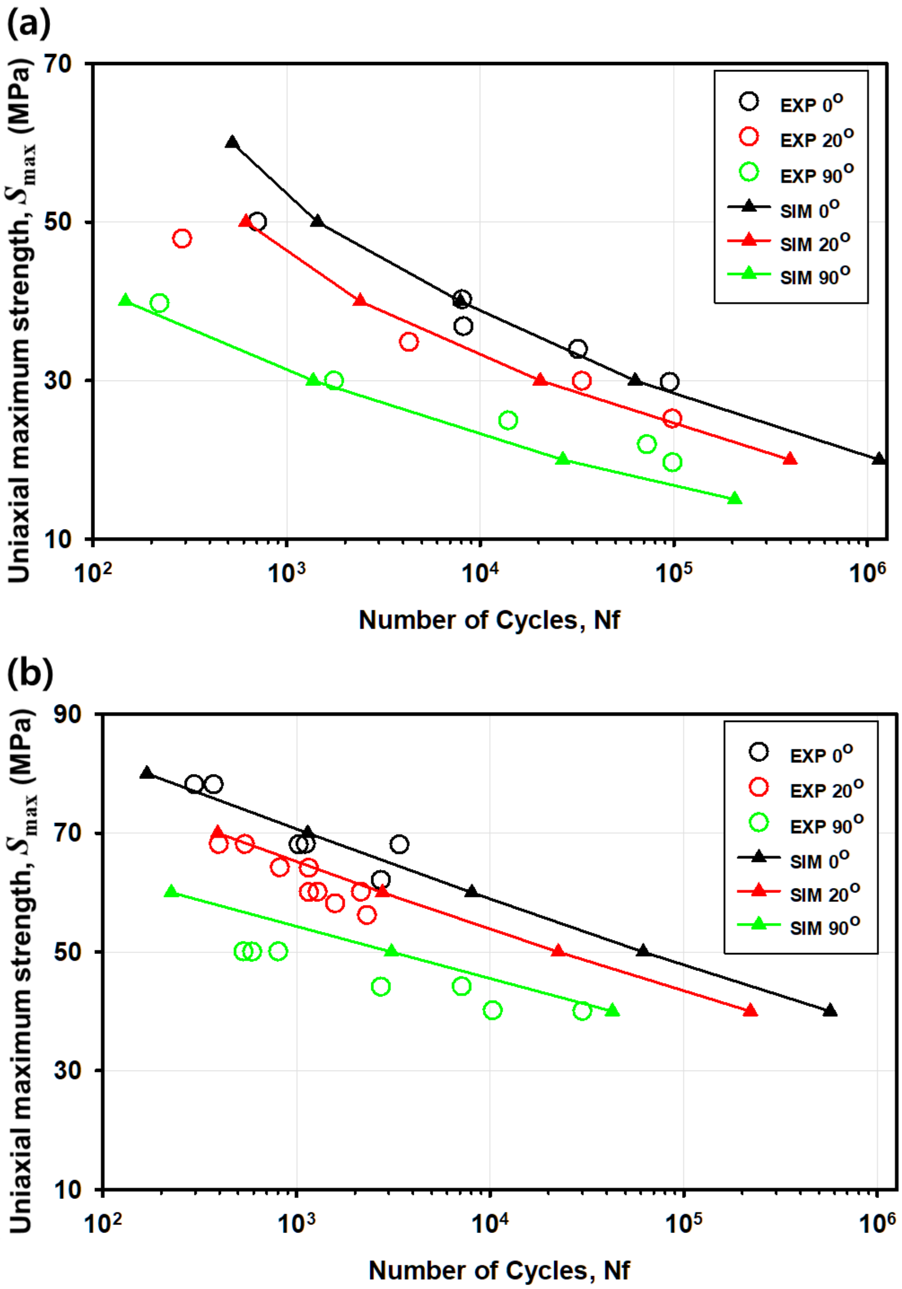

Figure 3-10 Comparison between numerical and experimental S-N curves of PP-GF30 with different fiber orientations (0D, 20D, 90D) for stress ratio (a) -1 and (b) 0.1.

Table 3-4 Boundary condition of fatigue test simulation

Stress ratio (R)	Specimen	Applied maximum stress (MPa)	Applied maximum load (N)
-1	PP-GF30-0D	20, 30, 40, 50, 60	720, 1080, 1440, 1800, 2160
-1	PP-GF30-20D	20, 30, 40, 50	720, 1080, 1440, 1800
-1	PP-GF30-90D	15, 20, 30, 40	540, 720, 1080, 1440
0.1	PP-GF30-0D	40, 50, 60, 70, 80	1440, 1800, 2160, 2520, 2880
0.1	PP-GF30-20D	40, 50, 60, 70	1440, 1800, 2160, 2520
0.1	PP-GF30-90D	40, 50, 60	1440, 1800, 2160

3.4.4. Comparison of PPDA model with Tsai-Hill fatigue indicator

The present PPDA model employs NFF concept and Chaboche fatigue damage model to describe damage and predict fatigue life of individual pseudograin. This section is to compare the present model with widely used Tsai-Hill fatigue indicator model for individual pseudograins. The Tsai-Hill fatigue indicator is expressed as follows:

$$f(N)=\frac{\boldsymbol{\sigma}_{11}^2}{X_t^2(N)}-\frac{\boldsymbol{\sigma}_{11}(\boldsymbol{\sigma}_{22}+\boldsymbol{\sigma}_{33})}{X_t^2(N)}+\frac{\boldsymbol{\sigma}_{22}^2+\boldsymbol{\sigma}_{33}^2}{Y_t^2(N)}+(\frac{1}{X_t^2(N)}-\frac{2}{Y_t^2(N)})\boldsymbol{\sigma}_{22}\boldsymbol{\sigma}_{33}+\frac{(\boldsymbol{\sigma}_{12}^2+\boldsymbol{\sigma}_{13}^2)}{S^2(N)}+(\frac{4}{Y_t^2(N)}-\frac{1}{X_t^2(N)})\boldsymbol{\sigma}_{23}^2$$

$$X_t(N)=X_t(-\frac{Sl_X}{Int_X}\log(N)+1)\ ,\quad Y_t(N)=Y_t(-\frac{Sl_Y}{Int_Y}\log(N)+1)\ ,\quad S(N)=S(-\frac{Sl_S}{Int_S}\log(N)+1) \tag{63}$$

where $f(N)$ is the failure indicator, $X_t(N)$, $Y_t(N)$ and $S(N)$ are the fatigue strength of two tensile and one shear fatigue loading, and Sl_X, Sl_Y, Sl_S, Int_X, Int_Y and Int_S are parameters of Tsai-Hill fatigue indicator. Tsai-Hill fatigue indicator finds the fatigue life of unidirectional composites finding $N = N_f$ which makes $f(N)=1$. Using the Thai-Hill fatigue indicator parameters in **Table 3-2** and experimental fatigue test results in **Figure 3-10**, Tsai-Hill fatigue indicator parameters are obtained by fitting **Equation (63)**. The result is shown in **Table 3-5**.

In this section, the fiber orientation of 12 pseudograins was set to be identical so that a single pseudograin was calculated. The re-simulation of PP-GF30 fatigue result with three specimen (0D, 20D, 90D) and two stress ratio (-1, 0.1) were carried out. Fiber orientation tensors of **Equation (60)** was used. The same geometry, mesh type, and boundary conditions as in the previous section were taken.

The simulation results are presented in **Figure 3-11(a)** and **Figure 3-11(b)** are the result of tension-compression ($R = -1$) and tension-tension ($R = 0.1$) conditions, respectively. Overall, Tsai-Hill failure indicator predicts a shorter fatigue life of PP-GF30. The slope of S-N curve predicted by Tsai-Hill failure indicator is smaller than that of the present model. When compared to experimental S-N curve, both Tsai-Hill fatigue indicator and the present model show similar levels of accuracy. Nevertheless, Tsai-Hill fatigue indicator is not appropriate for predicting damage accumulation in sequential fatigue failure of pseudograins. The key requirement in sequential fatigue failure process is to calculate the damage accumulation of each pseudograin when other pseudograins have failed and is to consider the stress concentration caused by the accumulated damage. Tsai-Hill fatigue indicator only predicts the final failure of pseudograins because it assumes that strength of composites decrease linearly as the fatigue cycle progresses. If accumulated fatigue damage in pseudograin is linear, Tsai-Hill failure indicator can be used; however, previous studies have shown that the fatigue damage accumulation profile is nonlinear [122, 137]. Consideration of asymmetric tensile and compressive strength is another advantage of the current PPDA model compared to the Tsai-Hill indicator that does not take such asymmetry into account.

Inaccuracies in the prediction in **Figure 3-11** are likely to be a consequence of assumption in parameter identification. Accumulated damage of pseudograins during successive failure is highly dependent on the fatigue damage parameter a.

Note that a is obtained from the reference [137]. More accurate fatigue life prediction is possible, if parameter a is identified by two-step fatigue test or observation of cyclic stiffness [123]. Moreover, the assumptions for the current PPDA model may lead to inaccuracies in prediction. In the present framework, micromechanical damages behavior such as matrix damage by fiber tip [107], delamination [109], and fiber-fiber interaction effect [138] during fatigue cycles were not considered. While micromechanical models considering these behavior may bring more physically reasonable and accurate results, their use may increase the computational cost due to the existence of 12 pseudograins and iterations in VEVP behavior. In this aspect, the current PPDA model offers a good compromise between accuracy and computational cost in simulation.

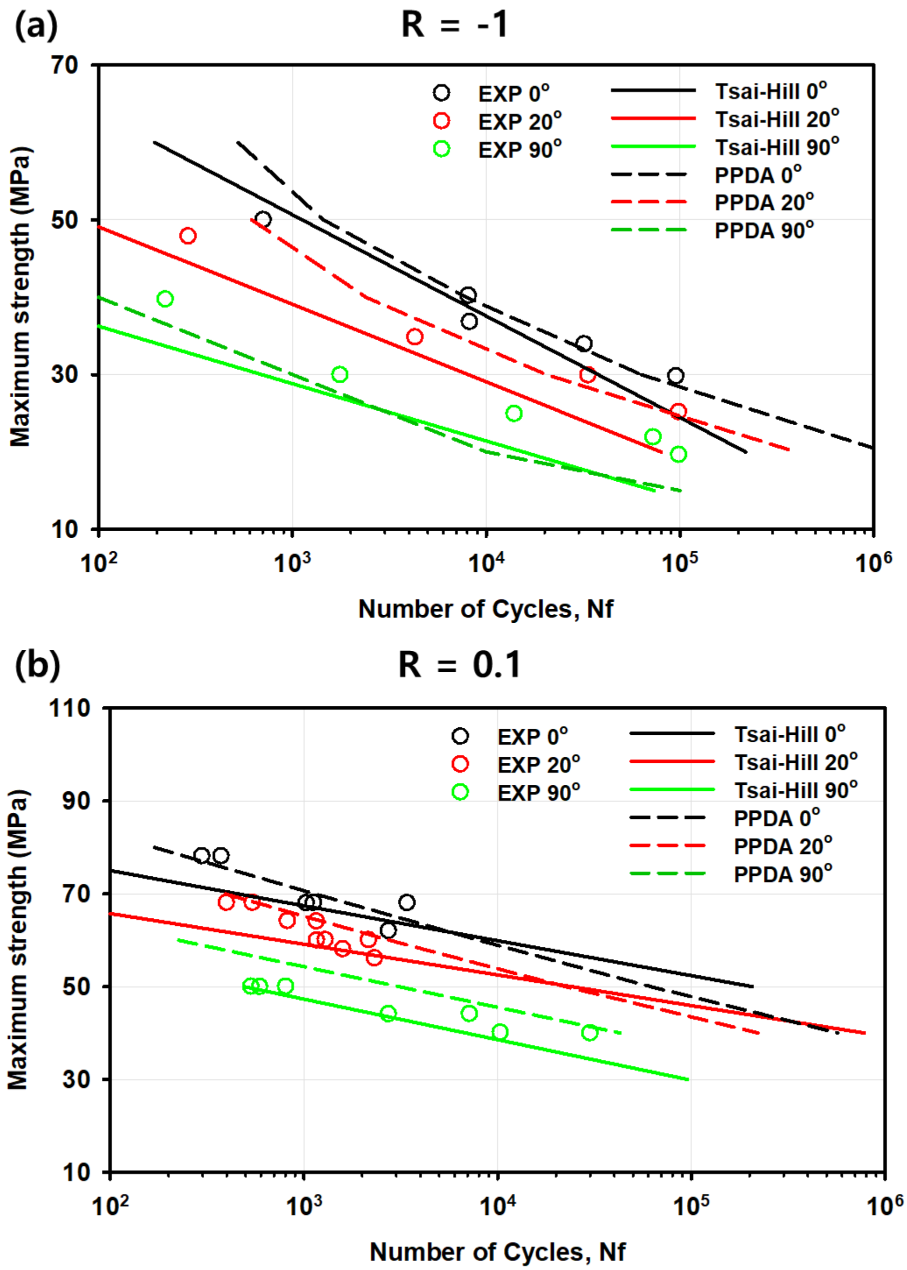

Figure 3-11 Comparison of S-N curves predicted using the present model with that using Tsai-Hill fatigue indicator for different fiber orientations (0D, 20D, 90D) and stress ratio (a) -1 and (b) 0.1.

Table 3-5 Parameters of Tsai-Hill fatigue indicator (PP-GF30)-

R = -1					
Sl_X	Int_X	Sl_Y	Int_Y	Sl_S	Int_S
-18.47	126.7	-6.608	53.06	-4.998	43.88
R = 0.1					
Sl_X	Int_X	Sl_Y	Int_Y	Sl_S	Int_S
-10.62	126.7	-2.609	53.06	-2.102	43.88

3.4.5. Further comparison of PPDA model for different fiber orientation cases

The failure of RVE can be decided using various criteria, e.g., first pseudograin failure, last pseudograin failure, and PPDA model in this study. In this section, these criteria are compared by simulating the fatigue behavior of SFRPs for two different loading conditions: (1) PP-GF30-20D with $S_{\max}$ =70 MPa and R = 0.1 and (2) PP-GF30-90D with $S_{\max}$ =30 MPa and R = -1.

3.4.5.1. Case (1) PP-GF30-20D, S_{max}=70 MPa, R=0.1

Figure 3-12 shows the NFF of decomposed pseudograins and their fatigue lifetime (number of cycles on x axis below circle symbols). When the RVE is subjected to the maximum stress during the fatigue cycle, 12 pseudograins experience different NFF (ranging from 0.278 to 0.898) and lifetime (ranging from 110 to 526341) as shown in **Figure 3-12(a)**. Clearly it can be confirmed that first or last pseudograin failure criterion are not suitable for predicting RVE failure of SFRPs (see two lifetimes and experimentally determined lifetime). In contrast, the predicted lifetime by PPDA model has a good agreement with the experimental results.

3.4.5.1. Case (2) PP-GF30-90D, S_{max}=30 MPa, R=-1

Figure 3-12(b) shows the NFF of decomposed pseudograins and their fatigue lifetime (represented by circle symbols) of case (2). 12 pseudograins have similar NFF (ranging from 0.611 to 0.642) and lifetime (ranging from 1345 to 1942). Since the pseudograins fail almost simultaneously, all RVE failure decision criteria can predict a reasonable lifetime.

In case (2), pseudograins have similar fatigue lifetime so that RVE failure decision method does not have a significant impact, whereas in case (1), we observed significant difference. This is because the fiber orientation tensor of SFRPs in case (1) shows random fiber distribution compared to case (2) (See **Equation (60)**). After the pseudograin decomposition process, the 12 pseudograins have significantly different fiber orientations, leading to significant differences in NFF between pseudograins as shown in **Figure 3-12(a)**. Therefore, first and last pseudograin failure criterion lead to inaccurate predictions for case (1). In contrast, PPDA model in this study considers all 12 pseudograin failures and damage inside them considering the stress concentration caused by constraining effect throughout the cycles of the RVE. Therefore, PPDA model can predict the fatigue life of SFRPs with different fiber orientation tensors, and is also more suitable than other failure models for simulating real parts.

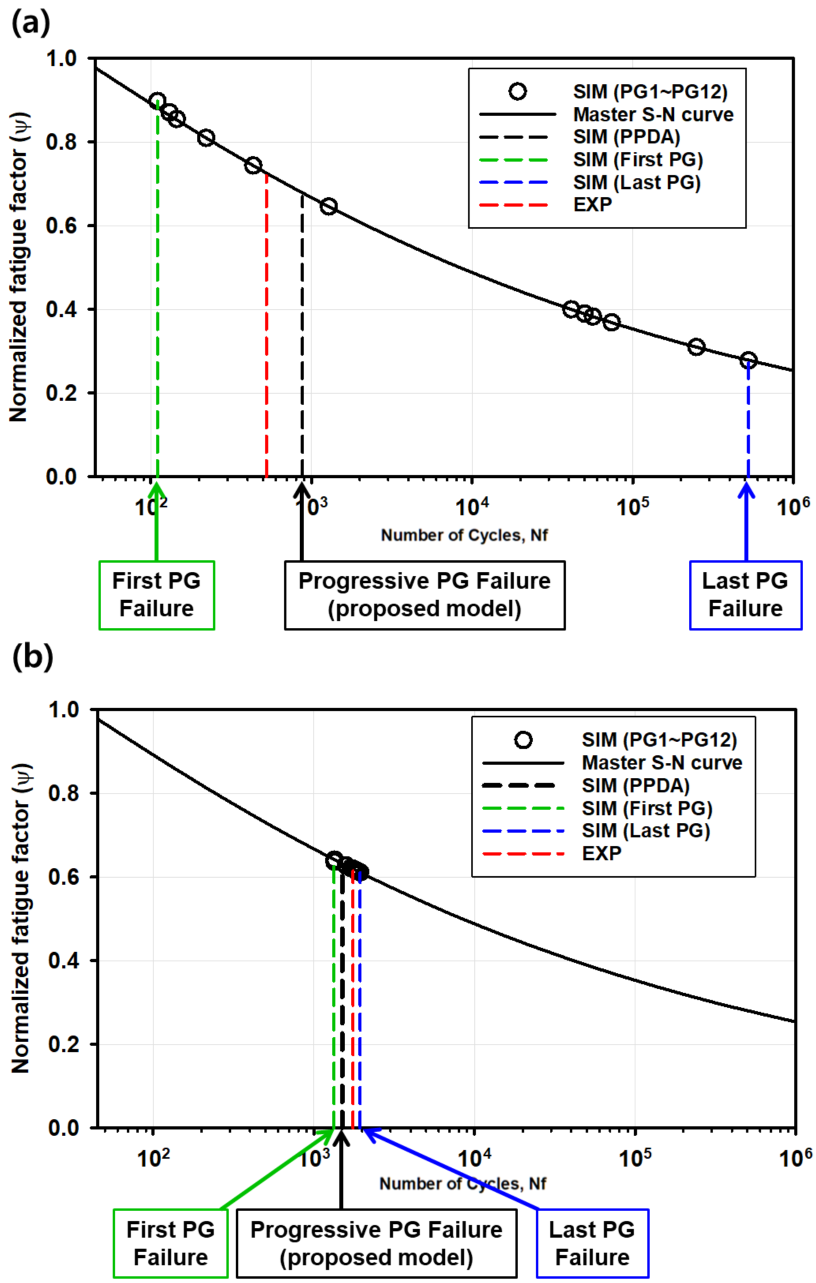

Figure 3-12 NFF of decomposed pseudograins and their fatigue lifetime, and comparison of fatigue failure criterion (first pseudograin failure, last pseudograin failure, and PPDA model) with experimental results. (a) case (1) and (b) case (2).

3.5. Summary

In this study, to predict fatigue lifetime in SFRPs, we proposed a novel PPDA model, which has not been reported in literature. The proposed model consists of two stages: (1) calculation of fatigue damage of each pseudograin and (2) failure determination of RVE considering progressive pseudograin failures. In the first stage, Chaboche fatigue damage model was used for the non-linear damage accumulation of pseudograins and NFF was used to consider their anisotropic fatigue characteristics. In the second stage, we considered the stress concentration and accumulation of fatigue damages accelerated by it, finally determining a reasonable RVE fatigue failure. We implemented PPDA model into UMAT and compared the predicted S-N curves with experimental data. In the first stage, the combination of Chaboche fatigue damage model and NFF was compared with Tsai-Hill fatigue indicator, showing similar accuracy but better suitability for the PPDA model. In the second stage, the PPDA model showed better predictions of fatigue life compared to the first pseudograin failure or last pseudograin failure approach. Overall, the proposed model is a promising approach for predicting the fatigue behavior of SFRPs and can potentially be extended to other composite materials.

Chapter 4. Application of PPDA model to creep-fatigue interaction behavior

4.1. Constitutive modeling

4.1.1. Creep damage model of pseudograin

4.1.1.1. Tsai-Wu effective stress

Assuming that pseudograin is transversely isotropic and that σ_{23} is negligible, it can be expressed as follows:

$$TW(\boldsymbol{\sigma}_{ij}) = [F_{11}\boldsymbol{\sigma}_{11}^2 + F_{22}(\boldsymbol{\sigma}_{22}^2 + \boldsymbol{\sigma}_{33}^2) + F_{66}(\boldsymbol{\sigma}_{12}^2 + \boldsymbol{\sigma}_{13}^2)] + [F_1\boldsymbol{\sigma}_{11} + F_2(\boldsymbol{\sigma}_{22} + \boldsymbol{\sigma}_{33})] = 1$$

$$F_1 = \frac{1}{X_t} - \frac{1}{X_c}\ ,\quad F_2 = \frac{1}{Y_t} - \frac{1}{Y_c}\ ,\quad F_{11} = \frac{1}{X_t X_c}\ ,\quad F_{11} = \frac{1}{X_t X_c}\ ,\quad F_{22} = \frac{1}{Y_t Y_c}\ ,\quad F_{66} = \frac{1}{S^2} \tag{64}$$

The left-hand side of **Equation (64)** represents a distance from origin to the failure envelope [120]. In this study, non-dimensional Tsai-Wu effective stress is defined as the distance from origin to the failure envelope, representing the ratio of the magnitude of the current stress state to the static failure of the composites. With this definition, non-dimensional Tsai-Wu effective stress is expressed as follows:

$$\xi = \frac{2[F_{11}\sigma_{11}^2 + F_{22}(\sigma_{22}^2 + \sigma_{33}^2) + F_{66}(\sigma_{12}^2 + \sigma_{13}^2)]}{-[F_1\sigma_{11} + F_2(\sigma_{22} + \sigma_{33})] + \sqrt{[F_1\sigma_{11} + F_2(\sigma_{22} + \sigma_{33})]^2 + 4[F_{11}\sigma_{11}^2 + F_{22}(\sigma_{22}^2 + \sigma_{33}^2) + F_{66}(\sigma_{12}^2 + \sigma_{13}^2)]}} \quad (65)$$

4.1.1.2. Chaboche and Lemaitre creep damage model

After converting the multiaxial stress state of pseudograin to a universal scalar quantity (ξ), a creep damage model is required to predict the lifetime of pseudograins. In this study, Chaboche and Lemaitre creep damage model was used for this purpose. Chaboche and Lemaitre suggested a non-linear creep damage evolution model [139]. This model expressed as:

$$\frac{dD_c}{dt} = \left(\frac{S_{creep}}{A}\right)^r (1 - D_c)^{-K} \quad (66)$$

where D_c is the creep damage variable, S_{creep} is the creep stress, and A, r, K are constants.

By applying Tsai-Wu effective stress to Chaboche fatigue damage model, **Equation (65)** was combined with **(66)**, resulting in the following creep damage equations for pseudograins:

$$\frac{dD_c}{dt} = \left(\frac{\xi}{A}\right)^r (1 - D_c)^{-K} \quad (67)$$

Integrating damage from 0 to 1 in **Equation (67)**, creep rupture time (t_c) can be expressed as:

$$t_c = \frac{1}{(K+1)}\left(\frac{A}{\xi}\right)^r \tag{68}$$

Furthermore, damage at creep time t can be obtained by integrating time $t=0$ to t_c as follows.

$$D_c = 1-\left(1-\frac{t}{t_c}\right)^{\frac{1}{K+1}} \tag{69}$$

We obtained Chaboche and Lemaitre creep damage parameters from creep tests reported in the literature [137]. Short glass fiber-reinforced plastics with polypropylene were used in the literature. The weight fraction of GF was 30% and fiber orientation is transverse to the load applied (PP-GF30-90D). Creep tests result data is shown in in **Figure 4-1(a)**. Creep data was converted to creep master curve using Tsai-Wu effective stress. The data was obtained from figures in paper (**Figure 4-1(a)**) by image digitizing using Grabit.m file in Matlab program. Creep parameters for the master curve were obtained and are listed in **Table 4-1**. Details of parameter identification methods are given in reference [137]. The value of parameter K was assumed to be 7.5, which is the value of PP-GF obtained from the same reference [137]. The master creep curve obtained by the damage model is shown in **Figure 4-1(b)**.

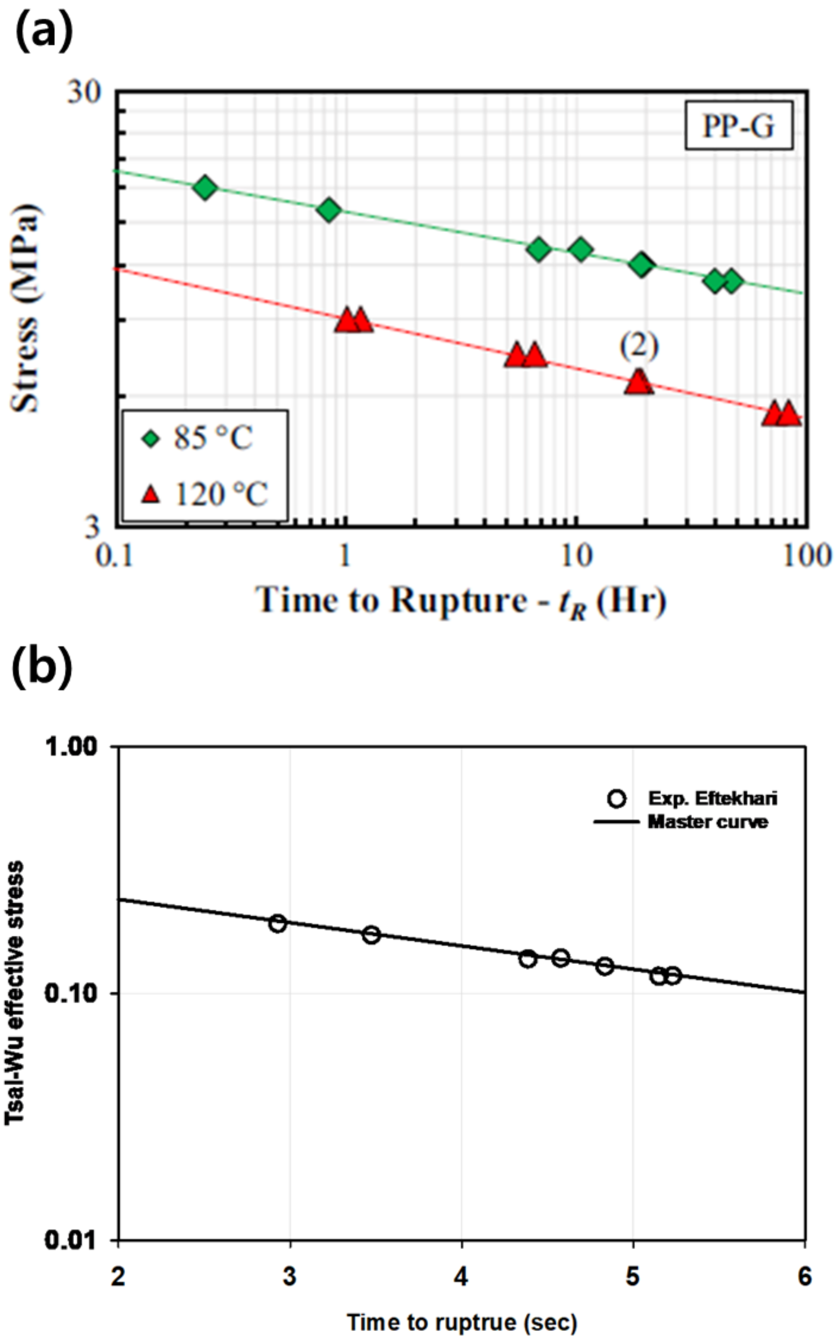

Figure 4-1 (a) Creep curve of PP-GF30 [137] and (b) master creep curve using Tsai-Wu effective stress.

Table 4-1 Chaboche and Lemaitre creep damage model parameters of master creep curve.

Chaboche and Lemaitre creep damage model parameters	
Non-linear parameter (K)	7.5
Chaboche constant 1 (r)	10.6
Chaboche constant 2 (A)	0.44

4.1.2. Creep-fatigue interaction model of pseudograin

Constitutive modeling for fatigue damage model of a pseudograin in SFRPs is developed in Section 3.2.3 using normalized fatigue factor and Chaboche fatigue damage model. In addition, constitutive modeling for creep damage model of a pseudograin in SFRPs is developed in Section 4.1.1 using Tsai-Wu effective stress and Chaboche and Lemaitre creep damage model. When the creep damage (linked to the loading duration) and fatigue damage (due to cyclic loading) are present simultaneously, the interaction effect can be represented macroscopically by introducing a coupling as:

$$dD = dD_c + dD_f \tag{70}$$

By combining , **Equation (70)** was combined with **(44)** and **(67)**, resulting in the following creep-fatigue interaction damage equations for pseudograins:

$$\frac{dD}{dN_R} = \left(\frac{\xi}{A}\right)^r \left(1-D\right)^{-K} + [1-(1-D)^{\beta+1}]^{\alpha} \left(\frac{\psi_{\max}}{M_0(1-D)}\right)^{\beta} \tag{71}$$

We obtained Chaboche fatigue damage parameters from creep and fatigue test results reported in the literature [140]. Eftekhari, M. et al. used short glass fiber-reinforced plastics with polypropylene. The weight fraction of GF was 30% and fiber orientation is transverse to the load applied (PP-GF30-90D) which is the same material in Section 4.1.1. Therefore, we used creep damage parameters listed in **Table 4-1**, and fatigue damage parameters were obtained from the literature. Fatigue tests result data in the literature is shown in in **Figure 4-2**. The data was obtained from figures in paper (**Figure 4-2**) by image digitizing using Grabit.m file in Matlab program. Fatigue S-N curve data was converted to master S-N curve using normalized fatigue factor in Section 3.2.3. The master S-N curve obtained by the damage model is shown in **Figure 4-3**. Fatigue parameters for the master curve were obtained and are listed in **Table 4-2**.

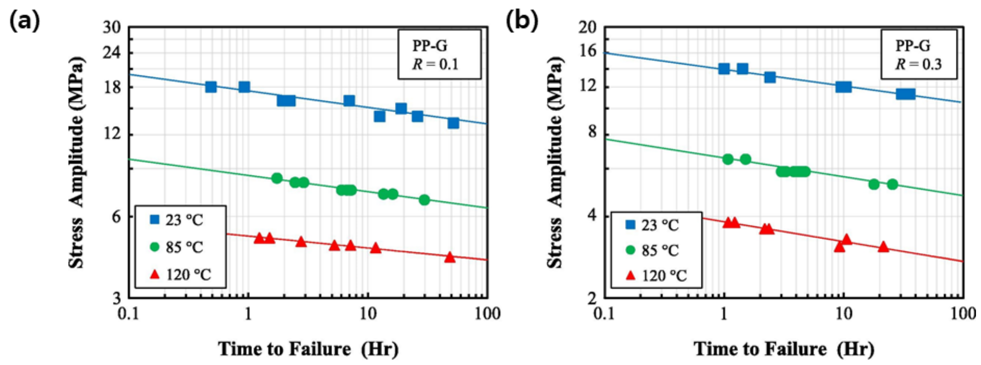

Figure 4-2 Fatigue S-N curve of PP-GF30 at the stress ratio of (a) 0.1 and (b) 0.3 [140].

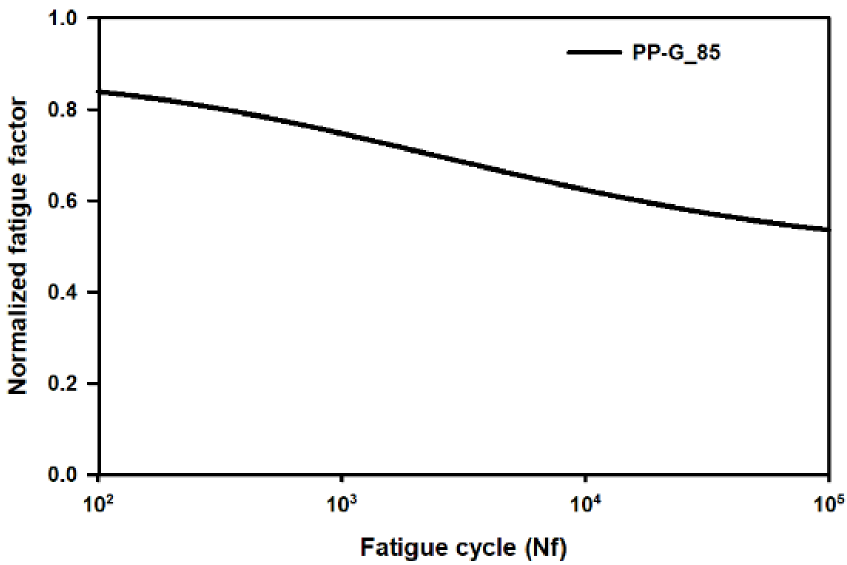

Figure 4-3 Master S-N curve using fatigue data in [140] and normalized fatigue factor.

Table 4-2 Chaboche fatigue damage model parameters of PP-GF30 master curve [140].

Chaboche fatigue damage model parameters	
Ultimate normalized fatigue factor (ψ_u)	1.2
Fatigue endurance limit (ψ_{l0})	0.01
Non-linear parameter (a)	0.65
Chaboche constant 1 (β)	5.06
Chaboche constant 2 (M_0)	1.067

4.1.3. PPDA model for creep-fatigue interaction behavior

After the creep-fatigue lifetime of each pseudograin is obtained using **Equation (72)**, the overall failure of RVE is predicted by PPDA model. We assume that the RVE in the fatigue loading is composed of k pseudograins: PG_i (i=1, 2, …, k). The creep-fatigue life of pseudograins is expressed by $N_{R.i}$ (i=1, 2, …, k) integrating the **Equation (73)** from $D=0$ to $D=1$ Here, assume that PG_1 is a pseudograin with the shortest lifetime and PG_k is the pseudograin with the longest lifetime. Once PG_1 has failed first, all pseudgrains are cycled through $N_{R.1}$ block cycles. At this block cycle ($N_{R.1}$), the stress of the other pseudograins (PG_i) is concentrated due to following two reasons: (a) accumulated damage in the PG_i until the cycle $N_{R.1}$ and (b) loss of the load-bearing ability of PG_1. First, accumulated damage of the other pseudograins is calculated using **Equation (71)** as follows:

$$D_{i.1} = 1 - \left(1 - \left(\frac{N_{R.1}}{N_{R.i}}\right)^{\frac{1}{1-\alpha}}\right)^{\frac{1}{\beta+1}} - \left(1 - \frac{N_{R.1}}{N_{R.i}}\right)^{\frac{1}{K+1}} \tag{74}$$

where $D_{i.1}$ is accumulated damage in PG_i at $N_{R.1}$ cycles. In terms of mechanical parameters, damage $D_{i.1}$ can be expressed by means of a net area reduction [125]. As the damage represents the loss of effective area taking into account local stress concentrations, one can write:

$$\psi_{i.D} = \frac{\psi_i}{(1 - D_{i.1})}, \ \xi_{i.D} = \frac{\xi_i}{(1 - D_{i.1})} \tag{75}$$

where $\psi_{i.D}$ and $\xi_{i.D}$ are damaged NFF and Tsai-Wu effective stress.

Then, the failure of PG_1 is modeled assuming that it is still capable of transferring the load to the other pseudograins and thus stress redistribution happens. After the redistribution, stress concentration effect of other pseudograins is reflected in the NFF and Tsai-Wu effective stress as follows:

$$\psi_{i.1} = K\psi_{i.D}, \ \xi_{i.1} = K'\xi_{i.D} \tag{76}$$

where $\psi_{i.1}$ and $\xi_{i.1}$ are concentrated NFF at $N_{R.1}$. K and K' are stress concentration factors due to the failure of PG_1.

The procedure to calculate stress concentration factor K is explained in Section 3.2.4. Another stress concentration factor for creep stress K' is obtained by considering the Tsai-Wu effective stress of RVE based on the assumption used in the second step of homogenization procedure. Like in the calculation of K, Voigt model [56], which assumes an iso-strain condition, was adopted for the second step homogenization. Accordingly, the Tsai-Wu effective stress of RVE can be computed as the sum of the product of Tsai-Wu effective stress and the fraction of each pseudograin, as follows:

$$\xi_{RVE} = \sum_{i=1}^{k} w_i \xi_i \tag{77}$$

where ξ_{RVE} is Tsai-Wu effective stress of RVE before PG_1 fails. After PG_1 fails, Tsai-Wu effective stress of RVE (ξ'_{RVE}) can be expressed as follows:

$$\xi'_{RVE} = K' \sum_{i=2}^{k} w_i \xi_i \tag{78}$$

It is assumed that Tsai-Wu effective stress of RVE is unchanged before and after the pseudograin failure ($\xi_{RVE} = \xi'_{RVE}$). Then, the stress concentration factor can be derived as follows:

$$K' = \frac{\sum_{i=1}^{k} w_i \xi_i}{\sum_{i=2}^{k} w_i \xi_i} \tag{79}$$

The concentrated Tsai-Wu effective stress of other pseudograins after the first pseudograin failure can be calculated using **Equations (75), (76)** and **(79)** as follows:

$$\xi_{i.1} = K' \xi_{i.D} = \frac{\sum_{i=1}^{k} w_i \xi_i}{\sum_{i=2}^{k} w_i \xi_i} \frac{\xi_i}{(1 - D_{i.1})} \tag{80}$$

Then, the remaining life of PG_2 ($n_{R.2}$) can be obtained as follows:

$$n_{R.2} = \int_{D=D_{i.1}}^{1} \left[\left(\frac{\xi_{i.1}}{A} \right)^{r} \left(1-D\right)^{-K} + [1-(1-D)^{\beta+1}]^{\alpha} \left(\frac{\psi_{i.1}}{M_0(1-D)} \right)^{\beta} \right]^{-1} dD \qquad (81)$$

The same procedure is then repeated after the failure of PG_2, PG_3 $\cdots$ PG_k. Finally, the creep-fatigue life of the RVE is obtained by,

$$N_{R.RVE} = N_{R.1} + n_{R.2} + \cdots + n_{R.k} = N_{R.1} + \sum_{i=2}^{k} n_{R.i} \qquad (82)$$

4.2. Validation of PPDA for creep behavior

4.2.1. Creep behavior of pseudograin

The reconstruction of orientation distribution function (ODF) and pseudograin decomposition procedure for 12 pseudograins were implemented in UMAT. Then, the VEVP model and mean-field homogenization method described in the previous sections were implemented. The PPDA model developed in this study were also implemented in UMAT. The re-simulation of PP-GF30-0D creep case were performed as follows. Elastic modulus of 72.40 GPa, Poisson's ratio of 0.22 and fiber aspect ratio of 25 were used for glass fiber in simulation. Poisson's ratio of 0.43 was used for the PP matrix in simulation.

A cubic geometry of size 6×6×6 mm was created and meshed with a C3D8 element of size 1×1×1 mm. The U1=0, U2=0, and U3=0 boundary conditions were applied to the plane perpendicular to the x-, y-, and z-axis in the negative direction, respectively. A creep stress (S_{creep}) in **Table 4-3** was applied to the plane perpendicular to the x-axis in the positive direction. Varying the creep stress, the creep behavior of PP-GF30-0D were simulated.

The simulation results are presented in **Figure 4-5.** Creep stress-rupture time curve shows a good agreement with experimental results, confirming that creep PPDA model implemented in ABAQUS can properly capture the creep behavior of SFRPs.

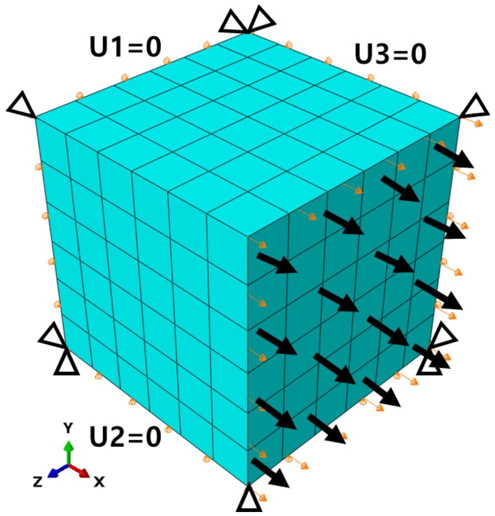

Figure 4-4 Geometry, mesh information, boundary condition of creep test and creep-fatigue interaction test simulation.

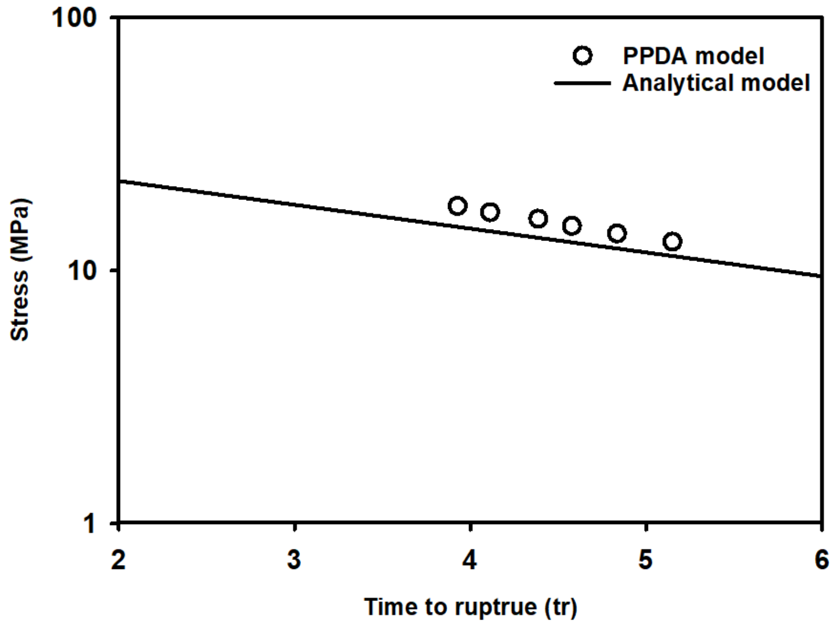

Figure 4-5 Creep simulation result.

Table 4-3 Boundary condition of creep test simulation.

Creep stress (S_{creep})
19 MPa
18 MPa
17 MPa
16 MPa
15 MPa
14 MPa

4.2.2. Comparison of PPDA creep model with other RVE failure criterion

The creep failure of RVE can be decided using various criteria, e.g., first creep pseudograin failure, last creep pseudograin failure, and PPDA model in this study. In this section, these criteria are compared by simulating the creep behavior of SFRPs for PP-GF30-0D with S_{creep}=16 MPa.

Figure 4-6 shows the Tsai-Wu effective stress of decomposed pseudograins and their creep rupture time (represented by circle symbols). 12 pseudograins have similar Tsai-Wu effective stress (ranging from 0.101 to 0.164) and creep rupture time (ranging from 8745 to 11242). Since the pseudograins fail almost simultaneously, all RVE failure decision criteria can predict a reasonable lifetime.

After the pseudograin decomposition process, the 12 pseudograins have significantly different fiber orientations, leading to significant differences in Tsai-Wu effective stress between pseudograins as shown in **Figure 4-6**. Therefore, first and last pseudograin creep failure criterion lead to inaccurate predictions of creep rupture time. In contrast, PPDA model in this study considers all 12 pseudograin creep rupture behavior and damage inside them considering the stress concentration caused by constraining effect throughout the creep loading of the RVE. Therefore, PPDA model can predict the creep rupture time of SFRPs with different fiber orientation tensors, and is also more suitable than other failure models for simulating real parts.

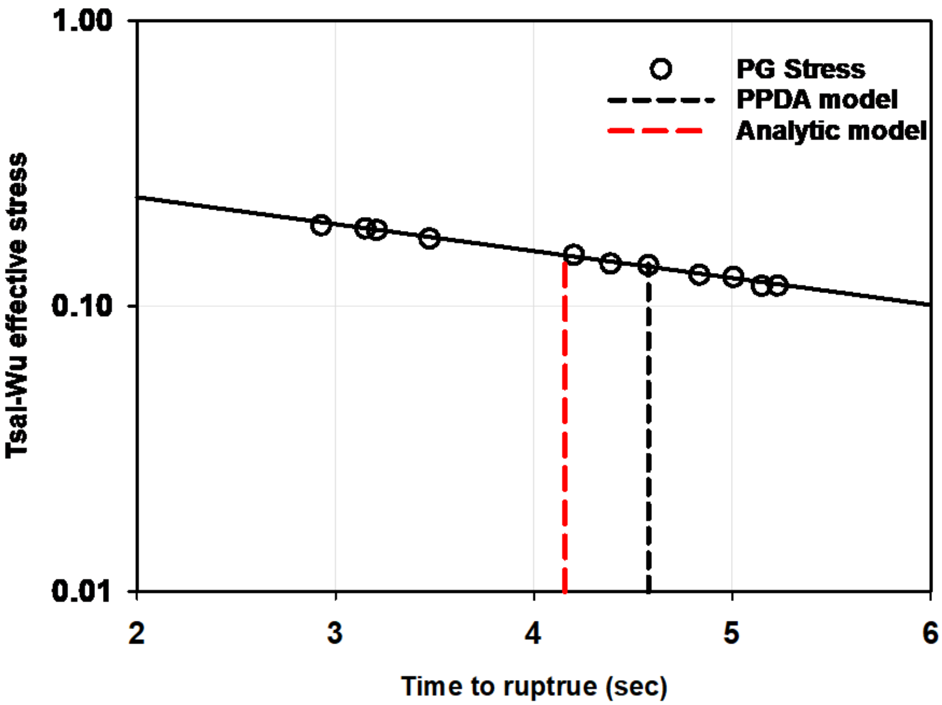

Figure 4-6 Tsai-Wu effective stress of pseudograins when 16 MPa creep stress applied on RVE.

4.3. Validation of PPDA model for creep-fatigue interaction effect

A cubic geometry of size 6×6×6 mm was created and meshed with a C3D8 element of size 1×1×1 mm. The U1=0, U2=0, and U3=0 boundary conditions were applied to the plane perpendicular to the x-, y-, and z-axis in the negative direction, respectively. Block of fatigue cycles and creep stress were applied. One fatigue cycle of 5 Hz frequency is applied first and creep stress of half maximum stress of maximum fatigue stress were applied after the fatigue cycle. Repeated blocks were applied to the plane perpendicular to the x-axis in the positive direction. Varying maximum load of sine wave and stress ratio, the fatigue tests of three different specimens (PP-GF30-0D, 20D, 90D) were simulated as shown in **Table 4-4**.

A summary of experimental results under creep-fatigue loading condition is presented in **Table 4-4**, and simulation results are shown in **Figure 4-7**. The nonlinear behavior can also be observed from the cross plots of fatigue life ratio versus hold-time life ratio, shown in **Figure 4-8**. Sum of the life ratios (sum of the cyclic and hold-time damages based on LDR) is less than unity for all the conditions which confirms a non-linear behavior in terms of damage accumulation. Re-simulation results were conducted for most of the conditions and very good repeatability of results were obtained.

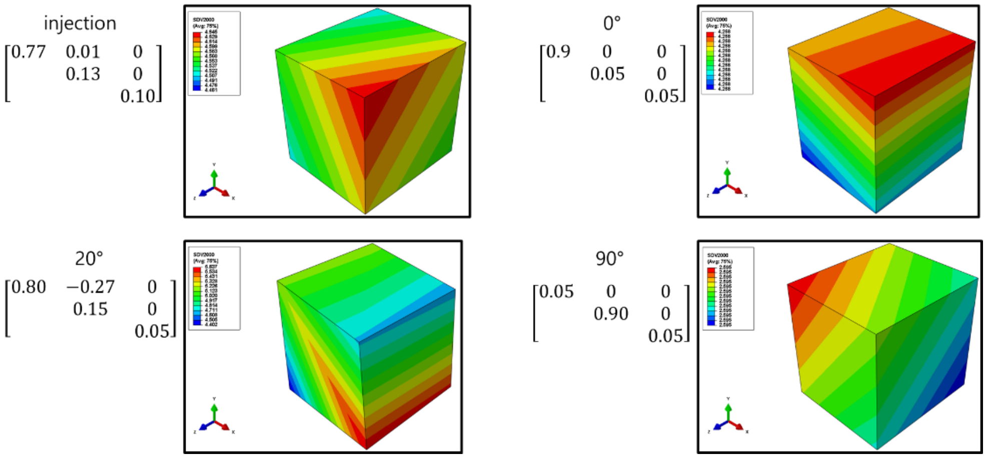

Figure 4-7 Creep-fatigue interaction simulation result of SFRPs.

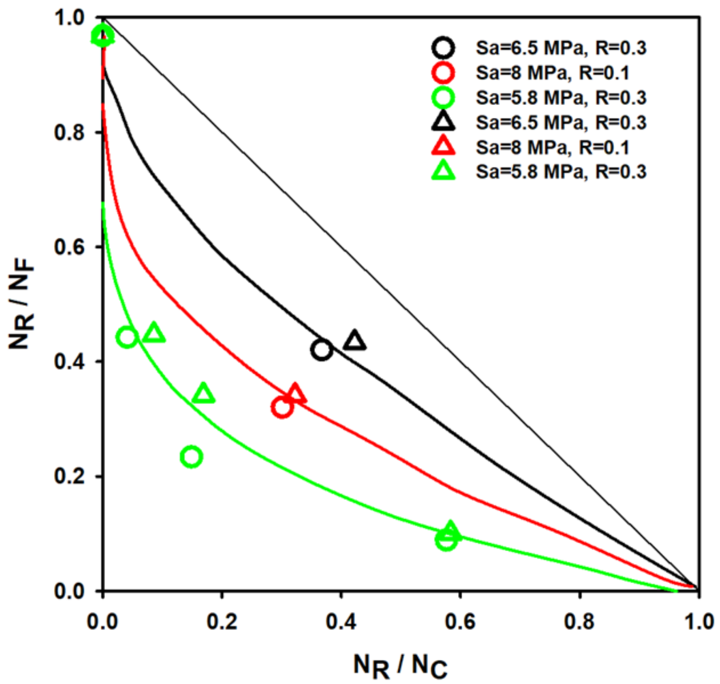

Figure 4-8 Prediction of the non-linear interaction for cyclic and hold-time damages for SFRPs. Data points are experimental and UMAT results. Curves are predictions of Chaboche model and solid line is prediction of linear damage rule

Table 4-4 Boundary condition of creep-fatigue interaction test simulation.

Boundary conditions			
Stress ratio	Maximum fatigue stress (MPa)	Creep stress (MPa)	Hold time (s)
0.3	16.72	10.9	13
0.3	16.72	10.9	39
0.3	16.72	10.9	73
0.3	17.76	9.8	243
0.1	18.58	12	19.2

4.4. Summary

In this study, to predict creep-fatigue interaction effect of SFRPs, we extended use of the PPDA model proposed in Chapter 3. The proposed model consists of two stages: (1) calculation of creep and fatigue damage of each pseudograin and (2) failure determination of RVE considering progressive pseudograin failures. The PPDA model is successfully implemented into ABAQUS user material subroutine (UMAT), predicting the creep lifetime and creep-fatigue interaction effect of SFRPs in good agreement with experimental data.

Chapter 5. Conclusion

This study aimed to detect and model the damage of composite materials, and then to apply feature of damage and theoretical damage model to predict mechanical behavior of the composite materials.

Delamination damage was detected by AE technique, and FLD of steel–polymer sandwich composites was constructed. Our approach relied on monitoring to detect delamination, which was identified by a peak frequency band in the range of 300-500 kHz. We also conducted numerical simulations using the cohesive zone model to investigate the effects of interfacial properties and damage on formability. Our results showed that stronger interfacial properties led to improved formability by reducing the risk of delamination. Overall, our approach provides a valuable tool for optimizing the design and processing of steel–polymer sandwich composites for various industrial applications.

Progressive pseudograin damage accumulation model to predict fatigue lifetime in SFRPs was developed. The proposed model consists of two stages: (1) calculation of fatigue damage of each pseudograin and (2) failure determination of RVE considering progressive pseudograin failures. In the first stage, Chaboche fatigue damage model was used for the non-linear damage accumulation of pseudograins and NFF was used to consider their anisotropic fatigue characteristics. In the second stage, we considered stress concentration and accumulation of fatigue damages accelerated by it, finally determining a reasonable RVE fatigue failure. We implemented PPDA model into UMAT and compared the predicted S-N curves with experimental data. In the first stage, the combination of Chaboche fatigue damage model and NFF was compared with Tsai-Hill fatigue indicator, showing similar accuracy but better suitability for the PPDA model. In the second stage, the PPDA model showed better predictions of fatigue life compared to the first pseudograin failure or last pseudograin failure approach.

The PPDA model was expanded to encompass the creep behavior and the interaction between creep and fatigue effects of SFRPs. We implemented the PPDA model into UMAT and compared the predicted creep curves with experimental data available in literature. The results demonstrated that the PPDA model outperformed the first pseudograin failure or last pseudograin failure approaches in terms of predicting creep life. Subsequently, we employed the PPDA model to forecast creep-fatigue tests, which involved repeated block loading combined with fatigue cycling and creep holding time. The simulation outcomes indicated that the PPDA model effectively captured the nonlinearity exhibited by the creep-fatigue behavior of SFRPs. Overall, the proposed model is a promising approach for predicting the creep-fatigue behavior of SFRPs and can potentially be extended to other composite materials.

Reference

1. *CO2 Emissions in 2022*. 2023, International Energy Agency (IEA).
2. Fuchs, E.R., et al., *Strategic materials selection in the automobile body: Economic opportunities for polymer composite design.* Composites science and technology, 2008. **68**(9): p. 1989-2002.
3. Ashby, M.F. and Y.J. Bréchet, *Designing hybrid materials.* Acta materialia, 2003. **51**(19): p. 5801-5821.
4. Harhash, M., E. Abd, and M. Hamid, *Forming behaviour of multilayer metal/polymer/metal systems*. 2017.
5. Engel, B. and J. Buhl, *Metal Forming of Vibration-Damping Composite Sheets.* Steel Research International, 2011. **82**(6): p. 626-631.
6. Christke, S., et al., *Multi-layer polymer metal laminates for the fire protection of lightweight structures.* Materials & Design, 2016. **97**: p. 349-356.
7. Liao, F.-S., A.-C. Su, and T.-C.J. Hsu, *Damping behaviour of dynamically cured butyl rubber/polypropylene blends.* Polymer, 1994. **35**(12): p. 2579-2586.
8. Zhang, S.H. and H.L. Chen, *A study on the damping characteristics of laminated composites with integral viscoelastic layers.* Composite Structures, 2006. **74**(1): p. 63-69.
9. Bateman, M.J., K.S. Kim, and Y.S. Shin, *Constrained viscoelastic layer damping of thick aluminum plates: Design, analysis and testing*. 1990, NAVAL POSTGRADUATE SCHOOL MONTEREY CA.
10. Ayrilmis, N., *Effect of fire retardants on internal bond strength and bond durability of structural fiberboard.* Building and environment, 2007. **42**(3): p. 1200-1206.
11. Malushte, H.S., *Evaluation of Statistical Energy Analysis for prediction of*

breakout noise from air duct. 2013.

12. Christke, S., et al., *Multi-layer polymer metal laminates for the fire protection of lightweight structures.* Materials & Design, 2016. **97**: p. 349-356.
13. Stachowiak, G.W. and A.W. Batchelor, *Engineering tribology*. 2013: Butterworth-heinemann.
14. Gruber, G., A. Haimerl, and S. Wartzack, *Consideration of orientation properties of short fiber reinforced polymers within early design steps.* FEA Inf. Eng. J, 2013. **2**: p. 2167-2173.
15. Mortazavian, S. and A. Fatemi, *Fatigue behavior and modeling of short fiber reinforced polymer composites: A literature review.* International Journal of Fatigue, 2015. **70**: p. 297-321.
16. Fu, S.-Y., B. Lauke, and Y.-W. Mai, *Science and engineering of short fibre-reinforced polymer composites*. 2019: Woodhead Publishing.
17. Bernasconi, A., M. Carboni, and R. Ribani, *On the combined use of Digital Image Correlation and Micro Computed Tomography to measure fibre orientation in short fibre reinforced polymers.* Composites Science and Technology, 2020. **195**: p. 108182.
18. Luan, C., et al., *Towards next-generation fiber-reinforced polymer composites: a perspective on multifunctionality.* Functional Composites and Structures, 2019. **1**(4): p. 042002.
19. Ballout, W., et al., *High performance recycled CFRP composites based on reused carbon fabrics through sustainable mild solvolysis route.* Scientific Reports, 2022. **12**(1): p. 5928.
20. Tanaka, K., et al., *Fatigue crack propagation in short-carbon-fiber reinforced plastics evaluated based on anisotropic fracture mechanics.* International Journal of Fatigue, 2016. **92**: p. 415-425.
21. Li, Z., et al., *An innovative computational framework for the analysis of complex mechanical behaviors of short fiber reinforced polymer composites.*

Composite Structures, 2021. **277**: p. 114594.

22. Sato, N., et al., *Microfailure behaviour of randomly dispersed short fibre reinforced thermoplastic composites obtained by direct SEM observation.* Journal of materials science, 1991. **26**: p. 3891-3898.

23. Chon, C.T. and C. Sun, *Stress distributions along a short fibre in fibre reinforced plastics.* Journal of Materials Science, 1980. **15**: p. 931-938.

24. Okereke, M.I., C.P. Buckley, and A.I. Akpoyomare, *The mechanism of rate-dependent off-axis compression of a low fibre volume fraction thermoplastic matrix composite.* Composite Structures, 2017. **168**: p. 685-697.

25. Sket, F., et al., *Automatic quantification of matrix cracking and fiber rotation by X-ray computed tomography in shear-deformed carbon fiber-reinforced laminates.* Composites Science and Technology, 2014. **90**: p. 129-138.

26. Yokozeki, T., et al., *Effects of layup angle and ply thickness on matrix crack interaction in contiguous plies of composite laminates.* Composites Part A: Applied Science and Manufacturing, 2005. **36**(9): p. 1229-1235.

27. Sket, F., et al., *Determination of damage micromechanisms and fracture resistance of glass fiber/epoxy cross-ply laminate by means of X-ray computed microtomography.* Composites Science and Technology, 2012. **72**(2): p. 350-359.

28. Aymerich, F. and S. Meili, *Ultrasonic evaluation of matrix damage in impacted composite laminates.* Composites Part B: Engineering, 2000. **31**(1): p. 1-6.

29. Sihn, S., et al., *Experimental studies of thin-ply laminated composites.* Composites Science and Technology, 2007. **67**(6): p. 996-1008.

30. Yokozeki, T., Y. Aoki, and T. Ogasawara, *Experimental characterization of strength and damage resistance properties of thin-ply carbon fiber/toughened epoxy laminates.* Composite Structures, 2008. **82**(3): p. 382-389.

31. Kyriazoglou, C., B. Le Page, and F. Guild, *Vibration damping for crack*

detection in composite laminates. Composites Part A: Applied Science and Manufacturing, 2004. **35**(7-8): p. 945-953.

32. Seo, D.-C. and J.-J. Lee, *Damage detection of CFRP laminates using electrical resistance measurement and neural network.* Composite structures, 1999. **47**(1-4): p. 525-530.
33. Zhang, L., et al., *Fatigue failure mechanism analysis and life prediction of short fiber reinforced polymer composites under tension-tension loading.* International Journal of Fatigue, 2022. **160**: p. 106880.
34. Sokolova, O.A., A. Carrado, and H. Palkowski, *Metal–polymer–metal sandwiches with local metal reinforcements: A study on formability by deep drawing and bending.* Composite Structures, 2011. **94**(1): p. 1-7.
35. Liu, J., W. Liu, and W. Xue, *Forming limit diagram prediction of AA5052/polyethylene/AA5052 sandwich sheets.* Materials & Design, 2013. **46**: p. 112-120.
36. Kim, K., et al., *Formability of AA5182/polypropylene/AA5182 sandwich sheets.* Journal of Materials Processing Technology, 2003. **139**(1-3): p. 1-7.
37. Weiss, M., et al., *The influence of temperature on the forming behavior of metal/polymer laminates in sheet metal forming.* 2007.
38. Parsa, M. and M. Ettehad, *Experimental and finite element study on the spring back of double curved aluminum/polypropylene/aluminum sandwich sheet.* Materials & Design, 2010. **31**(9): p. 4174-4183.
39. Parsa, M., et al., *Experimental and numerical determination of limiting drawing ratio of Al3105-polypropylene-Al3105 sandwich sheets.* Journal of engineering materials and technology, 2010. **132**(3).
40. Sokolova, O., A. Carradó, and H. Palkowski. *Production of customized high-strength hybrid sandwich structures*. in *Advanced materials research*. 2010. Trans Tech Publ.
41. LIU, J.-g., L. Wei, and J.-x. WANG, *Influence of interfacial adhesion strength on formability of AA5052/polyethylene/AA5052 sandwich sheet.*

Transactions of Nonferrous Metals Society of China, 2012. **22**: p. s395-s401.

42. Liu, J.-g. and X. Wei, *Formability of AA5052/polyethylene/AA5052 sandwich sheets.* Transactions of Nonferrous Metals Society of China, 2013. **23**(4): p. 964-969.

43. Forcellese, A. and M. Simoncini, *Mechanical properties and formability of metal–polymer–metal sandwich composites.* The International Journal of Advanced Manufacturing Technology, 2020: p. 1-17.

44. Kazemi, F., R. Hashemi, and S.A. Niknam, *Formability and fractography of AA5754/polyethylene/AA5754 sandwich composites.* Mechanics Based Design of Structures and Machines, 2020: p. 1-15.

45. Parsa, M., M. Ettehad, and P. Matin, *Forming limit diagram determination of Al 3105 sheets and Al 3105/polypropylene/Al 3105 sandwich sheets using numerical calculations and experimental investigations.* Journal of engineering materials and technology, 2013. **135**(3).

46. Bleck, W., et al., *A comparative study of the forming-limit diagram models for sheet steels.* Journal of Materials Processing Technology, 1998. **83**(1-3): p. 223-230.

47. Sun, C.-T. and R.S. Vaidya, *Prediction of composite properties from a representative volume element.* Composites science and Technology, 1996. **56**(2): p. 171-179.

48. Feyel, F., *Multiscale FE2 elastoviscoplastic analysis of composite structures.* Computational Materials Science, 1999. **16**(1-4): p. 344-354.

49. Breuer, K. and M. Stommel, *Prediction of short fiber composite properties by an artificial neural network trained on an rve database.* Fibers, 2021. **9**(2): p. 8.

50. Pierard, O., C. Friebel, and I. Doghri, *Mean-field homogenization of multi-phase thermo-elastic composites: a general framework and its validation.* Composites Science and Technology, 2004. **64**(10-11): p. 1587-1603.

51. Eshelby, J.D., *The determination of the elastic field of an ellipsoidal*

inclusion, and related problems. Proceedings of the royal society of London. Series A. Mathematical and physical sciences, 1957. **241**(1226): p. 376-396.

52. Mori, T. and K. Tanaka, *Average stress in matrix and average elastic energy of materials with misfitting inclusions.* Acta metallurgica, 1973. **21**(5): p. 571-574.

53. Hill, R., *A self-consistent mechanics of composite materials.* Journal of the Mechanics and Physics of Solids, 1965. **13**(4): p. 213-222.

54. Nemat-Nasser, S. and M. Hori, *Micromechanics: overall properties of heterogeneous materials*. 2013: Elsevier.

55. McLaughlin, R., *A study of the differential scheme for composite materials.* International Journal of Engineering Science, 1977. **15**(4): p. 237-244.

56. Voigt, W., *Ueber die Beziehung zwischen den beiden Elasticitätsconstanten isotroper Körper.* Annalen der physik, 1889. **274**(12): p. 573-587.

57. Reuß, A., *Berechnung der fließgrenze von mischkristallen auf grund der plastizitätsbedingung für einkristalle.* ZAMM-Journal of Applied Mathematics and Mechanics/Zeitschrift für Angewandte Mathematik und Mechanik, 1929. **9**(1): p. 49-58.

58. Tian, W., et al., *Numerical evaluation on mechanical properties of short-fiber-reinforced metal matrix composites: Two-step mean-field homogenization procedure.* Composite Structures, 2016. **139**: p. 96-103.

59. Camacho, C.W., et al., *Stiffness and thermal expansion predictions for hybrid short fiber composites.* Polymer Composites, 1990. **11**(4): p. 229-239.

60. Friebel, C., I. Doghri, and V. Legat, *General mean-field homogenization schemes for viscoelastic composites containing multiple phases of coated inclusions.* International journal of solids and structures, 2006. **43**(9): p. 2513-2541.

61. Kammoun, S., et al., *First pseudo-grain failure model for inelastic composites with misaligned short fibers.* Composites Part A: Applied Science and Manufacturing, 2011. **42**(12): p. 1892-1902.

62. Jain, A., et al., *Pseudo-grain discretization and full Mori Tanaka formulation for random heterogeneous media: Predictive abilities for stresses in individual inclusions and the matrix.* Composites science and technology, 2013. **87**: p. 86-93.
63. Kammoun, S., et al., *Micromechanical modeling of the progressive failure in short glass–fiber reinforced thermoplastics–First Pseudo-Grain Damage model.* Composites part A: applied science and manufacturing, 2015. **73**: p. 166-175.
64. Ogierman, W. and G. Kokot, *Homogenization of inelastic composites with misaligned inclusions by using the optimal pseudo-grain discretization.* International Journal of Solids and Structures, 2017. **113**: p. 230-240.
65. Ogierman, W., *A new model for time-efficient analysis of nonlinear composites with arbitrary orientation distribution of fibres.* Composite Structures, 2021. **273**: p. 114310.
66. Gommers, B., I. Verpoest, and P. Van Houtte, *The Mori–Tanaka method applied to textile composite materials.* Acta Materialia, 1998. **46**(6): p. 2223-2235.
67. Weber, B., et al., *Improvements of multiaxial fatigue criteria computation for a strong reduction of calculation duration.* Computational materials science, 1999. **15**(4): p. 381-399.
68. Nciri, M., et al., *Modelling and characterisation of dynamic behaviour of short-fibre-reinforced composites.* Composite Structures, 2017. **160**: p. 516-528.
69. Amiri-Rad, A., et al., *An anisotropic viscoelastic-viscoplastic model for short-fiber composites.* Mechanics of Materials, 2019. **137**: p. 103141.
70. He, G., et al., *Constitutive modeling of viscoelastic–viscoplastic behavior of short fiber reinforced polymers coupled with anisotropic damage and moisture effects.* Acta Mechanica Sinica, 2019. **35**(3): p. 495-506.
71. He, G., et al., *A combined viscoelasticity-viscoplasticity-anisotropic damage*

model with evolving internal state variables applied to fiber reinforced polymer composites. Mechanics of Advanced Materials and Structures, 2021. **28**(17): p. 1775-1796.

72. Fazlollahi, M., M.R. Morovvati, and B. Mollaei Dariani, *Theoretical, numerical and experimental investigation of hydro-mechanical deep drawing of steel/polymer/steel sandwich sheets.* Proceedings of the Institution of Mechanical Engineers, Part B: Journal of Engineering Manufacture, 2019. **233**(5): p. 1529-1546.
73. Farahani, S., V.A. Yerra, and S. Pilla, *Analysis of a hybrid process for manufacturing sheet metal-polymer structures using a conceptual tool design and an analytical-numerical modelling.* Journal of Materials Processing Technology, 2020. **279**: p. 116533.
74. Mousa, S. and G.-Y. Kim, *A direct adhesion of metal-polymer-metal sandwich composites by warm roll bonding.* Journal of Materials Processing Technology, 2017. **239**: p. 133-139.
75. Qadeer, A., et al., *Springback behavior of a metal/polymer laminate in incremental sheet forming: stress/strain relaxation perspective.* Journal of Materials Research and Technology, 2023.
76. Harhash, M. and H. Palkowski, *Incremental sheet forming of steel/polymer/steel sandwich composites.* journal of materials research and technology, 2021. **13**: p. 417-430.
77. ASTM, S., *Standard test method for determining forming limit curves.* ASTM International, West Conshohocken, PA, 2008. **1**(1): p. 1.
78. Harhash, M., et al., *Experimental characterization, analytical and numerical investigations of metal/polymer/metal sandwich composites–Part 2: Free bending.* Composite Structures, 2020. **232**: p. 111421.
79. Weiss, M., et al., *The influence of temperature on the forming behavior of metal/polymer laminates in sheet metal forming.* Journal of Engineering Materials and Technology-Transactions of the Asme, 2007. **129**(4): p. 530-

537.

80. Kazemi, F., R. Hashemi, and S.A. Niknam, *Formability and fractography of AA5754/polyethylene/AA5754 sandwich composites.* Mechanics Based Design of Structures and Machines, 2020. **50**(4): p. 1253-1267.

81. Son, Y.K., D.C. Ko, and B.M. Kim, *Prediction of delamination and tearing during stamping of polymer-coated metal sheet.* Journal of Materials Processing Technology, 2015. **220**: p. 146-156.

82. ISO, *Metallic materials–sheet and strip–determination of forming-limit curves–part 2: determination of forming-limit curves in the laboratory*, in *ISO*. 2008. p. 1-27.

83. Aghaie-Khafri, M. and R. Mahmudi, *Predicting of plastic instability and forming limit diagrams.* International Journal of Mechanical Sciences, 2004. **46**(9): p. 1289-1306.

84. ASTM, E., *Standard test methods for tension testing of metallic materials*, in *Annual book of ASTM standards. ASTM*. 2001.

85. ASTM, *ASTM D638.* Encyclopedic dictionary of polymers. New York: Springer, 2011: p. 51-51.

86. ASTM. *Strength Properties of Adhesively Bonded Plastic Lap-Shear Sandwich Joints in Shear by Tension Loading, Annual Book of ASTM Standards*. 1997. American Society for Testing Materials Philadelphia.

87. Hooputra, H., et al., *A comprehensive failure model for crashworthiness simulation of aluminium extrusions.* International Journal of Crashworthiness, 2004. **9**(5): p. 449-463.

88. Andrade, F.X.C., J.M.A.C. de Sa, and F.M.A. Pires, *Assessment and comparison of non-local integral models for ductile damage.* International Journal of Damage Mechanics, 2014. **23**(2): p. 261-296.

89. Jang, J., et al., *Prediction of delamination of steel-polymer composites using cohesive zone model and peeling tests.* Composite Structures, 2017. **160**: p. 118-127.

90. Naik, R., S. Panda, and V. Racherla, *Failure analysis of metal-polymer-metal sandwich panels with wire mesh interlayers: Finite element modeling and experimental validation.* Composite Structures, 2022. **280**: p. 114813.

91. Alfano, G., *On the influence of the shape of the interface law on the application of cohesive-zone models.* Composites Science and Technology, 2006. **66**(6): p. 723-730.

92. Han, S., et al., *The effects of adhesion on the tensile strength of steel-polymer sandwich composites.* Advanced Composite Materials, 2020. **30**(5): p. 443-461.

93. Gronostajski, J.Z. and Z. Zimniak, *Theoretical Simulation of Sheet Behavior in Forming Processes.* Journal of Materials Processing Technology, 1992. **31**(1-2): p. 57-63.

94. Panich, S., et al., *Experimental and theoretical formability analysis using strain and stress based forming limit diagram for advanced high strength steels.* Materials & Design, 2013. **51**: p. 756-766.

95. Kami, A., et al., *Numerical determination of the forming limit curves of anisotropic sheet metals using GTN damage model.* Journal of Materials Processing Technology, 2015. **216**: p. 472-483.

96. Gutkin, R., et al., *On acoustic emission for failure investigation in CFRP: Pattern recognition and peak frequency analyses.* Mechanical Systems and Signal Processing, 2011. **25**(4): p. 1393-1407.

97. Monti, A., et al., *Mechanical behaviour and damage mechanisms analysis of a flax-fibre reinforced composite by acoustic emission.* Composites Part a-Applied Science and Manufacturing, 2016. **90**: p. 100-110.

98. Mohammadi, R., et al., *Correlation of acoustic emission with finite element predicted damages in open-hole tensile laminated composites.* Composites Part B-Engineering, 2017. **108**: p. 427-435.

99. Liu, J.G., W. Liu, and W. Xue, *Forming limit diagram prediction of AA5052/polyethylene/AA5052 sandwich sheets.* Materials & Design, 2013.

46: p. 112-120.

100. Parsa, M.H., M. Ettehad, and P.H. Matin, *Forming Limit Diagram Determination of Al 3105 Sheets and Al 3105/Polypropylene/Al 3105 Sandwich Sheets Using Numerical Calculations and Experimental Investigations.* Journal of Engineering Materials and Technology-Transactions of the Asme, 2013. **135**(3).

101. Kim, K.J., et al., *Formability of AA5182/polypropylene/AA5182 sandwich sheets.* Journal of Materials Processing Technology, 2003. **139**(1-3): p. 1-7.

102. Andriyana, A., N. Billon, and L. Silva, *Mechanical response of a short fiber-reinforced thermoplastic: Experimental investigation and continuum mechanical modeling.* European Journal of Mechanics-A/Solids, 2010. **29**(6): p. 1065-1077.

103. Launay, A., et al., *Multiaxial fatigue models for short glass fibre reinforced polyamide. Part II: Fatigue life estimation.* International Journal of Fatigue, 2013. **47**: p. 390-406.

104. Amjadi, M. and A. Fatemi, *Multiaxial fatigue behavior of thermoplastics including mean stress and notch effects: Experiments and modeling.* International Journal of Fatigue, 2020. **136**: p. 105571.

105. De Monte, M., E. Moosbrugger, and M. Quaresimin, *Influence of temperature and thickness on the off-axis behaviour of short glass fibre reinforced polyamide 6.6–Quasi-static loading.* Composites Part A: Applied Science and Manufacturing, 2010. **41**(7): p. 859-871.

106. Kanters, M.J., L.F. Douven, and P. Savoyat, *Fatigue life prediction of injection moulded short glass fiber reinforced plastics.* Procedia Structural Integrity, 2019. **19**: p. 698-710.

107. Köbler, J., et al., *A computational multi-scale model for the stiffness degradation of short-fiber reinforced plastics subjected to fatigue loading.* Computer Methods in Applied Mechanics and Engineering, 2021. **373**: p. 113522.

108. Brighenti, R., A. Carpinteri, and D. Scorza, *Micromechanical model for preferentially-oriented short-fibre-reinforced materials under cyclic loading.* Engineering Fracture Mechanics, 2016. **167**: p. 138-150.
109. Jain, A., et al., *Effective anisotropic stiffness of inclusions with debonded interface for Eshelby-based models.* Composite Structures, 2015. **131**: p. 692-706.
110. Miled, B., et al., *Micromechanical modeling of coupled viscoelastic–viscoplastic composites based on an incrementally affine formulation.* International Journal of solids and structures, 2013. **50**(10): p. 1755-1769.
111. Jung, J., et al., *Improved incrementally affine homogenization method for viscoelastic-viscoplastic composites based on an adaptive scheme.* Composite Structures, 2022. **297**: p. 115982.
112. Haddad, M., I. Doghri, and O. Pierard, *Viscoelastic-viscoplastic polymer composites: Development and evaluation of two very dissimilar mean-field homogenization models.* International Journal of Solids and Structures, 2022. **236**: p. 111354.
113. Krairi, A., I. Doghri, and G. Robert, *Multiscale high cycle fatigue models for neat and short fiber reinforced thermoplastic polymers.* International Journal of Fatigue, 2016. **92**: p. 179-192.
114. Doghri, I. and L. Tinel, *Micromechanical modeling and computation of elasto-plastic materials reinforced with distributed-orientation fibers.* International Journal of Plasticity, 2005. **21**(10): p. 1919-1940.
115. Alfano, G., F. De Angelis, and L. Rosati, *General solution procedures in elasto/viscoplasticity.* Computer methods in applied mechanics and engineering, 2001. **190**(39): p. 5123-5147.
116. Bornert, M., *Homogénéisation des milieux aléatoires: bornes et estimations*. 2001, Hermes science.
117. Mura, T., *Micromechanics of defects in solids*. 2013: Springer Science & Business Media.

118. Doghri, I., L. Adam, and N. Bilger, *Mean-field homogenization of elasto-viscoplastic composites based on a general incrementally affine linearization method.* International Journal of Plasticity, 2010. **26**(2): p. 219-238.

119. Tsai, S.W. and E.M. Wu, *A general theory of strength for anisotropic materials.* Journal of composite materials, 1971. **5**(1): p. 58-80.

120. Kawai, M., et al., *Off-axis fatigue behavior of unidirectional carbon fiber-reinforced composites at room and high temperatures.* Journal of Composite Materials, 2001. **35**(7): p. 545-576.

121. 장진혁, *Predictive method of fatigue properties of fiber reinforced plastics considering damage*. 2021, 서울대학교 대학원.

122. Chaboche, J. and P. Lesne, *A non-linear continuous fatigue damage model.* Fatigue & fracture of engineering materials & structures, 1988. **11**(1): p. 1-17.

123. Lemaitre, J. and J.-L. Chaboche, *Mechanics of solid materials*. 1994: Cambridge university press.

124. Fawaz, Z. and F. Ellyin, *A new methodology for the prediction of fatigue failure in multidirectional fiber-reinforced laminates.* Composites science and technology, 1995. **53**(1): p. 47-55.

125. Kachanov, L., *Introduction to continuum damage mechanics*. Vol. 10. 1986: Springer Science & Business Media.

126. Tseng, H.-C., R.-Y. Chang, and C.-H. Hsu, *Numerical prediction of fiber orientation and mechanical performance for short/long glass and carbon fiber-reinforced composites.* Composites Science and Technology, 2017. **144**: p. 51-56.

127. Tseng, H.-C., R.-Y. Chang, and C.-H. Hsu, *Numerical predictions of fiber orientation and mechanical properties for injection-molded long-glass-fiber thermoplastic composites.* Composites Science and Technology, 2017. **150**:

p. 181-186.

128. Tseng, H.C., R.Y. Chang, and C.H. Hsu, *Numerical predictions of fiber orientation and mechanical properties for injection-molded long-carbon-fiber thermoplastic composites.* Polymer Composites, 2018. **39**(10): p. 3726-3739.

129. Tseng, H.C., et al., *Accurate predictions of fiber orientation and mechanical properties in long-fiber-reinforced composite with experimental validation.* Polymer Composites, 2018. **39**(10): p. 3434-3445.

130. Tseng, H.-C., R.-Y. Chang, and C.-H. Hsu, *The use of shear-rate-dependent parameters to improve fiber orientation predictions for injection molded fiber composites.* Composites Part A: Applied Science and Manufacturing, 2018. **104**: p. 81-88.

131. Hessman, P.A., et al., *On mean field homogenization schemes for short fiber reinforced composites: Unified formulation, application and benchmark.* International Journal of Solids and Structures, 2021. **230**: p. 111141.

132. Jiang, Q.s., et al., *Three-dimensional numerical simulation on fiber orientation of short-glass-fiber-reinforced polypropylene composite thin-wall injection-molded parts simultaneously accounting for wall slip effect and pressure dependence of viscosity.* Journal of Applied Polymer Science, 2022. **139**(45): p. e53129.

133. ISO, E., *527-2. Plastics—Determination of Tensile Properties—Part 2: Test Conditions for Moulding and Extrusion Plastics.* Organization of Standardization: Geneva, Switzerland, 2012.

134. Advani, S.G. and C.L. Tucker III, *The use of tensors to describe and predict fiber orientation in short fiber composites.* Journal of rheology, 1987. **31**(8): p. 751-784.

135. Sabiston, T., et al., *Evaluating the number of fibre orientations required in homogenization schemes to predict the elastic response of long fibre sheet moulding compound composites from X-ray computed tomography*

measured fibre orientation distributions. Composites Part A: Applied Science and Manufacturing, 2018. **114**: p. 278-294.

136. Sabiston, T., P. Lee-Sullivan, and K. Inal, *Artificial intelligence approach for increasing the fidelity of the second order fibre orientation tensor for use in finite element analysis.* Composite Structures, 2021. **275**: p. 114393.

137. Eftekhari, M. and A. Fatemi, *Creep-fatigue interaction and thermo-mechanical fatigue behaviors of thermoplastics and their composites.* International Journal of Fatigue, 2016. **91**: p. 136-148.

138. Belmonte, E., et al., *Damage initiation and evolution in short fiber reinforced polyamide under fatigue loading: Influence of fiber volume fraction.* Composites Part B: Engineering, 2017. **113**: p. 331-341.

139. Lemaitre, J. and J. Chaboche, *A non-linear model of creep-fatigue damage cumulation and interaction(for hot metallic structures).* Mechanics of visco-elastic media and bodies, 1975: p. 1975.

140. Eftekhari, M. and A. Fatemi, *On the strengthening effect of increasing cycling frequency on fatigue behavior of some polymers and their composites: Experiments and modeling.* International Journal of Fatigue, 2016. **87**: p. 153-166.

Korean abstract

스틸-고분자 샌드위치 복합재료 및 단섬유 보강 플라스틱(SFRP)을 포함한 복합재료는 높은 기계적 물성과 가벼운 무게를 가지기 때문에 자동차, 항공, 우주 및 방위 산업 등 다양한 산업 분야에서 널리 사용된다. 그러나 자동차 및 구조 부품에 사용되는 복합재료는 다양한 하중 조건을 받게 되고 이는 파괴로 이어진다. 특히 성형, 크립 및 피로와 같은 상황에서 외부 하중으로 발생하는 손상은 복합재료의 최종 파괴가 일어나기 전, 기계적 물성의 저하에 기여하기 때문에 이러한 요소들을 고려하여 안전한 설계를 하는 것이 중요하다. 본 연구에서는 이러한 손상을 감지하고 분석하기 위하여 실험 및 이론적 연구를 수행하였고, 이를 복합재의 성형성 및 크립-피로 수명 예측에 활용하였다.

우선, 스틸-고분자 샌드위치 복합재료의 성형성을 음향방출시스템을 활용한 손상 관측을 이용하여 평가하였다. 스틸-고분자 샌드위치 복합재료의 성형성은 시편의 파괴 이외에도 눈으로 볼 수 없는 곳에서 일어나는 계면 분리도 함께 고려하여 판단해야 한다. 기존의 연구들은 성형성 평가 후 계면 분리 여부만을 판단하였다. 따라서 이 논문에서는 기초 실험들을 통해 각 파괴 모드에 따른 손상 특징을 분석한 후, 성형성 평가 실험 도중 발생하는 계면 분리 손상 신호를 음향방출시스템을 통해 관측하였다. 이를 통해, 샌드위치 복합재료의 성형 방법들을 평가할 수 있는 성형한계도 도출 과정을 확립하였다.

더불어, SFRP 의 피로 수명을 예측하기 위한 점진적 유사결정립 손상 누적(PPDA) 모델을 개발하였다. SFRP 는 섬유배향의 분포를 고려하여

물성을 예측하여야 한다. 기존의 연구들은 대표 체적 요소를 유사결정립으로 분해하는 2 단계 균질화 모델을 활용하였다. 이 논문에서는 2 단계 균질화 모델을 피로 수명 예측에 활용하였다. 각 유사결정립은 응력 비와 다축 응력 상태를 모두 고려한 "normalized fatigue factor" 컨셉을 통해 마스터 S-N 곡선을 구축하여 예측하였다. 그리고 유사결정립의 파괴 및 피로 손상으로 발생하는 응력 집중을 고려하는 PPDA 모델을 개발하였다. PPDA 모델은 ABAQUS UMAT 에 구현되었고 이를 통해 시뮬레이션 한 결과, 실험 데이터와 잘 일치하였다.
마지막으로 앞서 개발한 PPDA 모델을 확장하여 SFRP 의 크립 및 크립-피로 상호 작용 효과를 예측하였다. 크립 손상 모델과 크립-피로 상호 작용 손상 모델을 "normalized fatigue factor"와 결합하여 PPDA 크립-피로 모델을 구성하였다. 예측된 크립 수명은 PPDA 모델이 다른 모델들과 비교하여 문헌의 실험 결과와 잘 일치함을 보여주었다. 또한 SFRP 의 크립-피로 상호 작용 효과의 비선형성을 문헌 결과와 비교하여 PPDA 모델의 확장 적용 가능성을 확인하였다.

주제어: 스틸-고분자 복합재료, 단섬유강화 플라스틱, 음향 방출, 평균 균질화 기법, 점진적 손상 누적 모델

학번: 2017-22541